Induced Pluripotent Stem Cells Technology For Investigating Familial Dilated Cardiomyopathy Due To Lamin A/C Mutations

Thesis

Silvia Crasto

Personal Identifier: E3141816

Master degree in Molecular Biology

INDUCED PLURIPOTENT STEM CELLS TECHNOLOGY FOR INVESTIGATING FAMILIAL DILATED CARDIOMYOPATHY DUE TO LAMIN A/C MUTATIONS

A thesis submitted for the degree of

DOCTOR OF PHILOSOPHY

The Open University

School of Life, Health and Chemical Sciences

Affiliated Research Center:

IRCCS Istituto Clinico Humanitas

Date of submission: 29 January 2019

LIST OF CONTENTS

1.ABSTRACT

Mutations of *LMNA* gene, encoding the proteins Lamin A and C, are common causes of familial dilated cardiomyopathy (DCM), typically manifesting in association with cardiac conduction defects. LaminA/C regulate various nuclear functions, including gene transcription and chromatin organization. Most of human studies on LaminA/C so far were conducted on fibroblasts, while those focusing on cardiomyocytes (CMs) are scarce. Thus, we generated a human cardiac model of *LMNA*-dependent cardiomyopathy (*LMNA*-CMP) by differentiating CMs from induced pluripotent stem cells (iPSCs) carrying the K219T and R190W *LMNA* mutations (*LMNA*-CMs). *In vitro*, these cells recapitulate morphological features of DCM. RNA-sequencing experiments revealed profound differences between control and *LMNA*-CMs transcriptomes. Remarkably, the main cardiac sodium channel gene (*SCN5A*), was one of the most downregulated gene. Accordingly, electrophysiological studies in *LMNA*-CMs showed a significant reduction of the maximal upstroke velocity and the related properties of the action potential, accompanied by a reduction of the peak sodium currents and diminished conduction velocity. Functional experiments also revealed diminished contractile force in *LMNA* mutated cells. Biochemical studies confirmed the reduction of *SCN5A* gene, and its encoded protein $Na_v1.5$, and showed an increased binding of LaminA/C to its promoter. A higher deposition of H3K27me3 marker, together with an increased binding of its catalysing complex PRC2, was also found at that genomic locus. Furthermore, 3D-FISH studies indicated a preferential localization of *SCN5A* gene at the nuclear periphery. Similar findings were obtained in relation to genes of the contractile pathways. Altogether, these data support a mechanism by which LaminA/C influence cardiac function by directly acting on transcriptional regulation of genes that control CMs functionality. Studies conducted on CMs from CRISPR/Cas9 gene-edited iPSCs proved the causality between the *LMNA* mutation and the observed phenotypes.

Finally, experiments for evaluating the efficacy of Remodelin molecule also demonstrated that the generated models are suitable for drug testing.

2. DECLARATION

The work described in this dissertation was performed at the IRCSS Istituto Clinico Humanitas (ICH), between February 2015 and January 2019. I declare that this dissertation has not been submitted in part or in whole to any other academic institution. The work reported here was entirely carried out by the author, unless otherwise indicated. Part of the results included in this dissertation have been submitted to the peer-reviewed journal Nature Communications and the related manuscript is currently under revision.

3. PREFACE

Publications obtained during the course of this thesis:

Vittoria Di Mauro, **Silvia Crasto**, Federico Colombo, Elisa Di Pasquale & Daniele Catalucci. Wnt signalling mediates miR-133a nuclear re-localization for the transcriptional control of Dnmt3b in cardiac cells. Scientific Reports. doi.org/10.1038/s41598-019-45818-4

Nicolò Salvarani*****, **Silvia Crasto*,** Michele Miragoli, Alessandro Bertero, Marianna Paulis, Paolo Kunderfranco, Simone Serio, Alberto Forni, Carla Lucarelli, Matteo Dal Ferro, Veronica Larcher, Gianfranco Sinagra, Paolo Vezzoni, Charles E. Murry, Giuseppe Faggian, Gianluigi Condorelli & Elisa Di Pasquale**.*equal contribution**. The K219T-Lamin mutation induces conduction defects through epigenetic inhibition of SCN5A in human cardiac laminopathy. Nature Communications. doi.org/10.1038/s41467-019-09929-w

Francesco Lodola, Vito Vurro, **Silvia Crasto**, Elisa Di Pasquale, and Guglielmo Lanzani. Optical Pacing of Human-Induced Pluripotent Stem Cell-Derived Cardiomyocytes Mediated by a Conjugated Polymer Interface. Advanced Healthcare Materials. DOI: 10.1002/adhm.201900198

Silvia Crasto and Elisa Di Pasquale. Induced Pluripotent Stem Cells to Study Mechanisms of Laminopathies: Focus on Epigenetics. Frontiers in Cell and Developmental Biology. doi: 10.3389/fcell.2018.00172. Review

Maria Chatzifrangkeskou, David Yadin, Thibaut Marais, Solenne Chardonnet, Mathilde Cohen-Tannoudji, Nathalie Mougenot, Alain Schmitt, **Silvia Crasto**, Elisa Di Pasquale, Coline Macquart, Yannick Tanguy, Imen Jebeniani, Michel Pucéat, Blanca Morales Rodriguez, Wolfgang H Goldmann, Matteo Dal Ferro, Maria-Grazia Biferi, Petra Knaus, Gisèle Bonne, Howard J Worman, Antoine Muchir. Cofilin-1 phosphorylation catalyzed by ERK1/2 alters cardiac actin dynamics in dilated cardiomyopathy caused by lamin A/C gene mutation. Human Molecular Genetics, ddy215, https://doi.org/10.1093/hmg/ddy215

Silvia Crasto, Nicolò Salvarani, Michele Miragoli, Marianna Paulis, Paolo Kunderfranco, Pierluigi Carullo, Alberto Forni, Giuseppe Faggian, Gialuigi Condorelli, Elisa Di Pasquale.

Lamin A/C Mutations Epigenetically Dysregulate *SCN5A* Gene Expression, Perturbing Action Potential Properties in IPSC-derived Cardiomyocytes. Abstract published by Circulation Research vol 121 suppl A11, Basic Cardiovascular sciences (BCVS) Conference, Portland (Oregon) 10-13 July 2017. Abstract

4. LIST OF FIGURES AND TABLES

5. ABBREVIATIONS

ACTC1	α-cardiac actin gene
AP	Alkaline phosphatase
AP	Action potential
APA	AP amplitude
BAF1	Barrier-to-autointegration factor 1
Ca^{2+}	Calcium
Ca_v	Calcium channel
CDM1/ 2	Cardiac differentiation medium 1/ 2
ChIP	Chromatin Immunoprecipitation
ChIP-seq	ChIP-sequencing
CIM	CVPCs induction medium
cLADs	Constitutive LADs
Cm	Membrane capacitance
CMP	Cardiomyopathy
CMs	Cardiomyocytes
CNTR	Control
CSDs	Conduction system diseases
CV	Conduction velocity
CVPCs	Cardiovascular progenitors
CX40	Connexin 40 gene
CX43	Connexin 43 gene
DamID	DNA Adenine Methylation-based Identification
DCM	Dilated Cardiomyopathy
DEFA3	Defensin alpha 3 gene
DEFA4	Defensin alpha 4 gene

DES	Desmin gene
dV/dt_{max}	Maximal upstroke velocity
EBs	Embryoid bodies
EDMD	Emery-Dreifuss muscular dystrophy
EGFP	Enhanced green fluorescent protein
EMD	Emerin gene
END-2	Endoderm-like stromal cell
ERK1/2	Extracellular signal-regulated kinase ½
ES	Embryonic stem
ESC	Embryonic stem cell
eSpCas9	Enhanced specificity SpCas9
EZH2	Enhancer of zeste homolog 2
FACS	Fluorescence-activated cell sorting
FBs	Fibroblasts
FDA	Food and Drug administration
FIAU	Fialuridine
FISH	Fluorescence In Situ Hybridization
fLADs	Facultative LADs
FPLD	Familial Partial Lipodystrophy
Fura-2 AM	Fura-2 acetoxymethyl
G9a	Euchromatic histone-lysine N-methyltransferase 2 (EHMT2), also known as G9a
HGPS	Hutchington-Gilford Progeria Syndrome
H3K4me1	Histone 3 lysine 4 monomethylation
H3K4me2	Histone 3 lysine 4 dimethylation
H3K4me3	Histone 3 lysine 4 trimethylation
H3K9me2	Histone 3 lysine 9 dimethylation

H3K9me3	Histone 3 lysine 9 trimethylation
H3K27me3	Histone 3 lysine 27 trimethylation
H3K79me2	Histone 3 lysine 79 dimethylation
IFs	Intermediate Filaments
INM	Inner nuclear membrane
IP	Immunoprecipitation
iPSC	Induced Pluripotent Stem Cells
I_{KR}	Rapid potassium current
I_{KS}	Slow potassium current
I_{Na}	Sodium current
IPA	Ingenuity Pathway Analysis
I_{to}	Transient outward potassium current
K^+	Potassium
LA	Left atrium
LAD	Lamina-associated domains
LAP2α	Lamin associated polypeptide 2α
LBR	Lamin B receptor
LC-MS	Liquid chromatography-mass spectrometry
LDHCP	Lipoatrophy with Diabetes, hepatic steatosis, hypertrophic cardiomyopathy and leukomalenodermic papules
LEM	LAP, Emerin, MAN
LGMD1B	Muscular dystrophy, limb-girdle, type 1B
LMNA	Lamin A/C gene
LMNA-CMP	Lamin A/C dependent cardiomyopathy
LMNB1	Lamin B1 gene
LMNB2	Lamin B2 gene
LQTS3	Long QT syndrome type 3

LV	Left Ventricle
MAD	Mandibular Dysplasia
MAN	Matrin-3
MPD	Maximal diastolic potential
MYBPC3	Myosin-binding protein-C gene
MYH6	α-Myosin heavy chain 6 gene
MYH7	α-Myosin heavy chain 7 gene
Na^+	Sodium
NAT10	N-acetyltransferase 10 enzyme
Na_v	Sodium channel
$Na_v1.5$	Voltage-dependent sodium channels 1.5
NE	Nuclear envelope
NL	Nuclear Lamina
NLS	Nuclear localization signal
NPCs	Nuclear pore complexes
NT	Nuclear transplantation
ONM	Outer nuclear membrane
PAT-ChIP	Pathology tissue chromatin immunoprecipitation
pbLMNA	PiggyBac-LMNA
PBMNCs	Peripheral blood mononuclear cells
PCNA	Proliferating Cell Nuclear Antigen
PcG	Polycomb group
PRC1	Polycomb repressive complex 1
PRC2	Polycomb repressive complex 2
PURO	Puromycin
RA	Right Atrium
Rb	Retinoblastoma

ROCKi	Rho-associated coiled coil kinase inhibitor (Y27632)
RPKM	Reads Per Kilobase Million
RV	Right Ventricle
SCN5A	Sodium channel 5 A gene
SCN10A	Sodium channel 10 A gene
SCN11A	Sodium channel 11 A gene
sgRNA	Single guide RNA
SMT	Single molecule tracking
SN	Sinus node
SNPs	Single- nucleotide polymorphism
STED	Stimulated emission depletion
Suv39H1/H2	Suppressor Of Variegation 3-9 Homolog 1 / Homolog 2
TBX3	T-box transcription factor 3 gene
TBX5	T-box transcription factor 5 gene
TCAP	Titin-Cap
TNNT2	Cardiac troponin 2 gene
TNNC1	Cardiac troponin C1 gene
TNNI3	Cardiac troponin I3 gene
TNPO1-NUP153	Transportin-1/NPC protein complex
TRIM28	Tripartite motif containing 28 gene
TRIM63	Tripartite Motif Containing 63 gene
TrxG	Trithorax group
TSS	Transcriptional Start Site
TTN	Titin gene
vLADs	Variable LADs

6. CHAPTER INTRODUCTION

6.1. Lamin A/C and Laminopathies

Mutations in *LMNA* gene, encoding the nuclear proteins Lamin A and C, give rise to a phenotypically heterogeneous group of disorders collectively called *Laminopathies*. These manifest with many different clinical disorders, typically presenting with tissue-specific phenotypes, often overlapping. Based on their clinical manifestations, laminopathies may be grouped into those that affect the striated (cardiac/skeletal) muscle (i.e. Emery-Dreifuss Muscular Dystrophy and Dilated Cardiomyopathy type 1A), the adipose tissue (Familial Partial Lipodystrophy – FPLD and other lypodytrophies) and the peripheral nerves, or can give rise to multi-organ systemic syndromes, mainly associated with accelerated ageing (i.e. Hutchington-Gilford Progeria Syndrome atypical Werner Syndrome). Table 1 gives a summary of both tissue-specific and systemic syndromes caused by Lamin A/C mutations; the tissue-specific phenotypes are also graphically represented in the Fig. 1.

Tissue-specific disorder	Inheritance
Cardiomyopathy, dilated, 1A	**AD**
Charcot-Marie-Tooth disease, type 2B1	**AR**
Emery-Dreifuss muscular dystrophy 2 (EDMD2)	**AD**
Emery-Dreifuss muscular dystrophy 3 (EDMD3)	**AR**
Heart-hand syndrome, Slovenian type	**AD**
Muscular dystrophy, congenital	**AD**
Muscular dystrophy, limb-girdle, type 1B (LGMD1B)	**AD**
Malouf syndrome	**AD**
Familial partial lipodystrophy of the Dunnigan, type 2 (FPLD)	**AD**

Systemic-multiorgans disorder	Inheritance
Hutchinson-Gilford Progeria syndrome (HGPS)	**AD**
Restrictive dermopathy, lethal	**AD**
Atypical Werner syndrome	**AD**
Mandibular Dysplasia (MAD)	**AR**
Lipoatrophy with Diabetes, hepatic steatosis, hypertrophic cardiomyopathy and leukomalenodermic papules (LDHCP)	**AD**

Table 1. Diseases caused by *LMNA* gene mutations, classified as tissue-specific (top) or systemic- multi-organs disorders (bottom). AD: Autosomal Dominant; AR: Autosomal Recessive. Adapted from (Crasto and Di Pasquale 2018)

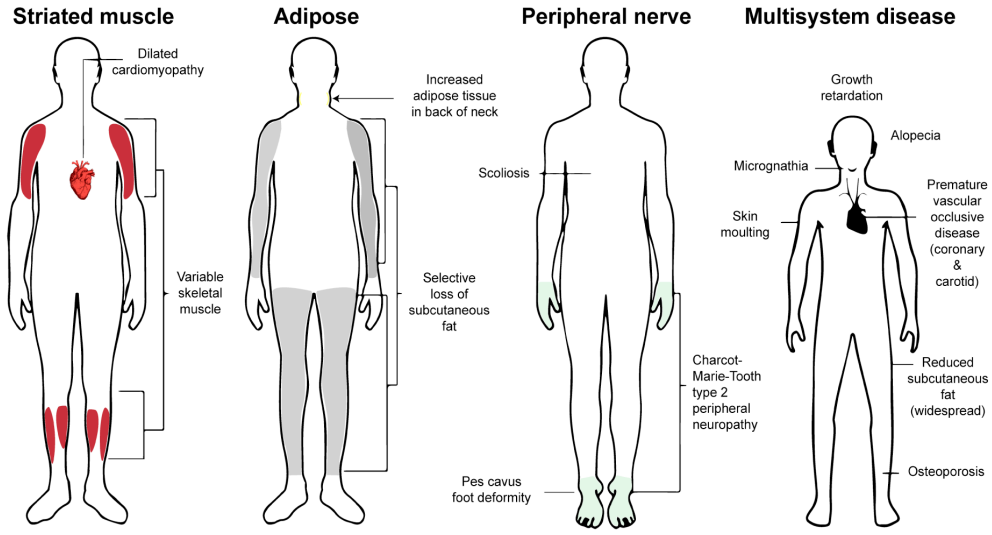

Figure 1. Schematic representation of tissue specific phenotypes due to *LMNA* mutations. (*Adapted from (Worman 2012).*

In spite of this heterogeneity, cardiac defects are quite frequent in all laminopathic patients and represent one of the primary cause of death (Worman and Bonne 2007), strongly indicating the heart as a principal tangible site of Lamin A/C action.

Mutations in Lamin A/C were first identified associated to Emery-Dreifuss Muscular Dystrophy (EDMD) in 1999 ((Bonne, Di Barletta et al. 1999); in general, EDMD is especially caused by missense mutations but also frameshifts and deletions have been found in affected subjects (Benedetti, Menditto et al. 2007).

Beside the autosomal dominant, an X-linked form of the diseases also exists and is caused by mutation in the *EMD* gene, encoding the protein of the inner nuclear membrane, emerin (Bione, Maestrini et al. 1994).

At the clinical level, EMDM patients are usually normal at birth and in the first years of life; symptoms generally start to develop in the second decade of life with contractures first and subsequently dilated cardiomyopathy (DCM) with conduction defects. However, in patients with *LMNA* heterozygous mutations, clinical manifestations may range from those typical of EDMD to no phenotypic effect (Raffaele Di Barletta, Ricci et al. 2000).

Subsequently *LMNA* gene was also described as candidate in Familial Partial Lipodystrophy (FPLD), Dunnigan variety (Speckman, Garg et al. 2000; Cao, Liang et al. 2013). This disorder is typically characterized by loss of adipose tissue from the extremities and accumulation of fat deposition in the head and in the neck. Patients also manifest insulin resistance, dyslipidaemia and diabetes.

The above-mentioned disorders are referred to tissue-restricted diseases; however, mutations in *LMNA* gene can also cause systemic multi-organs disorders, as the Hutchinson-Gilford Progeria Syndrome (HGPS) (De Sandre-Giovannoli, Bernard et al. 2003; Eriksson, Brown et al. 2003), which can be considered one of the most severe *LMNA*-dependent disease. Premature senescence is the typical sign of HGPS, which is clinically characterized by postnatal growth retardation, midface hypoplasia, micrognathia, premature atherosclerosis, absence of subcutaneous fat, alopecia, generalized osteodysplasia with osteolysis and pathologic fractures. Patients usually appear normal at birth, but in one year all the symptoms become strongly evident. Death usually occurs at around 14.6 years of age and, progressive atherosclerosis of the coronary and cerebrovascular arteries represents the principal cause (Brown 1992). At molecular level, the *LMNA* mutation associated to HGPS causes the expression of an aberrant form of prelamin A, called progerin, that accumulates into the cell nuclei, dramatically affecting nuclear architecture and cellular functions. Progerin also increases progressively during “normal” aging but it is still not clear whether this is directly due to spontaneous *LMNA* mutations, epigenetic modifications or abnormal farnesylation.

6.1.1. Lamin A/C-dependent Cardiomyopathy

Mutations in *LMNA* gene were also shown to give rise to DCM, typically complicated by conduction system diseases, in absence or with minimal skeletal muscle involvement (Fatkin, MacRae et al. 1999). As of today, 165 unique mutations have been reported, distributed all along the entire gene (Tesson, Saj et al. 2014); however, most of the mutations occur in the head and in the rod domain, but rarely in the tail domain. The majority of the pathogenic variants are missense and nonsense mutations, while fewer are small deletions or small insertions or occur at the splicing sites; such variants exert their pathogenic action through either a haploinsufficiency or dominant-negative mechanisms (Dittmer, Sahni et al. 2014; Zahr and Jaalouk 2018).

From the clinical side, DCM is phenotypically characterized by enlargement of left ventricle (LV), with a decrease in contractile force and in blood pumping (Fig. 2). When DCM is due to *LMNA* mutations, the disease has a worse prognosis with a high penetrance (often age-dependent) and young onset, and is characterized by an extremely high rate of heart transplantation due to heart failure and an increased risk of sudden cardiac death due to the occurrence of progressive conduction system diseases, such as atrioventricular block, bradyarrhythmias and tachyarrhythmias (Arbustini, Morbini et al. 2000; van Rijsingen, Arbustini et al. 2012).

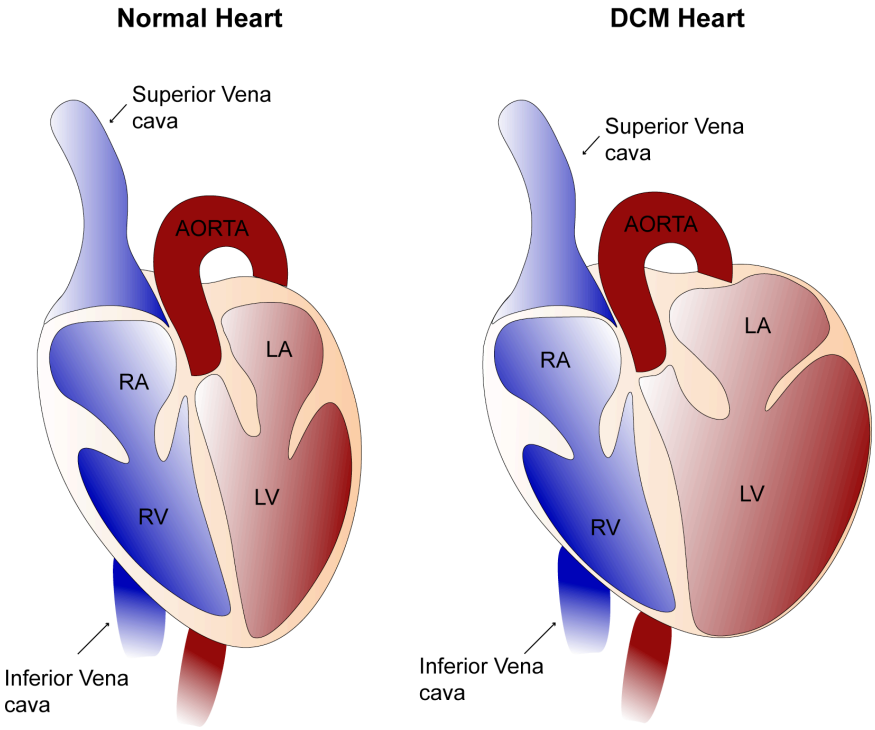

Figure 2. Representation of stylised human heart, anterior exposure. A normal Heart is illustrated on the left. The cartoon on the right schematically shows the morphological changes in patients' DCM hearts. RA: right atrium; RV: right ventricle; LA: left atrium; LV: left ventricle.

Although DCM has been reported associated to mutations in numerous genes, mostly sarcomeric, such as α-myosin heavy chain (*MYH6* and *MYH7*), α-cardiac actin (*ACTC1*), cardiac troponins (*TNNT2*, *TNNC1*, *TNNI3*), mutations in those encoding the sarcomeric protein titin (*TTN)* and the nuclear lamina component Lamin A/C (*LMNA*) are considered the most frequent causes (McNally and Mestroni 2017). As a matter of fact, *LMNA* gene is the second most commonly altered gene associated to familial DCM, and accounts for ~6-8% of the cases (Hershberger and Siegfried 2011).

Furthermore, as already specified above, cardiac abnormalities are also hallmark of other laminopathies, such as EDMD, Limb-girdle muscular dystrophy 1B (LGMD-1B) and HGPS. In this last case, even though DCM is occurring in progeria patients, the accumulation of progerin has not been specifically associated to this specific phenotype (McNally and Mestroni 2017). Therefore, progerin accumulation may not at the basis of premature aging disorders and DCM.

6.1.2. LMNA and LaminA/C: classification and biological functions

LaminA/C belong to the family of the lamin proteins, which are classified as type-V intermediate filaments (IFs) and assemble to form the nuclear lamina (NL), a dense compartment of filamentous proteins involved in maintaining the nuclear architecture and anchoring DNA and chromatin to nuclear periphery. The mammalian cell predominantly expresses four lamins' isoforms, grouped into A-type (A and C) or B-type (B1 and B2), that can be distinguished on the basis of their primary sequence (Herrmann and Aebi 2016), their chemical features (Gerace and Blobel 1980; Krohne and Benavente 1986) and their tissue-specific expression (Harborth, Elbashir et al. 2001). In fact, whereas B-type lamins are ubiquitously expressed (Dittmer and Misteli 2011), A-type ones are mostly expressed in differentiated cells and absent, or expressed in reduced quantities, in early embryos, hematopoietic cells, certain neurons, undifferentiated epithelial and mesenchymal cells and few types of cancer (Worman and Bonne 2007). The tissue-specificity and the timely-regulated expression of LaminA/C is in favour of an important role of these proteins in cell differentiation and lineage determination (Worman and Bonne 2007; Butin-Israeli, Adam et al. 2012).

LMNA gene is located on chromosome 1q21 and encodes two protein products, Lamin A and Lamin C, whereas Lamin B1 and Lamin B2 proteins are encoded by *LMNB1* and *LMNB2* genes, which are on chromosomes 5q23 and 19q13 respectively. As the other type-V IFs, lamins share protein structure domains and amino acid sequence. These are characterized by a central rod domain, composed by four α-helical segments (1A, 1B, 2A and 2B), a short N-terminal head domain and a tail-domain to the C-terminal, with nine β-strands in sandwich configuration (Fig. 3). The tail domain contains a nuclear localization signal (NLS), an Ig-fold like domain, and, with the exception of Lamin C, a carboxy-terminal CaaX domain, that is chemically modified by carboxymethylation and farnesylation, a posttranscriptional modification with an isoprenoid lipid to C-terminal region (Young, Fong et al. 2005). Whereas B-type Lamins remain farnesylated, Lamin A protein is subjected to

further processing by the zinc metalloproteinase Zmpste24/FACE1, which specifically cleaves the last C-terminal 15 residues of the farnesylated Lamin A (Prelamin A). The resultant protein is the mature Lamin A (Young, Fong et al. 2005; Rusinol and Sinensky 2006).

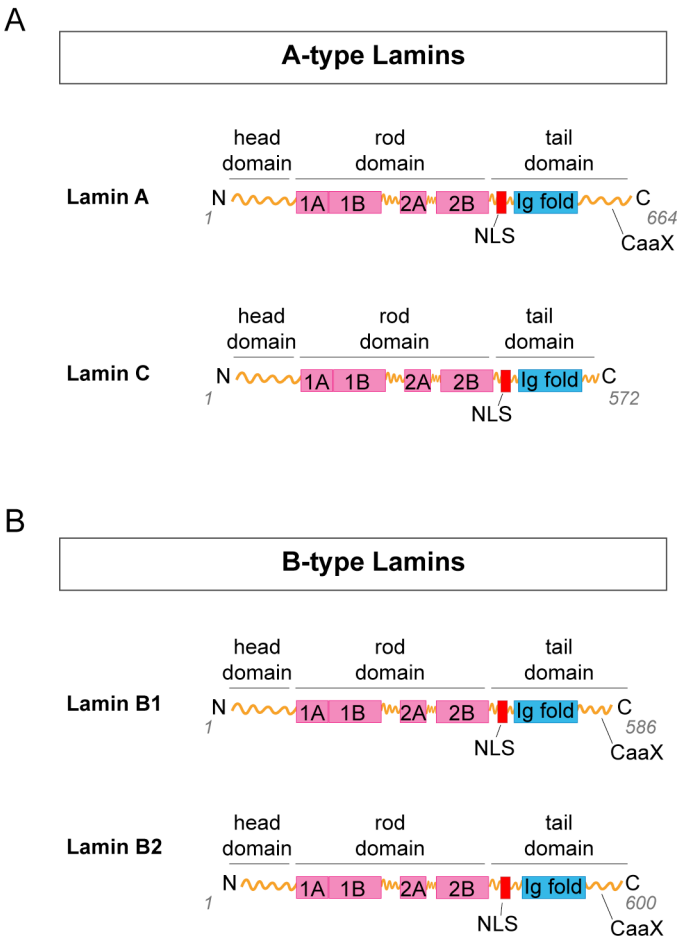

Figure 3. Schematic representation of Lamin proteins' structure. **A** panel shows A-type Lamins, distinguishing Lamin A, with 664 aminoacid residues and CaaX site included in the C-terminal tail domain, from Lamin C, with 572 residues and lacking of CaaX site. In **B,** B-type Lamins are illustrated. They are highly similar for their sequence but encoded by two different genes. Protein structure is extensively conserved among the different types of Lamins, with a N-terminal head domain, a central α-helical rod domain and a C-terminal tail domain.

Despite the preferential localization at the nuclear envelope, a small fraction of LaminA/C protein is also present at the nuclear interior. The nucleoplasmatic LaminA/C is characterized by an increased solubility and, as such, seems to be more dynamic; in this

compartment, its interaction with some chromatin binding-factors, as LAP2α, has been described, which is involved in the regulation of gene transcription and chromatin remodelling (Dechat, Korbei et al. 2000).

6.1.3. LaminA/C and its binding partners

The nuclear envelope (NE) is one of functional domain of the nucleus: it is composed by two membranes the "inner" (INM – inner nuclear membrane) and the "outer" (ONM – outer nuclear membrane), which are separated by a lumen region of 30-50 nm, or fuse together to form the nuclear pore complexes (NPCs) (Fig.4).

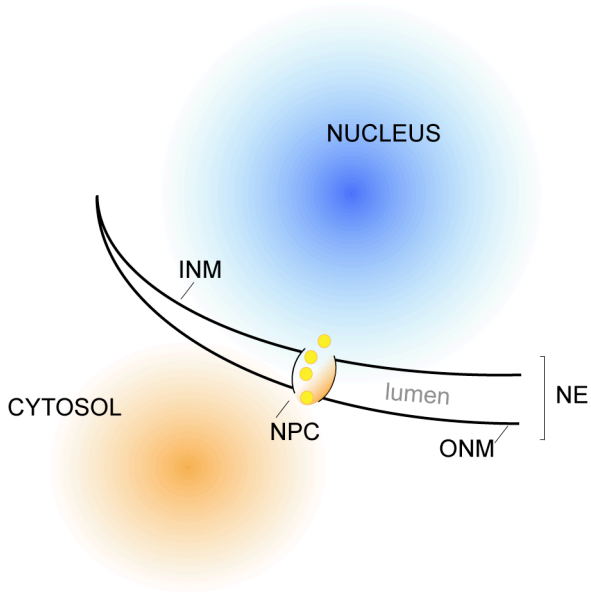

Figure 4. Structure of the nuclear envelope. The inner nuclear membrane (INM) and the outer nuclear membrane (ONM) define the NE. These two membranes are always separated by the lumen, but they fuse together in nuclear pore complex (NPC).

The INM and ONM are structurally and functionally different and establish interaction with several integral membrane proteins. Among these, A- and B-type Lamins are the most abundant and create an intricate filamentous network of interactions. Several studies reported more than 100 lamina associated polypeptides (LAP), identified through LC-MS analysis (Kubben, Voncken et al. 2010). Only 13% of the total number of interacting proteins were known to be Lamin A/C binding partners; those include: Barrier-to-autointegration

factor 1 (BAF1), emerin, matrin-3, MAN, titin, Lamin A, Lamin B, replication dependent and independent histones, lamin B receptor (LBR) and tripartite motif containing 28 (Trim28). The LAP concept, already emerged in 1988 (Senior and Gerace 1988; Foisner and Gerace 1993), was used to described a subgroup of polypeptides with specific solubility features, but then expanded to other proteins with various characteristics, which are bound to Lamins with variable strength (Wilson and Foisner 2010) as: retinoblastoma (Rb), PCNA, c-FOS and OCT-1. In addition to the binding with proteins of the INM, the interaction between LaminsA/C and lamina-associated polypeptide (LAP) 2α (Dechat, Gajewski et al. 2004) is quite relevant for LaminA/C regulatory function. LaminA/C- LAP2α complex exists as a detergent-soluble pool in the nuclear interior (Kolb, Maass et al. 2011) and the interaction between the two proteins is necessary to regulate the nucleoplasmatic localization of LaminA/C. Indeed, studies on LAP2α knock-out mice show absence of nucleoplasmic A-type lamins. Re-expression of the wild-type LAP2α into knock-out cells is sufficient to rescue the localization of LaminA/C in the nuclear interior (Naetar, Korbei et al. 2008).

Some of the binding partners listed above share a protein domain, called LEM (**L**AP, **E**merin, **M**AN) domain, which is a common motif composed by two α-helix motifs of 45 residues. BAF protein can bind the LEM domain and can be used as a "bridge" to connect DNA or chromatin to lamina-associated proteins or to Lamins directly (Margalit, Neufeld et al. 2007).

Interestingly, Polycomb Repressive Complex 1 and 2 (PRC1 and PRC2) have been recently added to the list of the lamin-binding partners (Cesarini, Mozzetta et al. 2015). In both, mouse model and *in vitro* studies using C2C12 cells, Lamin A/C was described as necessary scaffold to guarantee the proper formation of the polycomb bodies (Cesarini, Mozzetta et al. 2015; Marullo, Cesarini et al. 2016). Furthermore, changing in gene positioning and chromatin relocalization were found in a EDMD mouse model, and were demonstrated to be a consequence of the impairment of LaminA/C – PRC2 interaction. While the pivotal role of PRC2 in regulating chromatin architecture and transcription is widely recognized, clear

evidence that elucidate the molecular mechanisms at the basis of the dynamic interaction between the two proteins are still missing. However, the recent studies describing the cooperation of PRC2 and LaminA/C represent a step forward in the understanding of their interplay in regulating gene transcription.

6.1.4. The epigenetic role of Lamin A/C

Besides its well-known structural role, LaminA/C is also a master player in regulating gene transcription through mechanisms involving chromatin organization and remodelling, DNA replication and signal transduction pathways (Gruenbaum, Margalit et al. 2005; Dechat, Pfleghaar et al. 2008; Dittmer and Misteli 2011). In addition to the numerous interactions of LaminA/C with specific proteins and/or transcriptional factors, already described the *section 6.1.3* of this Thesis, LaminA/C is also able to interact directly with chromatin, in regions of the genome defined as the **L**amina-**a**ssociated **d**omains (LADs) (Pickersgill, Kalverda et al. 2006). These regions have been firstly identified and mapped in *D. melanogaster* and *C. elegans*, and then were also discovered in the mouse and human genomes (Pickersgill, Kalverda et al. 2006; Guelen, Pagie et al. 2008; Ikegami, Egelhofer et al. 2010; Peric-Hupkes, Meuleman et al. 2010), using the adenine methyltransferase technique (DamID) (Pickersgill, Kalverda et al. 2006). LADs are large genomic regions ranging from 0.1 to 10 megabases (Mb) in size and their occupancy corresponds to more than one–third of mouse and human genome (Kind and van Steensel 2010; Meuleman, Peric-Hupkes et al. 2013). The majority of genes present in the LADs are expressed at very low level and possess several molecular characteristics of heterochromatin (i.e. low genes density and expression; H3K9me2, H3K9me3 and H3K27me3 histone marks enriched regions) (Fig.5) (Meuleman, Peric-Hupkes et al. 2013).

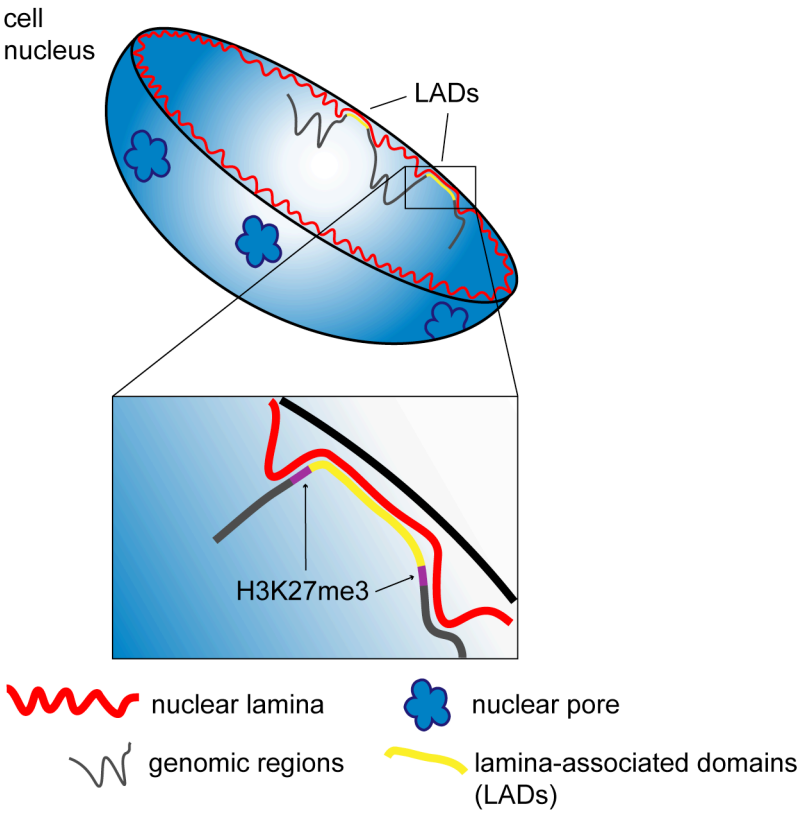

Figure 5. Schematic representation of lamin-associated domains (LADs) in a eukaryotic nucleus. LADs are the large genomic regions interacting with the nuclear lamina (here indicated as a coil red line); these are flanked by H3K27me3 histone marker (purple portion), usually identifying those referred as variable LADs..

Genome-wide studies indicated the existence of different LADs, those that are conserved among cell-type, named constitutive LADs (cLADs) and others that interact with the NL in a cell-type specific manner, called facultative (or variable) LADs (fLADs or vLADs) (Peric-Hupkes, Meuleman et al. 2010; Meuleman, Peric-Hupkes et al. 2013). cLADs are more conserved than fLADs, in terms of size and genomic position, among the species (mouse and human) and therefore form a structural ”backbone” that is crucial to determine the spatial architecture of chromosomes into the nucleus. Instead, fLADs change their genomic positions inside the nucleus: they mostly contain genes involved in development, and are subjected to remodelling during differentiation of mammalian cells, demonstrating the dynamics and flexibility of their interaction with the NL. These changes correspond to specific gene expression pattern: detachment from NL is typically associated to gene

activation, while attachment to the NL is accompanied by gene repression (Peric-Hupkes, Meuleman et al. 2010; Robson, de Las Heras et al. 2016).

However, how LADs sequences determines the LaminA/C interactions is still enigmatic, but it seems to be linked to the chromatin state. The presence of some histone marks at the LAD regions (i.e. H3K9me2/me3; H3K27me3), suggests G9A, SUV39H1/H2 and EZH2 enzymes, which catalyse these modifications, may be directly involved in orchestrating such NL-genome interaction (Bian, Khanna et al. 2013; Kind, Pagie et al. 2013; Chen, Yammine et al. 2014; Harr, Luperchio et al. 2015).

6.1.5. The role of Lamin A/C in the Heart

As already mentioned in the above sections of this thesis, cardiac involvement is very frequent in all laminopathies and manifest with cardiomyopathy associated with disturbances of the conduction, suggesting an important function of LaminA/C in the correct functioning of the heart.

Besides, studies addressing the role of LaminA/C in the heart and in the cardiomyocytes, the contracting units within the heart, are still limited.

Most of the knowledge we gained so far on functional and molecular mechanisms behind the cardiac phenotype in laminopathies comes from mouse models. In 1999, Sullivan and colleagues firstly generated a *Lmna* knockout (*Lmna*$^{-/-}$) mouse. The homozygous null mice displayed the following major phenotypes: (i) retarded growth rate, (ii) reduced stores of white fat and (iii) cardiac arrhythmia (Sullivan, Escalante-Alcalde et al. 1999). These mice generally die by the fourth week after birth. At molecular level, increased of pro-adipogenic factors (PPAP$_\gamma$ and CEBP/α) and decreased of Wnt-10/β-catenin levels have been shown as result of LaminA/C lack (Tong, Li et al. 2011), supporting the hypothesis that LaminA/C can influence myogenesis and osteogenesis through regulating adipogenesis (Tong, Li et al. 2011). Significant contributions to the understanding of the pathophysiology of cardiac

laminopathy have come from the H222P-*Lmna* transgenic mice (Arimura, Helbling-Leclerc et al. 2005). These mice showed cardiac conduction defects, dilatation of the heart chambers, increased fibrosis and lack of hypertrophy, due to elevated extracellular signal-regulated kinase 1/2 (erk1/2) (Chatzifrangkeskou, Le Dour et al. 2016). Moreover, Mounkes and colleagues generated a homozygous KI-*Lmna* N195K mouse model, which also recapitulated the DCM phenotype and exhibited disruption of the structural organization of the cardiomyocytes as misexpression and/or mislocalization of connexin 40 and connexin 43 and loss of sarcomeres organization were observed (Mounkes, Kozlov et al. 2005).

Although animal models have been necessary to significantly improve our knowledge on the genetics, the physiology and the molecular counterpart of lamin-dependent cardiomyopathy, human phenotypes may not be completely represented in mice, since numerous differences exist between the two species in the pathophysiology of the heart (discussed in detail in *paragraph 6.2.6* of this Thesis). Therefore, studying the disease using animal models may not be exhaustive. On the other hand, studying cells from human heart has limitations, mainly due to the limited accessibility of the organs and the difficulty to maintain heart cells ex vivo, so that human studies have been limited so far to more accessible cell type, such as fibroblasts, skeletal muscle cells and adipocytes.

The possibility to obtain cardiomyocytes (CMs) of human derivation *in vitro* may significantly improve our possibility to investigate disease-causing mechanisms and contribute to burst the development of new therapies.

In 2004, Gaustad and colleagues provided evidence for the involvement of LaminA/C in determining specific lineage specification events for the differentiation of contractile tissue. They showed how human adipose tissue stem cells, which do not express LaminA/C, become able to differentiate into beating CMs after exposure to cell extracts from rat CMs, which instead express LaminA/C (Gaustad, Boquest et al. 2004). Based on diverse studies conducted on different cell types, several hypotheses have been raised to explain the molecular mechanisms at the basis of LaminA/C action in the heart. On one hand, LaminA/C

has been proposed to influence the structural architecture of the contractile tissue, conferring resistance and protection against mechanical stress (Swift, Ivanovska et al. 2013); this is probably due to the α-helical coiled coil structure assembled into rope-like fibres that typically confer mechanical resistance to tension. In addition to the "mechanical stress" theory described above, the softer nuclei's structure caused by *LMNA* mutations can increase sensitivity to cell damage and apoptosis, and lead to an impairment in the nucleo-cytoskeletal coupling. This is referred as "structural hypothesis", and identifies the morphological abnormalities of the laminopathic nuclei as the molecular events at the basis of the lamin-dependent cardiac phenotypes (Nikolova, Leimena et al. 2004). Besides this "structural hypothesis", a "gene expression" hypothesis has also been raised. This is based on the putative role of LaminA/C in regulating gene transcription and proposes these proteins as important regulators of tissue-specific gene expression. As of today, there are no clear evidence supporting one hypothesis more than the other. Further studies are necessary to deepen our knowledge on the complex molecular events driving onset and progression of cardiac disease in laminopathies and to unveil how LaminA/C protein interfere with CM function.

On this regard, the advent of induced pluripotent stem cells (iPSC) has revolutionized the approached to the disease, allowing the generation of unlimited number of human CMs for any experimental need, *in vitro*. Few iPSC-based models of lamin-dependent cardiomyopathy have been reported in the last years that contributed to further improve our knowledge on the field. A detailed description of the aforementioned iPSC-models is provided in the *section 6.2.8 of this chapter*.

6.2. Induced Pluripotent Stem Cells (iPSCs)

6.2.1. Cell Reprogramming: Concepts and Developments

In 2006, Shinya Yamanaka, from Kyoto University, demonstrated for the first time the possibility to generate cells with a pluripotent potential from terminally differentiated cells, mouse adult fibroblasts, through the exogenous expression of four transcription factors (*Oct3/4; Sox2; c-Myc; Klf4*), identified over a 24 factors known to play an important role in maintenance of embryonic stem (ES) cell identity (Fig.6) (Takahashi and Yamanaka 2006). The derived pluripotent cells were called induced Pluripotent Stem Cells (iPSC) and marked the beginning of a new era for the investigation of human diseases.

In fact, in 2007, iPSCs were also derived from human fibroblasts by two different groups, using either the previously four identified "Yamanaka factors" (Takahashi, Tanabe et al. 2007) or a different cocktail of transcription factors, *OCT4*; *SOX2*; *NANOG* and *LIN28* (Yu, Vodyanik et al. 2007).

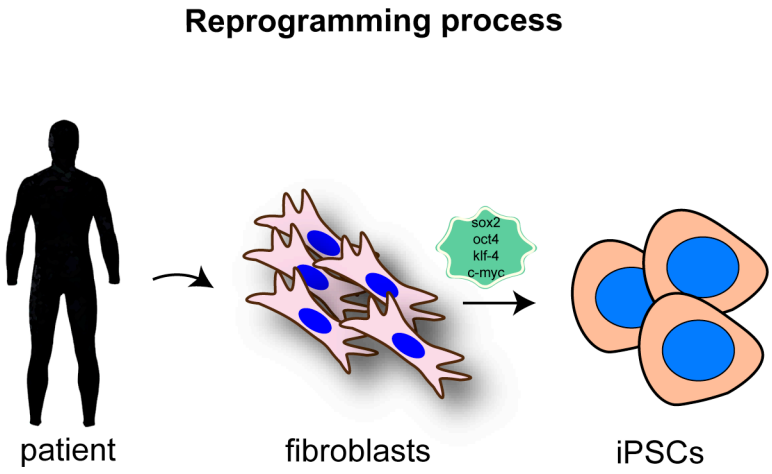

Figure 6. Schematic representation of reprogramming process. Generation of iPSCs from patient specific skin fibroblasts: transduction of the somatic cells with the "embryonic" genes *SOX2*, *OCT4*, *KLF-4* and *c-MYC* confers pluripotent potential to the transduced cells.

However, the concept that a somatic cell may acquire a pluripotent potential was not new at the time of iPSCs discovery; several important studies conducted in the previous decades demonstrated this possibility in different contexts, setting the ground that guided scientists in reaching this important milestone. The revolution of iPSCs lies in the ease of generation, which renders the technology accessible to many laboratories all over the world, and in the possibility to avoid manipulation of human embryos (and their derivates).

In 1952 the concept of cellular reprogramming was firstly demonstrated by Briggs and King. They showed the developmental potential of nuclei isolated from frog cells at different stages of embryonic development, by transplantation into enucleated oocytes (Briggs and King 1952). The method was subsequently called nuclear transplantation (NT) or "cloning". In their studies they observed a gradual decline in the cloning efficiency with the increase of differentiation of the donor-cell. A decade later, in 1962, Gurdon succeeded in generating adult frogs by nuclear transfer from embryonic cells (Gurdon 1962).

The establishment of stem cells properties, namely the ability to self-renew and to differentiate into multiple lineages, dates back to the sixties, thanks to the studies of James Till and Ernest McCulloch on the hematopoietic system: they demonstrated that the injection of bone marrow cells into the spleen of irradiated mice was sufficient give rise to multiple lineage hematopoietic colonies (McCulloch and Till 1960).

In the subsequent years, the relevant progresses in the field made possible to succeed in the cloning of mammals, from the "famous" sheep Dolly (Wilmut, Schnieke et al. 1997) to mouse and other mammals (Hochedlinger and Jaenisch 2002; Eggan, Baldwin et al. 2004), and in the derivation of embryonic stem (ES) cells of both, mouse (Evans and Kaufman 1981) and human derivation (Thomson, Itskovitz-Eldor et al. 1998). These last achievements and the studies conducted on ES cells are of particular relevance for iPSC field of research, since ES cells represent the "gold standard" for pluripotency.

On the whole, those studies have led to understand that the genetic mechanisms behind cellular differentiation are completely reversible and that terminally differentiated cells (their nuclei) are genetically pluripotent. This concept reverses the developmental model, proposed by Conrad Waddington in 1957, which describes how undifferentiated cells acquire their terminally specialization by an unidirectional process (Fig.7-A). This concept was drawn as a ball (zygote) rolling down from the top of the hill to valleys of specialized adult cells, passing through distinct differentiation states (precursors and progenitors), with different epigenetic profiles (Waddington 1957).

Cellular reprogramming can revert cells from a specific differentiated state back to an undifferentiated cell, which is defined pluripotent. The process of reprograming has been depicted as climbing the top of the hill, to highlight the complexity of the method and its low efficiency (Fig.7-B). The understanding of molecular events and epigenetic changes occurring during these processes can unveil how differentiated cells acquire their identity and a specific cell fate and provide us with more powerful tools to intervene in facilitating those processes and burst experimental potentials.

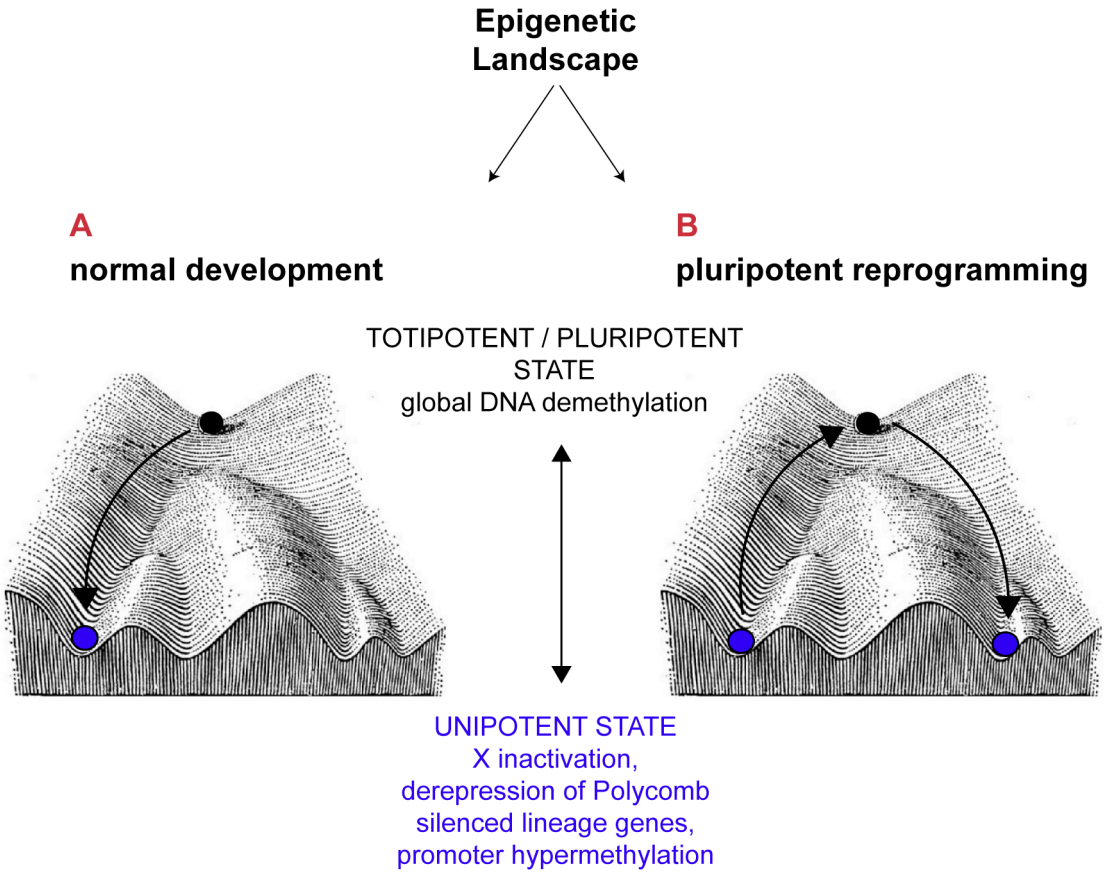

Figure 7. The Waddington model *(Adapted from Waddington "The strategy of genes" 1957)*. The cartoon in the panel **A** represents the route of normal development from a totipotent state (zygote) to terminally differentiated one, the specialized cell. **B** panel illustrates the conversion of adult somatic cells back to pluripotent state; this is a forced process that involves numerous changing of the epigenetic profile. The epigenetic status of the two different cell types is indicated in the middle.

6.2.2. The epigenetics of reprogramming and iPSCs

The reprograming process is mediated by subsequent epigenetic changes along distinct cellular states that can be summarized in: (i) the silencing of retroviral transgenes, when the pluripotency is establish, (ii) reactivation of endogenous pluripotency genes, (iii) establishment of the bivalent domains (presence of both H3K4me3 and H3K27me3) at the promoters of key developmentally-regulated genes, (iiii) DNA modifications as hypomethylation and hypermethylation of imprinted genes, (iiiii) reactivation of previously inactive X chromosome in female iPSCs (Kim, Doi et al. 2010). The multiple factors implicated in the reprogramming process are listed in the Table 2.

Chromatin Opening factors		
SWI/SNF	esBAF INO80	Increased reprogramming efficiency
Histone chaperones	ASF1	Increased reprogramming efficiency
Histone variants	TH2A TH2B H2AX H3.3 macroH2A	Increased reprogramming efficiency *except mactoH2A
CHD remodellers	CHD1	Increased reprogramming efficiency
Nurd complex	MBD3 (?)	Further investigation required
histone marks		
H3K4me1 H3K4me2 H3K4me3	WDR5	Increased reprogramming efficiency
H2AK119Ub	PRC1	Increased reprogramming efficiency
H3K27me3	PRC2	Increased and decreased reprogramming efficiency
H3K9me3	SUV3H1/2 SETDB1	Increased and decreased (Setdb1) reprogramming efficiency
H3K9me2	G9A GLP (?)	Increased reprogramming efficiency (?) Further investigation required

H3K27me3	UTX JMJD3	Increased reprogramming efficiency *except Jmjd3
H3K79me2	DOT1l	Decreased reprogramming efficiency
H3K36me3	KDM2A/B SET2	Increased reprogramming efficiency *except Set2
DNA modifications		
5-methylcytosine	PARP1 DNMT1	Increased reprogramming efficiency *except Dnmt1
5-hydroxymethylcytosine	TET1 TET2	Increased reprogramming efficiency

Table 2. Epigenetic mediators that influence the reprogramming efficiency. Chromatins modifications are reported in the first column, their catalytic enzymes in the centre of the table and functions are summarized in the right column.

At the initial stage of the reprograming, cells are globally marked with H3K4me2. WDR5, a component of Trithorax group (TRXG) mediates the methylation of H3K4me2 into H3K4me3, a chromatin marker typically linked to transcriptional activation and that, in this stage, is found associated to the promoters of pluripotency genes (Watanabe, Yamada et al. 2013), whereas Polycomb group (PcG) complex catalyses the try-methylation of K27 residue on Histone 3, to repress the expression of developmentally-regulated genes (Lee, Jenner et al. 2006). These loci simultaneously marked with H3K4me3 and H3K27me3 are defined “bivalent domains” and preferentially mark promoters of developmentally regulated genes (Harikumar and Meshorer 2015); in addition to this peculiar mark, the H3K9me2/3 demethylation, which is mediated by *JMJD1A* and *JMJD2C* and the high level of *de novo*

DNA methyltransferase activities, represent another characteristic epigenetic signature of iPSCs (Loh, Zhang et al. 2007).

6.2.3. Insight the strategy to induce iPSC

Generation of iPSCs implicates a resetting of the epigenetic profile of the somatic cells of origin, as reported (Kim, Doi et al. 2010; Papp and Plath 2013). The expression of the "reprogramming" transcription factors promotes the establishment of an "epigenome" similar to that of ES-cells, by inducing expression of endogenous "pluripotency" genes and preventing expression of those involved in cell differentiation; the resulting reprogrammed cells, iPSCs, are indistinguishable from ES-cells for morphology and possess self-renewal and developmental potential as ES-cells (Smith 2001).

Multiple approaches have been successfully employed for cell reprogramming; choice of the strategy mainly depends on the cell type and on the intended use. A major classification of the derivation methods relies on whether the integration of the transgenes into the host genome is occurring. The efficiency of the integrative approaches is typically higher (0.01% - 1%) than the non-integrative ones, but the random virus integration represents an issue since it can potentially alter the expression of genes, such as oncogenes. Thus, use of circular plasmids, non-integrative vectors or mRNA-based methods was employed to overcome this limit. The available reprogramming approaches are summarized in the Table 3.

Integrative Methods	-Retroviral vectors (Takahashi, Tanabe et al. 2007) -Lentiviral vectors (Blelloch, Venere et al. 2007; Yu, Vodyanik et al. 2007) -Excisable vectors (Kaji, Norrby et al. 2009; Woltjen, Michael et al. 2009)
Non-integrative Methods	Sendai virus-based vectors (Fusaki, Ban et al. 2009)
DNA free method	Modified mRNAs (Warren, Manos et al. 2010)

Table 3. Different methods adopted to generate iPSCs.

6.2.4. Characterization of iPSCs

Following generation, a comprehensive characterization of the iPSCs lines is required in order to assess their actual pluripotency (International Stem Cell, Adewumi et al. 2007; Marti, Mulero et al. 2013). Various criteria are adopted to verify that iPSCs possess pluripotency-associated features: these mostly relies on assessment of their similarity to ES cells and include morphology, functionality and molecular ES cell-like characteristics (Fig.8). On regard of the morphological evaluation, iPSCs, must be round colonies with defined borders and display high nucleus/cytoplasm ratio with prominent nucleoli. Also, iPSCs possess alkaline phosphatase (AP) activity.

At the molecular level, the expression of pluripotency transcription factors (*NANOG*, *SOX2*, *OCT4* and others) and surface antigens typical of ES cells, as SSEA-3/4 and TRA-1-60 is required.

At last, embryoid bodies (EBs) and teratoma formation assays represent the most stringent test in support of the full pluripotency of the generated iPSC lines, indicating they are able to differentiate into derivatives of the three germ layers.

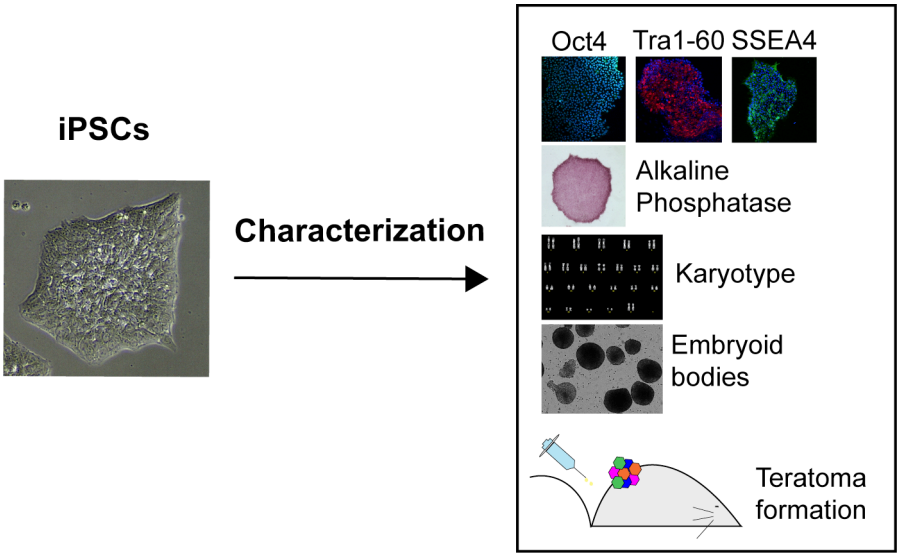

Figure 8. Workflow of iPSCs characterization. To verify the actual pluripotency of generated iPSC clones, specific assays are typically used: ES-like morphology, analysis of the expression of pluripotency markers (as TRA1-60, DNMT3B, OCT4, REX1 and SSEA4), Alkaline phosphatase activity, embryoid bodies and teratoma formation assays.

Under defined culture conditions, iPSCs can be cultured for many passages, even in feeder-free conditions, while maintaining a normal karyotype. Furthermore, culturing iPSCs in a hypoxic environment at 5% tension of O_2 has been shown to positively influence the cellular reprogramming, by increasing the efficiency of the process, and to favour their genomic stability (Yoshida, Takahashi et al. 2009).

6.2.5. Generation of cardiomyocytes from iPSC

Due to their ability to give rise to any cell typo of the body, iPSCs have been demonstrated to be able to spontaneously differentiate into contracting cardiomyocytes (CMs) (Xu, Police et al. 2002; He, Ma et al. 2003). However, the efficiency of this spontaneous differentiation process is very low, and represented for a while a limitation to their massive use. Over the past 10 years, thanks to the gained knowledge on cardiac development, several advances have been made that improved the efficiency and reproducibility of the cardiac differentiation protocols (Laflamme, Chen et al. 2007; Yang, Zhang et al. 2008).

Cardiac differentiation methods can be classified into three categories:

1) co-culture with mouse visceral endoderm-like (END-2) stromal cell;
2) Embryoid body (EB)-based differentiation;
3) Monolayer methods.

The co-culture method was firstly used to demonstrate the differentiation of CMs from ES cells, by co-culturing them with END-2 cells (Mummery, Ward-van Oostwaard et al. 2003). However this method was limited by a low CMs yield (usually from 10% to 1%) and their immature phenotype (Passier, Oostwaard et al. 2005; Fujiwara, Yan et al. 2011).

Most of the available methods for differentiating CMs from iPSCs are instead based on EB formation. EBs are 3D spherical aggregates that form from pluripotent cells when cultured into low-adhesion plates. They mimic embryonic development and can give rise to various cell types, including CMs in a range that varies from 5% to 70% (Laflamme, Chen et al. 2007), depending on the experimental settings. Yield of CMs obtained from spontaneous EB differentiation is extremely low, so that administration of chemicals factors and physical cues, acting on signalling pathways that are key in driving cardiac development, have been introduced to improve the differentiation efficiency. The "hanging-drop" (Yoon, Yoo et al. 2006) and "spin EBs" (Ng, Davis et al. 2005) are examples of EB-based methods, but still with limited efficiency; use of growth factors as Activin A, BMP4, bFGF, WNT-3A, VEGF or DKK1 has demonstrated to enhance efficiency and are included in some of the currently used protocols (Yang, Zhang et al. 2008).

More recently, methods that rely on iPSCs differentiation as a monolayer of cells, called here "monolayer methods" have prevailed on the other approaches, probably because of their ease to handle and the extremely high differentiation efficiency. These methods are based on the administration of growth factors and small molecules to iPSCs cultured in monolayer conditions; these factors drive differentiation more specifically and increase yield and purity of generated CMs. In 2007, the sequential treatments with Activin A and BMP4 was firstly applied to ES cells (H7 line) and reported to give rise to >30% contracting CMs at the 12th day of the differentiation process (Laflamme, Chen et al. 2007). This differentiation efficiency was higher than the one reported using EBs methods at that time.

In 2010, the formulation of a protocol based the modulation of the WNT/β-catenin signalling pathway, which is key in driving early cardiac development, led to a significant improve in the field, generating up to 75-90% of highly pure CMs (Paige, Osugi et al. 2010; Zhang, Klos et al. 2012; Lian, Zhang et al. 2013).

In the last few years, the studies on the field have continued to explore strategies to enhance quality and purity of the CMs differentiated from iPSC. Tohyama S. and colleagues

proposed a protocol to purify CMs over the other contaminant cells, which takes advantage of the specific metabolic properties of cardiac cells (oxidative *vs* glycolytic), demonstrating that use of lactate instead of glucose as a nutrient was sufficient to obtain 99% CMs pure population (Tohyama, Hattori et al. 2013). Furthermore, a recent study identified a specific population of cardiovascular progenitors (CVPCs), which can be obtained *in vitro* from iPSCs, cultured and expanded up to 15 passages and subsequently differentiated in CMs (Cao, Liang et al. 2013; Takeda, Kanki et al. 2018). The above described "monolayer methods" are summarized in the Figure 9.

Although functional and structural properties of iPSC-CMs improved over time, these cells are still immature if compared with adult CMs (Lieu, Fu et al. 2013). Many attempts have been made and are still under investigation to improve maturity of CMs differentiated from iPSCs. One possibility is to keep cells in culture for prolonged time (Otsuji, Minami et al. 2010) or to apply electromechanical stimulations (Nunes, Miklas et al. 2013; Mihic, Li et al. 2014). Besides the improvements obtained with these approaches, iPSC-CMs still retain characteristics which are more similar to foetal than adult CMs (Robertson, Tran et al. 2013). Thus, the future directions of the research in the field will move not only to further improve the differentiation efficiency but also to develop protocols able to generate more mature iPSC-derived CMs.

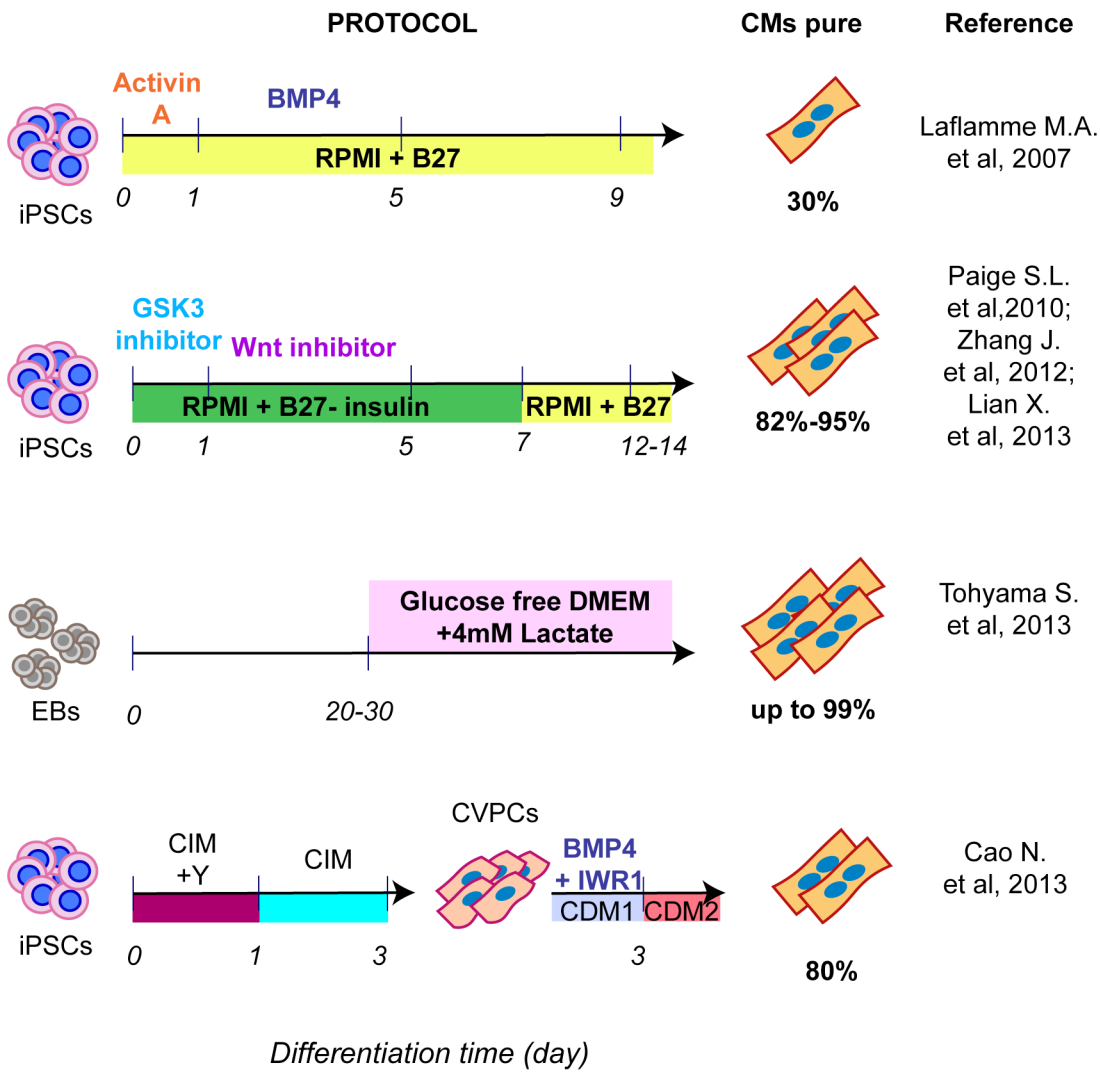

Figure 9. **Schematic representation of differentiation protocols based on "monolayer methods"**. CIM: CVPCs induction medium; Y: Y27632, Rho-associated coiled coil kinase (ROCK) inhibitor; CDM1/ 2: cardiac differentiation medium 1/ 2.

Furthermore, it is worth discussing that the differentiation protocols described above give rise to a mixed population of cardiac cells, including atrial, ventricular and pacemaker-like CMs subtypes.

Very recently, few studies described new differentiation strategies to promote the generation of the specific CMs' subtypes (Lee, Protze et al. 2017; Cyganek, Tiburcy et al. 2018); this possibility represent an important achievement in the field, since it allows modelling of cardiac diseases which preferentially affect one cell type, such as atrial fibrillation, ventricular tachycardia and cardiomyopathy, and the test of specific therapeutic option in

the proper cell type. These protocols are based on induction of specific mesodermal progenitor populations, from which atrial and ventricular CMs derive (Lee, Protze et al. 2017). Results from these studies also provide the access to cells at early stages of cardiac development that can be used as platform to study congenital cardiac diseases that are due to defects occurring during cardiac development.

6.2.6. Basics on cardiomyocytes' functioning

Mouse and human hearts exhibit different electrophysiological properties. For example, QT interval of the ECG profile is five times longer in humans than in mice; these also displayed differences in the shape and duration of the action potential (AP), with cardiac AP in mice being shorter than that in humans and lacking a clear phase 2 (or plateau) (Davis, van den Berg et al. 2011).

Unlike skeletal muscle APs, which are generated by nervous system activity, the APs in the heart are due to events provoked by specialized cardiac tissues areas: the sinus nodes (SN). Located between the superior vena cava and the right atrium (RA), nodes are able to initiate the impulse propagation that rapidly travels across the myocardium, passing from a cell to the adjacent one through gap junctions, which electrically connect myocardial cells. The AP travels throughout the whole heart, causing a propagated electrical wave (Feher 2012). The AP occurs when the cellular membrane depolarizes (inward currents) and then rapidly repolarizes (outward currents), moving back to the resting state (Carmeliet and Vereecke 2002). The inward currents are mostly generated by voltage-gated Na^+ and Ca^{2+} channels (Na_v and Ca_v respectively), while K^+ channels are responsible of the outward currents. AP profiles vary between different areas of the heart but can be essentially divided into 5 phases, summarized below and graphically represented in the Figure 10:

- **Phase 0**: the initial phase of depolarization of the membrane, which quickly brings the negatively charged membrane potential (about -80 mV) to a positive value. Na^+ rapidly gets through voltage-gated sodium channels, allowing cell depolarization.

- **Phase 1**: Na^+ channels close and repolarization of cell membrane starts. This is mediated by K^+ channels. At the end of this phase, Ca^{2+} channels slowly start opening.

- **Phase 2 (or Plateau)**: the membrane potential is firstly closed to 0 mV and then becomes more negative. Plateau is the result of the combination between Ca^{2+} influx and K^+ efflux due to a decrease in K^+ cell permeability and an increase in Ca^{2+} permeability.

- **Phase 3**: the complete closure of Ca^{2+} channels and the increased K^+ permeability mark the end of Plateau phase. K^+ influx rapidly restores membrane potential.

- **Phase 4 (or Resting membrane potential)**: the stable resting potential of myocardial cells is re-established and is about -80 mV.

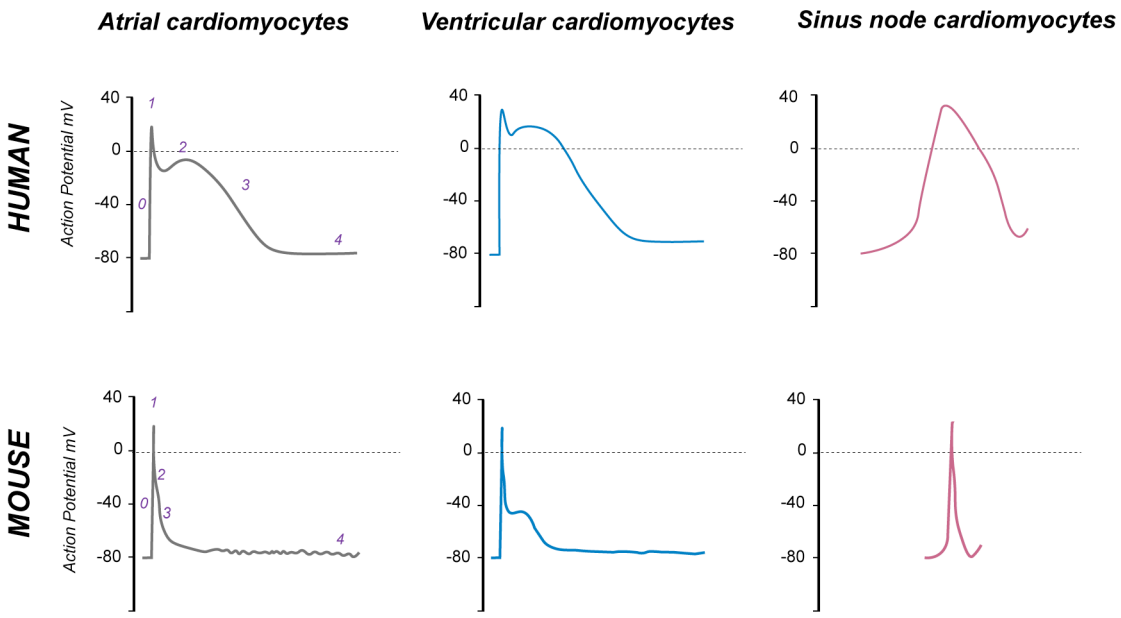

Figure 10. Atrial (grey line), ventricular (blue line) and sinus node (pink) AP profiles, recorded in human and mouse CMs. The different five phases of AP are numbered from 0 to 4, in purple.

Although the upstroke due to sodium influx (Na^+) is quite similar in mice and humans, several differences exist between the two species on regard of the K^+ currents. In fact,

transient outward potassium current (I_{to}) is the major outward current in mouse, while slow (I_{KS}) and rapid (I_{KR}) delayed rectifier potassium currents, are predominantly present in humans. Moreover, I_K slow1, I_K slow2 and steady-state non-inactivating K^+ current (I_{SS}), are involved in repolarization phase only in mouse CMs and completely absent in human cells (Davis, van den Berg et al. 2011).

6.2.7. iPSCs applications

Being derived from donor/patient-specific cells, iPSCs are a useful tool for a wide variety of applications in biomedical research as diseases modelling and drug screening (Fig. 11); at the same time, use of these cells overcome the ethical issues associated with the manipulation of human embryos and embryonic stem cells. Furthermore, iPSC technology also represents a potential source of autologous cells for transplantation (Scheiner, Talib et al. 2014; Singh, Kalsan et al. 2015).

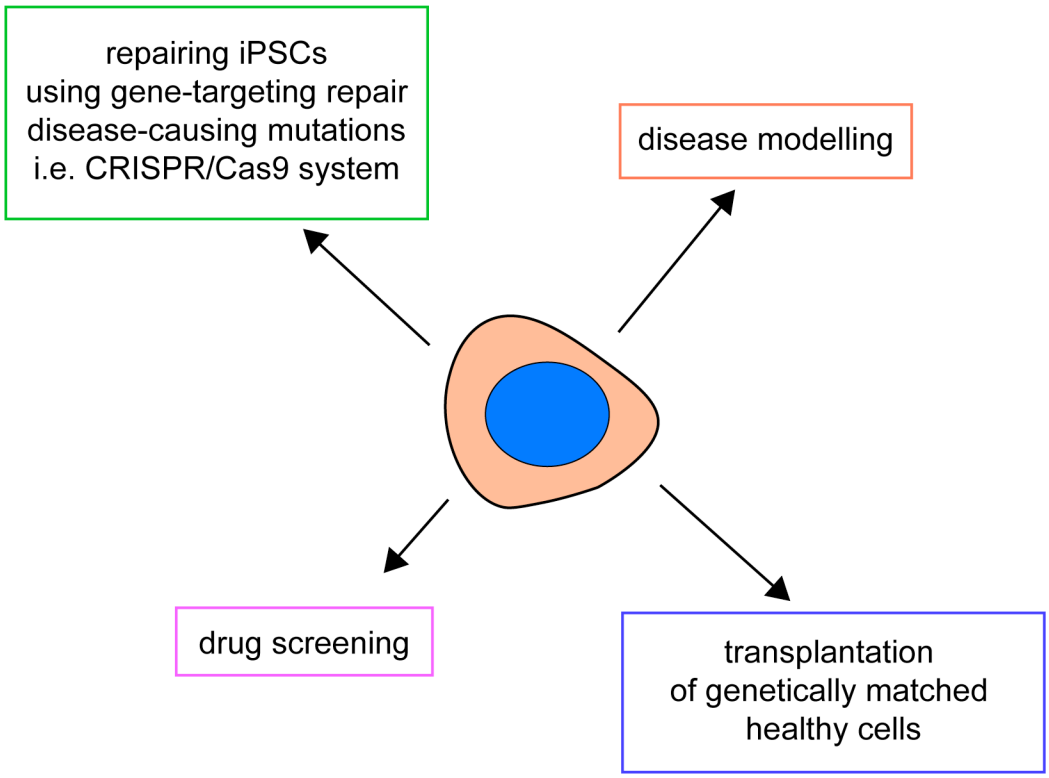

Figure 11. Schematic representation of iPSCs applications in biomedical research.

Their ES-like features, as unlimited proliferation, self-renewal and wide differentiation potential, allow the employment of iPSCs in tissue damage repair, *in vitro* modelling of diseases and as a platform for drug-testing. In the past years, several models of iPSCs have been generated to recapitulate different diseases in patient-specific relevant cell types, such as neurons for several neurological disorders, skeletal muscle and cardiomyocytes for dystrophies, arrhythmic disorders and cardiomyopathies, including those related to laminopathies (Park, Zhao et al. 2008; Moretti, Bellin et al. 2010; An, Zhang et al. 2012; Sun, Yazawa et al. 2012; Priori, Napolitano et al. 2013; Drawnel, Boccardo et al. 2014; Li, Fujimoto et al. 2015; Lodola, Morone et al. 2016; De Santis, Santini et al. 2017; Crasto and Di Pasquale 2018; Long, Li et al. 2018).

Furthermore, improvements in genome-editing technologies (Malik and Rao 2013; Hockemeyer and Jaenisch 2016) have been the key to overcome the limits of iPSC-based disease modelling and to allow the establishment of a causal link between a genetic mutation and the "clinical" phenotype of the iPSC-derived cells. On regard of their use in the clinic, although still at very early stage, some clinical trials using ESC-derived cells have been approved by the Food and Drug administration (FDA) (Goldring, Duffy et al. 2011), paving the way for the future clinical application of iPSCs. Very recently few studies reported transplantation of cells derived from patient-specific iPSC for treatment of macular degeneration and Parkinson disease (Mandai, Watanabe et al. 2017).

6.2.8. iPSC-based models of LMNA-CMP

At the moment, only three studies have been reported that employed iPSC-CMs to model LMNA-CMP; those are mostly derived from patients carrying nonsense mutations (R225X, GCCA insertion, Q354X and T518 frameshift) and have been shown to recapitulate some of the morphological and functional defects typical of laminopathy.

In addition to the well-known morphological defects of the nucleus caused by *LMNA* mutations, increased susceptibility to electrical and physical stresses was reported in LMNA-CMs, an effect that Siu and colleagues reported as mediated by alteration of ERK1/2 signalling pathway (Siu, Lee et al. 2012). Accordingly, abnormalities of ERK1/2 pathway were also described in iPSC-derived CMs carrying the *p.*R190W *LMNA* mutation in association with α-sarcomeric actinin disorganization (Chatzifrangkeskou, Yadin et al. 2018).

Remarkably, a recent study reported a beneficial effect of ataluren (PTC124), small molecule has been approved by the FDA for treatment of genetic diseases due to nonsense mutations, on the typical cellular phenotypes of LMNA-CMs and excitation-contraction coupling, setting the ground for a wider application of these models for pharmacological testing for laminopathies' treatment.

However, studies conducted so far were mostly phenomenological, while those focused on the molecular mechanisms underlying *LMNA* mutations in cardiac cells and the epigenetic role of LaminA/C in this context are almost absent.

A summary of the iPSC-based LMNA-CMP models reported so far is given in the Table 4.

LMNA mutation	iPSC-derived cell type	Phenotypes	References
GCCA insertion	FBs	Nuclear blebbing, cellular senescence, slow proliferation, electrical induced apoptosis	(Ho, Zhou et al. 2011)
R225X; GCCA insertion	CMs	Nuclear abnormalities, ERK1/2-mediated susceptibility to electrical stimulation	(Siu, Lee et al. 2012)
R225X; Q354X; T518fs frame shift mutation	CMs	R225X-CMs: improved senescence, apoptosis, excitation-contraction coupling and contractile functions induced by PTC124 treatment	(Lee, Lau et al. 2017)
R190W	CMs	Sarcomeric disorganization, abnormal activation of ERK1/2 signalling	(Chatzifrangkeskou, Yadin et al. 2018)

Table 4. iPSC-based model of *LMNA*-CMP. (*Adapted from Crasto S, Di Pasquale E., 2018)*.

7. AIMS AND RATIONALE

LaminsA/C are ubiquitous proteins and, together with Lamins B, constitute the main components of nuclear lamina which is critical for the maintenance of the shape and the mechanical stability of the nucleus; they also have key roles in other cellular processes, as transcriptional regulation and chromatin organization (Worman 2012).

Mutations in their encoding gene, *LMNA*, lead to a heterogeneous spectrum of human diseases collectively called laminopathies; based on their clinical manifestations, *LMNA*-related diseases can be classified into those that affect the striated muscle, the adipose tissue and the peripheral nerves or cause systemic diseases, that interest multiple organs and are mainly associated with accelerated ageing (progeria) (Muchir, Pavlidis et al. 2007). Cardiac involvement is very common in laminopathies and mainly manifests with dilated cardiomyopathy (DCM), usually associated with various conduction system diseases (CSDs).

Dilated cardiomyopathy (DCM) is a form of heart disease, associated with systolic dysfunction and contractile defects; when DCM is due to *LMNA* mutations, these clinical signs are typically anticipated by CSDs.

How different mutations in LaminA/C gene can cause such a broad spectrum of diseases still remains largely undetermined. With respect of the cardiac pathology, the molecular mechanisms underlying the onset and progression of the *LMNA*-dependent cardiomyopathy (CMP) as well as the role played by the nuclear envelope on its pathogenesis are still not completely understood. It is therefore crucial to better define how lamins work within the cardiomyocyte (CM) and how mutations impact on their functionality. Studies on *Lmna* knock-out mice and transgenic models carrying specific *Lmna* mutations have given an important contribution to shed light on the pathogenetic role of Lamin A/C. However, despite the gained knowledge, human studies so far have mainly focused on fibroblasts, adipose and muscular cells, while the functional and molecular effects of defective

LaminA/C in the human CMs as well as their role in the pathogenesis of the related CMP remain poorly understood. Furthermore, several important differences exist between mouse and human heart physiology, such as electrical properties, ion channel distribution, and heart rate, thus the use of mouse models may fail in reproducing some of the phenotypes as in the patients. Use of induced pluripotent stem cells (iPSCs) can overcome those limitations, allowing the generation of either patient-specific or isogenic cells of any type, including CMs, in which mechanisms of human diseases may be investigated (Takahashi, Tanabe et al. 2007; Yu, Vodyanik et al. 2007; Park, Zhao et al. 2008; Di Pasquale, Lodola et al. 2013; Lodola, Morone et al. 2016).

In this study we employed iPSC technology to dissect cellular and molecular mechanisms of cardiomyopathy due to LaminA/C mutations. The expected outcome of the proposed study is to gain knowledge on the biological functions of LaminA/C in the onset and progression of *LMNA*-dependent CMP (*LMNA*-CMP) and to dissect the molecular and functional mechanisms responsible for the disease phenotype. The specific aims of this Thesis are the followings:

1) To generate iPSC-based models of *LMNA*-CMP, either from patients or through gene editing, carrying K219T and R190W- *LMNA* mutations, for investigating their role in the pathophysiological context of the disease.

2) To determine the pathophysiological traits of *LMNA*-CMP in CMs derived from K219T and R190W-*LMNA*-iPSC lines. Study of CM phenotypes at the functional and molecular level through the combination of gene expression, electrophysiological, biomechanical and imaging techniques. Furthermore, gene correction studies, using CRISPR/Cas9 approach, will provide the causal link to the disease phenotype.

3) To define the role of LaminA/C and its mutation in transcriptional regulation. A special emphasis is given to the role of LaminA/C and the lamina-associated domains

(LADs) in structural organization and epigenetic regulation of the chromatin in the CMs. While it is generally accepted that the nuclear lamina functions to maintain the shape of the nucleus, it has also been demonstrated to play a role in the regulation of gene expression, by interacting with transcription factors and chromatin regulators.

4) To validate the use of the generated iPSC-derived models of *LMNA*-CMs as a platform for drug testing. We will perform a series of *proof-of-concept* experiments to test the effect of a small molecule (Remodelin), recently described to improve morphological traits of laminopathic cells, assessing its therapeutic potential on identified functional outcomes. Results from these experiments will provide us with evidence whether the generated models are suitable for drug screening approaches.

8. CHAPTER METERIALS and METHODS

8.1. iPSCs generation

8.1.1. Cell Reprogramming using STEMCCA lentiviral vector

Reprogramming of K219T *LMNA* fibroblasts was achieved by transduction of the four "Yamanaka" factors (Oct4, Sox2, Klf4 and c-Myc) using the STEMCCA lentiviral vector (Sommer, Stadtfeld et al. 2009), kindly provided by Dr. Mostoslavsky (Boston University School of Medicine, MA, USA). In brief, 1x 10^5 fibroblasts isolated from skin biopsies of 3 members of a family carrying the *p.*K219T Lamin A/C mutation were infected with STEMCCA lentiviral vector, for generated iPSC lines (referred as K219T#1, K219T#2 and K219T#3). iPSCs were also generated from two healthy wild-type family members and used as controls

8.1.2. Cell reprogramming using Sendai virus

An additional case carrying the *p.*R190W Lamin A/C mutation was also enrolled in the study and iPSCs were generated from peripheral blood mononuclear cells (PBMNCs) using a commercially available kit, based on Sendai virus (CytoTune™-iPS 2.0 Sendai Reprogramming Kit # A16517, Thermo Fisher Scientific), as described (Seki, Yuasa et al. 2012).

8.1.3. iPSC lines characterization and maintenance

iPSCs characterization was performed as previously described by us (Di Pasquale, Lodola et al. 2013; Lodola, Morone et al. 2016) and included: analyses of expression of pluripotency markers (OCT4, REX1, DNMT3B, TRA1-60, SSEA4) either by real time PCR, FACS analysis or immunofluorescence, assessment of alkaline phosphatase activity, embryoid bodies and teratoma formation assays to assess the ability of reprogrammed cells to differentiate into derivatives of the three germ layers, respectively *in vitro* and *in vivo*. Analysis of the karyotype was also carried out by standard procedures (Paulis, Castelli et al. 2015). Two clones per patient were used for the experiments. Cells were maintained under 5% CO2 in Essential 8 medium on Vitronectin (both from ThermoFisher Scientific) and passaged 1:5 when 90% confluence was reached (approximately 4-5 days) using 0.5mM EDTA after pre-treatment with 10 μM Rho-associated protein kinase inhibitor (Rocki from Selleck Chemicals).

8.1.4. Generation of gene-corrected isogenic lines

Gene correction strategy has been developed in the laboratory of Prof. Charles E Murry, at the University of Washington (Seattle – USA) and generation of the isogenic lines performed in both laboratories.

In detail, a suitable endogenous "TTAA" site was identified in the third intron of *LMNA* gene (about 130 bp from mutations sites), as close as possible to both mutations. Then, we designed a single guide RNA (sgRNA) spanning the TTAA site, so that only the wild-type sequence could be cut by CRISPR/Cas9. This strategy allowed us to avoid inserting any additional mutation into the targeting vector homology arms (such as those classically used to disrupt the PAM site). The sgRNA was designed using mit.crispr.edu and had a score of 80%, indicating a very high in-silico predicted specificity (sequence without PAM site: 5'-CTACCAGCCCCACTTTAACC-'3). To further decrease the risk of CRISPR/Cas9 off-

target activity, we adopted the enhanced specificity SpCas9 (eSpCas9) developed by Dr. Feng Zhang and colleagues (Slaymaker, Gao et al. 2016). The sgRNA was cloned into the eSpCas9 plasmid (Addgene #71784) using a standard method, based on restriction digestion with BbsI followed by ligation of a double-stranded oligo (Ran, Hsu et al. 2013). The resulting plasmid was named eSpCas9_*LMNA*. Sequence was confirmed by Sanger sequencing, and the sgRNA was validated to have a high on-target activity as measured by T7E1 assay in HEK293 cells. The *LMNA* targeting vector was made starting from the MV-PGK-Puro-TK_SGK-005 plasmid (Transposagen), which contains a piggyBac transposon encoding a PGK-EM7 promoter- driven a dual positive/negative selection cassette (puromycin N-acetyltransferase, ensuring resistance to puromycin, and truncated thymidine kinase, conferring sensitivity to ganciclovir or its analogue fialuridine). First, the piggyBac cassette was excised using NsiI and BsiWI and isolated. Then, a backbone with ends suitable for the subsequent overlap-based assembly was obtained from this same plasmid after removal of the piggyBac cassette using NotI and AscI. Finally, these two fragments were re-assembled together with two PCR products representing the 5' and 3' homology arms to the *LMNA* gene. The two homology arms were approximately 1 Kb long, and were amplified from genomic DNA of RUES2 human embryonic stem cells (hESCs) using primers:

5'-

GGTCCCGGCATCCGATACCCAATGGCGCGCCCGTACTTCAGGCTTCAGCAGT-3'

and 5'-

AAAGAGAGAGCAATATTTCAAGAATGCATGCGTCAATTTTACGCAGACTATCT

TTCTAGGGTTAACCTGGGAGCTGAGTGC-3' (for the 5' homology arm);

5'-

AATTTTACGCATGATTATCTTTAACGTACGTCACAATATGATTATCTTTCTAGG

GTTAAAGTGGGGCTGGTAGTG-3'

and 5'-

CGAATGCGTCGAGATATTGGGTCGCGGCCGCCCTGTCACAAATAGCACAGCC-

3’ (for the 3’ homology arm). The four-way assembly reaction was performed using NEBuilder HiFi DNA Assembly Kit (New England Biolabs) according to the manufacturer’s instructions, and the resulting targeting plasmid was named pbLMNA_K219K. Sanger sequencing confirmed that the 3’ homology arm contained the wild-type K219K allele, while the remaining genomic sequence of both homology arms was identical to that of line *LMNA* #1_2 as no SNPs were identified. The cloning strategy was designed so that during PCR the “TTAA” site was inserted both at the end of the 5’ homology arm and at the start of the 3’ homology arm, ensuring that the piggyBac cassette contained within could be excised using transposase while leaving behind a single “TTAA” matching the original genomic sequence. For the first gene targeting step, 150,000 hiPSCs (line *LMNA* #1_2) were seeded in each well of 6-well plate and immediately transfected using GeneJuice (Millipore) according to the manufacturer’s instructions. Briefly, for each well 3 µl of GeneJuice was mixed with 100 µl of Opti-MEM (ThermoFisher Scientific) and incubated for 5 min at room temperature. 1 µg of DNA was added to the transfection solution (equally divided between eSpCas9 *LMNA* and pbLMNA_K219K), which was further incubated for 15 min at room temperature and finally added to the cell suspension. After 16 h from transfection, cells were washed with DPBS and cultured for another 3 days in Essential 8 medium. Media without penicillin/streptomycin was used from two days before transfections up to this point, and 10 µM Y-27362 (ROCK inhibitor; SelleckChem) was added during plating and left until the subsequent day to increase cell survival. Gene targeted cells were selected by adding 1 µg/ml puromycin to the media for 4 days; the dose was then reduced to 0.5 µg/ml. 10 µM Y-27362 was added for the first 48 h of selection. Puromycin was then maintained at all times until the second gene targeting step to prevent silencing of the piggyBack transgene. After approximately 10 days from the transfection, 5-10 individual and well-separated colonies could be identified in each well of the 6-well plate, indicating that they likely arose from clonal expansion of a single gene-edited hiPSC. Colonies were manually picked following gentle treatment with EDTA to facilitate their detachment from

the matrix, and individually expanded as individual lines. Clones were screened by genomic PCR using LongAmp Taq Polymerase (New England Biolabs) according to manufacturer's instructions, except that all reactions were performed using an annealing temperature of 63°C and an extension time of 2 min. The primer sequences are reported in Table 5. Junctional PCRs for both the 5' and 3' integration site (5'- and 3'-INT) were used to confirm site-specific integration, while locus PCRs were used to monitor the presence of residual wild-type alleles. This step allowed us to discriminate homozygous clones from heterozygous ones or mixed cell populations. Finally, PCRs of the targeting vector backbone (5'- and 3'-BB) were performed to exclude random integration of the plasmid in the genome. Homozygous clones with only on-target integration events were selected (3 out of the 12 lines screened). These positive clones were further characterized by Sanger sequencing of the 5'- and 3'-INT PCR product to confirm the presence of the wild-type K219K allele in homozygosity (2 out of 3 lines) and exclude other unwanted mutations elsewhere in the locus (absent in all lines). One clone was karyotyped by standard G-banding, which confirmed its genetic stability, and therefore selected for the second gene targeting step. This clone was named K219K-PB_cl14. To remove the piggyback cassette and restore the *LMNA* locus to its original form, K219K-PB_cl14 hiPSCs were transfected using GeneJuice (Millipore) as described above using 1 μg of excision-only piggyBac transposase expression vector (PBx; Transposagen). Puromycin was removed from the media the day before transfection, and subsequently omitted. After 3 days from the transfection, the population was passaged as single cells, and 10,000 cells seeded per 10 cm dish in the presence of 10 μM Y-27362. On the next day, 400 nM fialuridine was added for negatively select the cells still carrying the piggyBac cassette. 10 μM Y-27362 was added for the subsequent 48 h. Selection was maintained for 7 days; at that point 10-50 individual and well-separated colonies could be identified in each 10 cm dish. Individual colonies were isolated, clonally expanded and screened by genomic PCR as described above to identify those with homozygous reconstitution of the wild-type allele (3 out of 15 screened lines). These were further

characterized by direct sequencing to ensure that the sequence surrounding the "TTAA" site was faithfully reconstituted upon piggyBac excision. The three clones were karyotyped by standard G-banding, which confirmed their genetic stability. Subsequent functional experiments were conducted on two of those (#F4 and #F6), named K219T-corrected.

PCR	Primer	Sequence	Location	Band WT (bp)	Band TARGET (bp)	Band PLASMID (bp)
LOCUS /LoA	*LMNA_FW1*	CCCCTGCTCAAACA TCCT CA	Left to 5' HAR	2181	5260 or LoA	-
	LMNA_REV 1	TGCAA TCAGAGCTTCCCC AG	Right to 3' HAR			
5'-INT	*LMNA_FW1*	CCCCTGCTCAAACA TCCT CA	Left to 5' HAR	-	1154	-
	PB3-P2	GCGACGGATTCGCGCTAT TTAGAAAG	5' ITR			
5'-INT+ 5'-LOCUS	*LMNA_FW1*	CCCCTGCTCAAACA TCCT CA	Left to 5' HAR	1836	1154 (4915)	-
	PB3-P2	GCGACGGATTCGCGCTAT TTAGAAAG	5' ITR			
	LMNA_REV 2	CTGTGGTTGTGGGGACAC TT	3' HAR			
3'-INT	*PB5-P2*	CGTCAATTTTACGCATGA TTATCTTTAAC	3' ITR	-	1173	-
	LMNA_REV 1	TGCAA TCAGAGCTTCCCC AG	Right to 3' HAR			
3'-INT + 3'-LOCUS	*LMNA_FW2*	CCCAAAAGTACCCCAGGC AT	5' HAR	1900	1173 (4979)	-
	PB5-P2	CGTCAATTTTACGCATGA TTATCTTTAAC	3' ITR			
	LMNA_REV 1	TGCAA TCAGAGCTTCCCC AG	Right to 3' HAR			
5'-BB	*M13-R49*	GAGCGGATAACAATTTCA CACAGG	Plasmid 5'	-	-	1157
	PB3-P2	GCGACGGATTCGCGCTAT TTAGAAAG	5' ITR			
3'-BB	*PB5-P2*	CGTCAATTTTACGCATGA TTATCTTTAAC	3' ITR	-	-	1127
	M13-F43	AGGGTTTTCCCAGTCACG ACGTT	Plasmid 3'			

Table 5. List of primer used for the characterization of CRISPR/Cas9 gene-edited human iPSCs.

8.2. Cardiac differentiation

iPSCs were differentiated into iPSC-CMs using a monolayer differentiation protocol (Nakahama and Di Pasquale 2016) and were maintained in a 5% CO2/air environment. In brief, iPSC colonies were dissociated with Accutase (Gibco-Life Technologies) and plated at a density of 0.25-0.5 x $10^5/cm^2$ in 12-well plates coated with Growth Factor Reduced (GFR) Matrigel (BD Bioscience) in Essential 8 medium containing 10μM Y-27362 (Selleck Chemicals). Cells were cultured until they reached 85-100% confluence (approximately 4 days) and then treated for 24 hours with 10-12μM CHIR99021 (Selleck Chemicals) in RPMI supplemented with B27 without insulin (the day of the treatment is referred to as day 0). On day 3, cells were treated with 5μM IWR-1 (Sigma Aldrich) for 48 hours. Medium was replaced on days 5 and 7 with RPMI+B27 without insulin; from day 10, RPMI supplemented with B27 and insulin was used and changed every other day. Cells were used for the experiments 20-25 days after the start of spontaneous contractions. Data presented are average of values obtained in CMs differentiated from two iPSCs lines per subject.

8.2.1. Remodelin treatment

iPSC-CMs were treated with the NAT10 inhibitor, Remodelin (cyclopentylidene-[4-(4-cyanophenyl)thiazol-2-yl)hydrazine) at final concentration of 5μM for 5 days (Larrieu, Britton et al. 2014), starting from day 20 after first contractions; medium supplemented with the small molecular was replaced every 2 days. Cells were harvest at day 6 after treatment and analysed.

8.2.2. FACS analysis

iPSCs differentiation efficiency was evaluated by FACS through the assessment of expression of the cardiac-specific marker α-sarcomeric actinin as previously described (Lodola, Morone et al. 2016). In brief, CMs were enzymatically dissociated into single cells, fixed in 1% paraformaldehyde and permeabilized; staining and detection were then performed using mouse monoclonal α-sarcomeric actinin antibody (1:400 from Abcam, Cambridge, UK) and goat anti-mouse Alexa-647-conjugated antibody (1:500 from Molecular Probes, Thermo Scientific), respectively. Dead cells were quantified and excluded from the analysis using the LIVE/DEAD fixable aqua stain kit (Molecular Probes, Thermo Fisher Scientific). Cell acquisition was performed on a FACS LSRFortessa flow cytometer (BD Bioscience, San Jose, CA, USA) and data analysed using DIVA software (BD Pharmingen, San Diego, CA, USA).

8.3. Electrophysiological Analysis

8.3.1. Patch-clamp recordings

Electrophysiological recordings were performed using a Multiclamp 700B patch-clamp amplifier (Molecular Devices) controlled by pClamp 10.3 software (Molecular Devices). Low-density cell cultures grown on glass coverslips (VWR international) were transferred 2-3 days after cell seeding to a custom-made experimental chamber that was fixed to the stage of an inverted microscope (Nikon eclipse, Ti/U) and superfused at 1.5 mL/min. Single human iPSC-derived cardiomyocytes (iPSC-CMs), identified on the basis of their typical morphology, were current/voltage-clamped in the whole-cell configuration of the ruptured patch-clamp technique. Data were collected from a minimum of three independent differentiations per line. Na^+ current (I_{Na}) and action potential (AP) signals were low-pass filtered at 10 kHz, digitized at 20 and 50 kHz, respectively, and stored for offline analysis whereupon the latter was performed using dedicated software (pClamp 10.6 and Clampfit 10.6; Molecular Devices). Patch pipettes were pulled from borosilicate glass capillaries (Intrafil-10, INTRACEL LTD) with a laser-based micropipette puller (P-2000; Sutter Instrument) and resistances ranging from 1 to 3 MΩ. After seal formation (2-10 GΩ), rupturing of the patch, and before I_{Na} measurement, adequate voltage control was achieved with membrane capacitance (Cm) and series resistance (Rs: 3–8 MΩ) compensation above 80% (estimated voltage error <5 mV in all cases), and by maintaining a fraction of channels in their inactivated state by using a holding potential of -90mV. Cm was determined by dividing the decay time constant of the whole-cell capacitance transient in response to hyperpolarizing steps from -50 mV, by the Rs. Statistical comparisons were made using Student's t-test for unpaired samples. Differences with at least $p<0.05$ were considered significant.

Patch clamp recording were performed by the Electrophysiology Unit of the Institute.

8.3.2. Action potential properties measurements

AP characteristics were assessed at 36°C using Hanks' balanced salt solution (HBSS, Sigma) containing: 137 mmol/L NaCl, 5.4 mmol/L KCl, 1.3 mmol/L $CaCl_2$, 1.2 mmol/L $MgSO_4$, 4 mmol/L $NaHCO_3$, 0.5 mmol/L KH_2PO_4, 0.3 mmol/L NaH_2PO_4, 5.5 mmol/L D-glucose and 10 mmol/L HEPES (pH 7.40 with KOH). The pipette filling solution contained: K-aspartate 120mmol/L, NaCl 10 mmol/L, MgATP 3 mmol/L, $CaCl_2$ 1 mmol/L, EGTA 10 mmol/L, HEPES 5 mmol/L (pH 7.2 with KOH). Liquid junction potential corrections (12.4 mV as calculated by pCLAMP software; Axon Instruments) were applied after experiments during offline analysis. AP measurement experiments were conducted on spontaneously active iPSC-CMs. Maximal upstroke velocity (dV/dt_{max}), peak voltage (Overshoot), action potential amplitude (APA), action potential duration at 90% of repolarization (APD_{90}), and maximal diastolic potential (MDP) were analysed. APs were recorded from cells able to generate spontaneous APs, averaging the 2 last sequential APs obtained from 10 sec current-clamp recordings.

8.3.3. I_{Na} measurements

Whole cell I_{Na} recordings were conducted at room temperature in an extracellular solution containing: 70 mmol/L NaCl, 1.8 mmol/L $CaCl_2$, 90 mmol/L CsCl, 1.2 mmol/L $MgCl_2$, 10 mmol/L glucose, 10 mmol/L HEPES, and 0.001 mmol/L Nifedipine (pH 7.4 with CsOH) and pipette solution filled with: 130 mmol/L CsCl, 10 mmol/L NaCl, 1 mmol/L $CaCl_2$, 10 mmol/L EGTA, 5 mmol/L HEPES, 3 mmol/L Mg-ATP (pH 7.2 with CsOH). Potentials were corrected for the estimated change in liquid junction potential of 6 mV before experiments. Peak I_{Na} densities and the voltage-dependence of activation were characterized as follows: single cells were held at -90mV and 100 msec voltage steps were applied from -90 to +80mV in 5 mV increments with a cycle time between voltage steps of 3 sec. Voltage-dependence of inactivation was assessed by holding cells at various potentials from -130 to 15 mV

followed by a 50 msec test pulse to -20mV to elicit I_{Na} (holding potential of -90 mV). To take into account the variations in cell size, current amplitude was normalized to Cm and expressed as current density (pA/pF). Activation and inactivation curves were described by fitting experimental points with the Boltzmann equation to estimate the voltages of half-maximal activation and inactivation (V1/2) and each slope-1 factor (k).

8.3.4. Optical measurements of impulse propagation

Action potential propagation were assessed optically using 80µm width strand preparations loaded with the voltage sensitive dye di-8-ANEPPS (135 µmol/L for 4 minutes; Life Technology) as described previously (Miragoli, Gaudesius et al. 2006). Loaded preparations were mounted in a temperature-controlled chamber (University of Bern, CH) placed on the stage of an inverted microscope (Nikon Ti/U) and were superfused at 36°C with HBSS containing 1% FBS. Strands were recorded as spontaneously contracting or stimulated with a bipolar electrode placed ≥ 1 mm from the measurement site in order to permit action potential propagation to reach steady-state conditions at the recording site. Strands were stimulated for the entire duration of recording (4 seconds, 5 stimulus) by a stimulator (TTi 110, Harward Apparatus) at a basic cycle length of 500 ms or 1000 ms. Recordings were made at 10x magnification (S-Fluo 10x, 0.5 N.A., Nikon) allowing to monitor the activity of two strands in one field of view. Impulse propagation was acquired by a fast-resolution camera at 1-5 kHz temporal resolution (Ultima L, Scimedia, USA). The amplitude of optically recorded action potential upstrokes was scaled to 10% (dF/F). Conduction velocities were computed by calculating the activation times for a given strands and divided by the covered space of the propagation with a dedicated software (BrainVision AN 1812).

8.3.5. Evaluation of contraction force through IonOptix

iPSC-CMs were plated on 22mm glass and loaded with 5μM Fura-2 acetoxymethyl ester, Fura-2 AM (Molecular Probes Inc, Eugene, OR). The chamber was perfused with HBSS buffer supplemented with 10 mM Hepes and the temperature was constantly kept at 37°C. Electrical pulses were introduced through a field stimulator at the frequency of 0.5, 1 and 2 Hz. The chosen cell cluster was visualized by the IonOptix imaging software, in the edge detection mode. Two markers for the cell edges were positioned manually by the operator. The cell shortening and calcium transients were then recorded with the following protocols: spontaneous beating (baseline) followed by either electrodes stimulation or ß-adrenergic stimulus by isoproterenol (1μM).

8.4. Molecular Studies

8.4.1. Gene expression studies

Total RNA was extracted with Trizol Reagent and quantified using Nanodrop (NanoDrop 2000c Spectrophotometer, Thermo Fisher Scientific). RNA was reverse transcribed with SuperScript VILO cDNA Synthesis Kit (Thermo Fisher Scientific) according to the manufacturer's instructions. Quantitative reverse transcriptase PCR (qRT-PCR) was performed using SYBR Select Master Mix for CFX (Thermo Fisher Scientific) and the relative expression calculated as $2^{-\Delta\Delta Ct}$ using the comparative Ct method using 18S or HGPRT as housekeeping controls. Specific primer sequences are summarized in Table 6.

Primers sequences used for gene expression experiments		
SCN5A	F: 5' GAGCTCTGTCACGATTTGAGG 3'	R: 5' GAAGATGAGGCAGACGAGGA 3'
CX40	F: 5' GGCTCACTGTCCTCTTCATATTC 3'	R: 5' CACACATAGGTGTTGAGCAGAGT 3'
CX43	F: 5' TGAGCGGGTGGTAATTGTGG 3'	R: 5' TGGAGGGTCAGGCCTAGAAA 3'
TBX3	F: 5' AGCAGCTTTCAACTGCTTCG 3'	R: 5' CCATGCTCCTCTTTGCTCTC 3'
TBX5	F: 5' GCATGGAGGGAATCAAAGTG 3'	R: 5' CGTCGGCAGGTACAATGTC 3'
HGPRT	F: 5' GACCAGTCAACAGGGGACAT 3'	R: 5' CTGCATTGTTTTGCCAGTGT 3'
18S	F: 5' CGCAGCTAGGAATAATGGAATAGG 3'	R: 5' CATGGCCTCAGTTCCGAAA 3'
TRIM63	F: 5' CAGCTGGACAAGTCCACAAA 3'	R: 5' CAAAGCCCTGCTCTGTCTTC 3'
TNNT2	F: 5' ACTGAGCGGGAAAAGAAGAA 3'	R: 5' CTCCTGCAGGTCGAACTTCTC 3'
MYH6	F: 5' TGGGTTTGGACCAAGATGAT 3'	R: 5' CATCACGAGCATTGTTTGCT
MYBPC3	F: 5' CGGGTGGAGTTTGAGTGTG 3'	R: 5' CGTCCTTCTTGAACCGGTATT 3'
DESMIN	F: 5' GTATGAGACCATCGCGGCTA 3'	R: 5' GGCGTCGTTGTTCTTGTTG 3'

Table 6. Sequences of the primes used in the gene expression experiments.

8.4.2. Western Blot

Protein lysates (30μg) from CNTR- and LMNA-CMs were loaded on precast polyacrylamide gels (Bolt 4-12% Bis-Tris Plus Gels, Invitrogen) and transferred to nitrocellulose membranes. Membranes were blocked with 5% milk in TBS-0.1% Tween for 1 hour at room temperature and then incubated overnight with primary antibodies (anti-$Na_v1.5$ 1:1000 from Cell Signaling, D9J7S; anti-β-actin 1:2000 from Santa Cruz, sc1615). Detection was performed after 1-hour incubation with the appropriate secondary antibody (1:2000) using the Millipore Chemiluminescent HRP substrate kit. Quantification of $Na_v1.5$ level was determined by densitometric analysis relative to β-actin, using Fiji-ImageJ software.

8.4.3. Co-immunoprecipitation (Co-IP) experiments

Co-IP was performed as previously described (Cesarini, Mozzetta et al. 2015). In brief, nuclear extracts were obtained using PARISTM KIT (Ambion AM1921). 0.5 mg of nuclear extracts were immunoprecipitated overnight at +4° with 5 μg of antibodies (Lamin A/C, Santa Cruz mAb sc-7292-x; unrelated IgG) in a nuclei lysis buffer (10mM Hepes, pH 7.5, 1.5mM $MgCl_2$, 150mM KCl, 10% glycerol, 0.2% NP-40, 1mM DTT, and protease inhibitors). Eluates were analysed by western blot as described above, using anti-Lamin A/C (Santa Cruz mAb sc-7292-x) and anti-EZH2 (ACTIVE MOTIF mAb catalogue #39875, AC22 clone) antibodies.

8.4.4. Immunofluorescence

iPSC-CMs were dissociated and plated onto glass cover-slips coated with fibronectin and laminin. Cells were prepared for staining by fixing in 4% paraformaldehyde; cells were then rinsed with PBS-0.1% Tween, blocked with 3% goat serum, and permeabilized with 0.1%

Triton X-100 for 1 hour at room temperature. Cells were then incubated overnight at +4°C with the primary antibodies: anti-$Na_v1.5$ channel (anti-rabbit from Alomone, #ASC005; 1:100) and anti-α-sarcomeric actinin (Abcam EA-53 ab9465, 1:100). For the detection, cells were washed three times with PBS-0.1% Tween and incubated for 1 hour at room temperature with Alexa-Fluor 488- and 555-coniugated secondary antibodies (Molecular Probes from Thermo Scientific) raised in the appropriate species for the experiments. Nuclei were stained with DAPI. Images were acquired on an Olympus FV1000 confocal laser-scanning microscope with x60 oil immersion objective and analysed using ImageJ Fiji software. For tissue immunofluorescence staining, paraffin-embedded heart sections (3μm thick) from three healthy controls (commercially available from Proteogenex) and four patients were used. Paraffin was removed from tissue sections with sequential treatment with xylene, 100% EtOH, 95% EtOH, and 70% EtOH, and slides subsequently rehydrated with ddH2O. Prior to immunostaining, we performed antigen retrieval by leaving sections at 98°C for 25 minutes in citrate. Slides were blocked with 3% goat serum and permeabilized with 0.3% Triton X-100 for 40 minutes at room temperature. Tissue sections were then washed three times with PBS-T (Tween 0.05%) for 5 minutes and then incubated overnight at +4°C with primary antibodies (anti-rabbit $Na_v1.5$, 1:100, from Alomone, #ASC005; anti-mouse α-sarcomeric actinin, 1:100, from Abcam, EA-53 ab9465). After 3 washes with PBS-0.1% Tween, slides were incubated with secondary antibodies for 1 hour at room temperature (Alexa Fluor 555-coniugated goat anti-rabbit, 1:500; Alexa Fluor 488-coniugated goat anti-mouse, 1:500, both from Molecular Probes). Nuclei were detected with DAPI. Images were acquired at x100 on an Olympus FV-1000 confocal laser-scanning microscope with an oil immersion objective and analysed using ImageJ Fiji software.

8.4.5. Stimulated emission depletion (STED) microscopy

iPSC-CMs were plated on glass coverslips (18mm, #1.5) and prepared for staining by fixing in 2% paraformaldehyde. Cells were then rinsed with PBS-0.1% Tween, blocked with 3% goat serum, and permeabilized with 0.1% Triton X-100 for 1 hour at room temperature. Cells were then incubated overnight at +4°C with the primary antibodies: anti- Lamin A/C (anti-mouse, from Santa Cruz 7292-X, 1:250) and anti-Suz12 (anti-rabbit, from Cell Signalling #3737, 1:250). After three washes with PBS-0.1% Tween, cell were incubated for 1 hour at room temperature with Abberior STAR-RED and STAR 580-conjugated secondary antibodies raised in the appropriate species for the experiments. Images were acquired on a Leica TCS SP8 STED 3X microscope in "counting mode" with a 100x oil immersion objective, using detection-lasers at wavelengths of 634 and 561 nm and 775 depletion-laser, with a z-step of 60nm. Colocalization analysis was performed with Imaris software (Bitplane). We measured the number of voxels on the 3D reconstructions of Lamin A/C-Suz12 colocalization channel. Statistical analysis was performed using an unpaired Mann-Whitney test with 95% confidence interval.

8.4.5.1. Distance distribution analysis

PRC2-LaminA/C distribution profile was calculated using the "Distance transformation" Xtension of Imaris Bitplane11. Spot option was used to count point-like objects in all acquired z-stacks. LaminA/C, Suz12 and colocalization channels were re-created using spot settings and visualized as "spheres" with an estimated XY diameter of 0.227 μm and a threshold quality above 0.800 fluorescent signal for Lamin A/C; and XY diameter of 0.227 μm and a threshold quality above 0.300 fluorescent signal for Suz12 and colocalization channels. The outside "ring of spots" of Lamin A/C was selected and used as the "nucleus edge" to calculate Suz12 and colocalization channel distances and distributions within

nuclei. Data were further analysed by dividing cell nuclei into three zones of 2.15 μm in length from the periphery to the centre.

8.4.6. 3D- DNA immuno-FISH

Immunofluorescence coupled with DNA in situ hybridization on preserved nuclei (3D DNA immuno-FISH) was performed on sterilized 18-mm round coverslips in 12-well tissue culture dishes. The nuclear lamina was visualized using an anti-Lamin A/C antibody (goat IgG, from Santa Cruz Biotechnology, sc-6215 N18). DNA hybridization probe was generated by nick translation (Nick translation DNA labelling system - Enzo Life Sciences) in the presence of Spectrum Orange dUTP nucleotide (Vysis) of the RP11-356A22 BAC (Children's Hospital, Oakland, CA) containing the sequence of the *SCN5A* gene. CNTR- and LMNA-CMs were fixed in 2% paraformaldehyde on slides. Cells were permeabilized and incubated for 30 min in blocking solution (3% normal rabbit serum, 0.4% Triton X-100). Cells were then incubated with the primary antibody (1:100) overnight at 4°C. After overnight incubation, samples were washed three times with PBS-Tween 0.1% and incubated with Alexa Fluor 488-coniugated secondary antibodies (Invitrogen, A-11078) diluted 1:500 for 1 h at room temperature. After rinsing, the samples were permeabilized with ice-cold detergent (0.7% Triton-100/0.1M HCl) and FISH was performed to detect *SCN5A* localization. The labelled probe was resuspended in hybridization buffer (50% formamide, 10% dextran sulphate, 1x Denhart's solution, 0.1% SDS, 40 mM Na_2HPO_4, pH 6.8, 2xSSC) containing a 10x excess of human Cot1 DNA (Life Technologies), and denatured at 80°C for 10 min. *In situ* hybridization was performed as previously described, with minor modifications (Paulis, Castelli et al. 2015; Paulis, Castelli et al. 2015). In brief, slides were denatured in 70% formamide/2xSSC at 78°C for 10 min, and hybridized for 48h at 37°C. Stringent washings were done with 50% formamide/2xSSC at 37°C. Slides were mounted with Vectashield mounting medium and DAPI, and then scored under an Olympus

FV-1000 confocal laser-scanning microscope at x100 with an oil immersion objective, using x2 optical zoom with a z-step of 0.3µm between optical slices. Distances between each *SCN5A* locus and the nuclear periphery were measured with Fiji-ImageJ software through a 3D distance map construction on the DAPI channel.

8.4.7. Chromatin immunoprecipitation (ChIP)

Differentiated iPSC-CMs were fixed in 1% formaldehyde for 10 min and then quenched with 0.125M glycine for 5 min. Fixed cells were lysed in IP buffer made from two volumes of SDS buffer (100mM NaCl, 50mM Tris-HCl pH 8.1, 5mM EDTA pH 8.0, 0.5% SDS), one volume of Triton buffer (100mM NaCl, 100mM Tris-HCl pH 8.1, 5mM EDTA pH 8, 5% Triton X-100) and protease inhibitors (Roche) for 10 min on ice. Chromatin was sonicated with a Bioruptor Diagenode Sonicator and immunoprecipitated overnight on a wheel at 4°C with 4µg LaminA/C antibody (anti-LaminA/C (636), from Santa Cruz Biotechnology, sc-7292x), 5µg of antibodies against the major histone modifications (anti-H3K4me3, from Active Motif, 39159; anti-H3K27me3, from Abcam, ab6002; anti-H3K9me3, from Abcam, ab8898) and anti-Suz12 antibody (Cell Signaling, #3737) at the 1:100 diluition. The bound complexes were washed with Mixed Micelle buffer (20mM Tris-HCl pH 8.0, 150mM NaCl, 5mM EDTA pH 8.0, 5% Sucrose, 1% Triton X-100, 0.2% SDS), Buffer 500 (50mM Hepes, 0.1% deoxycholic acid, 1% Triton X-100, 500mM NaCl, 1mM EDTA pH 8.0), and LiCl buffer (10mM Tris-HCl, pH 8.0, 0.5% deoxycholic acid, 0.5% NP40, 250mM LiCl, 1mM EDTA pH 8.0). Cross-linking was reversed by incubation at 65°C overnight in elution buffer (100mM $NaHCO_3$, 1%SDS), and DNA was extracted from Dynabead Protein G (Life Technologies) using the standard phenol/chloroform protocol and then resuspended in 20µl of ddH20. qPCR was performed in triplicate using SYBR Select Master Mix for CFX. Ct values were calculated by appropriated software and relative enrichment was calculated as ChIP/input ratio. Primer sequences are given in Table 7.

8.4.8. PAT-ChIP

Two 10μm sections of formal-fixed and paraffin-embedded (FFEP) heart tissue were used as starting material. The procedure was performed as previously described (Fanelli, Amatori et al. 2010) with modifications.

In brief, paraffin was efficiently removed with fresh Histolemon solution (Carlo Erba). Subsequently Histolemon was replaced with sequential 1ml washes of 100%, 95%, 70%, 50%, 20% ethanol and ddH_2O. For the chromatin extraction step, sections were resuspended in 500 μl of Lysis buffer (10mM Tris-HCl pH 7.4, 150mM NaCl, 3 mM $CaCl_2$, 2 mM $MgCl_2$, 0.5% Tween 20, 10 μg/ml RNAse A, 0.1 mM PMSF). The lysates were then resuspended in 200 μl of Digestion Buffer. Samples were sonicated four times with a 3-mm microtip probe at 25 W for 30 seconds on ice with a Branson 250. 1 U of micrococcal nuclease (USB, #70196Y) was added to every 10μg of preheated chromatin (3 minutes at 37°C) and incubated at 37°C for 1 minute. The digestion was stopped by addition of 0.5M EDTA to a final concentration of 12.5 μM. The sections were then resuspended in 200 μl of Extraction Buffer (10 mM Tris-HCl pH7.4, 150 mM NaCl, 3 mM $CaCl_2$, 2 mM $MgCl_2$, 0.1% SDS, 0.1 mM PMSF). Samples were sonicated for six times with a 3-mm microtip probe at 30 W for 20 seconds on ice. After the centrifugation step the supernatant containing purified chromatin was collected and stored in a clean 1.5 ml Eppendorf tube. The amount of chromatin was checked with Qubit (Thermo Fisher Scientific). For the immunoprecipitation step, 3μg of ChIP-grade antibody was added to 1μg of tissue chromatin in 500 μl of Incubation Buffer (20mM Tris-HCl pH 7.4, 5mM EDTA, 50mM NaCl, 0.1mM PMSF) and incubated in rotation (15 rpm) overnight at +4°C. The bound complexes were washed twice with 1 ml of ice-cold Washing Buffer A (20mM Tris-HCl pH 7.4, 5mM EDTA, 50mM NaCl) and 8 ml of the same buffer (containing Triton X-100) were added. After the centrifugation step, the pellet was washed with 10 ml of ice-cold Washing Buffer B (50 mM Tris-HCl pH 7.4, 10mM EDTA, 100mM NaCl) and 10ml of ice-cold Washing Buffer C

(50mM Tris-HCl pH 7.4, 10mM EDTA, 150 mM NaCl). The pellet was resuspended in 1 ml of ice-cold Washing Buffer C (without Triton X-100) and transferred to a clean 1.5 ml Eppendorf tube. The bound chromatin was eluted by addition of 300–500 µl 1% SDS in TE. 0.2 M NaCl was added to all samples (input and bound fractions) and samples incubated at 65°C overnight to reverse formaldehyde crosslinks. The next day, 10mM EDTA was added to all samples to a final concentration with 50mM Tris-HCl pH 6.5, 100 µg/ml Proteinase K and incubated at 45°C for 3 hours. The DNA was extracted from protein G-Sepharose (50% slurry, Zymed) with phenol-chloroform. qPCR was performed in triplicate using SYBR Select Master Mix for CFX. Ct values were calculated by appropriated software and relative enrichment was calculated as ChIP/input ratio. Primer sequences are summarized Table 7.

Primers sequences used for ChIP experiments		
ATCN2	F: 5' GGGCAAGATAGATTTCCCTTCT 3'	R: 5' AGGAGTTTGGGATGTGTGTTCT 3'
CX40	F: 5' ACAATGACTAAGAGCCCACAGAT 3'	R: 5' CTGCATAAAAGTGGGGTAAACTC 3'
CX43	F: 5' CAAACAGCAGCGGAGTTTTA 3'	R: 5' TGAAGTCACGCCAAGTGATT 3'
DEFA 3	F: 5' AACCTGAGGCAAAGATGGTG 3'	R: 5' CTGTCCTTCCAGCCTCTCAC 3'
DEFA 4	F: 5' TGCAGCGAGATTGGTGTTAG 3'	R: 5' AATAACCCAGGAGGGACCAC 3'
JUN	F: 5' ACTCTGAGCCCTTATCCAGC 3'	R: 5' AAAGAAGGGCCCGACTGTAG 3'
NANOG	F: 5' TTGTGGGCCTGAAGAAAACTAT 3'	R: 5' TCAAGAGGGAAATGATCCCTTA 3'
NEUROD	F: 5' GGGGTACTTGAGTGACACGACT 3'	R: 5' TGCCCCAGAATAGAAGCAATAA 3'
SCN5A	F: 5' TGCACACCCTTCCAATAACC 3'	R: 5' GGACAGTGGCAAATTGCAG 3'
SCN10A	F: 5' GGAAGAGGGTGAGGGAAAGC 3'	R: 5' TGTCACCAGTCCTTCCATGC 3'
TNNC1	F: 5' GGAGACAGTAATGGGGACTCAG 3'	R: 5' GGACAGTGATTCTGGTGTTTGA 3'
TBX3	F: 5' GCTTGTGAAACTGATCCCAAAGT 3'	R: 5' GGCCTTTGAAGACCATGGAG 3'
TBX5	F: 5' CGTTCATGAGAAGTAGCAGCAC 3'	R: 5' GGGGGAAATAGGTTTCTCTTTG 3'
TRIM63	F: 5' CATAGGAGGCACCTGGGTTA 3'	R: 5' AGGGGAGAGAGGAGAAGTCG 3'
TNNT2	F: 5' TCCAGGCTACTGGCTCCTAA 3'	R: 5' TCTGGCCTCCTGTAGCAGTT 3'

Table 7. Sequences of the primes used in the ChIP experiments.

8.4.9. Lentiviral-mediated Overexpression

For overexpression experiments, a lentiviral construct encoding C-terminus GFP-tagged LaminA/C carrying the K219T mutation (*c.*A656C) was obtained from Origene in the pLenti-EF1alpha-GFP vector (CW104035). We also generated a lentiviral construct encoding C-terminus GFP-tagged wild-type LaminA/C by subcloning the WT *LMNA* gene into the same pLenti-EF1alpha-GFP vector backbone. Lentiviral particles were produced in HEK293T cells and used to transduce iPSC-derived CMs as previously reported (Di Pasquale, Lodola et al. 2013). For LaminA/C overexpression experiments, transduction was performed between days 5 and 6 of the differentiation, a stage at which LaminA/C starts to be expressed in this system; cells were used for electrophysiology and for gene expression studies 20 days after the start of spontaneous beating. For gene expression, cells were sorted for GFP expression with a BD FACS ARIA III cell sorter and harvested for RNA extraction.

9. CHAPTER RESULTS

9.1. Generation of iPSC-derived models of *LMNA*-dependent Cardiomyopathy

Patient-specific iPSC lines were generated from three familial cases, carrying the *p.*K219T LaminA/C (c.A656C) heterozygous mutation (Fig.12), and diagnosed with Dilated Cardiomyopathy (DCM) in association with arrhythmogenic events (Roncarati, Viviani Anselmi et al. 2013). Patients' information is summarized in Table 8.

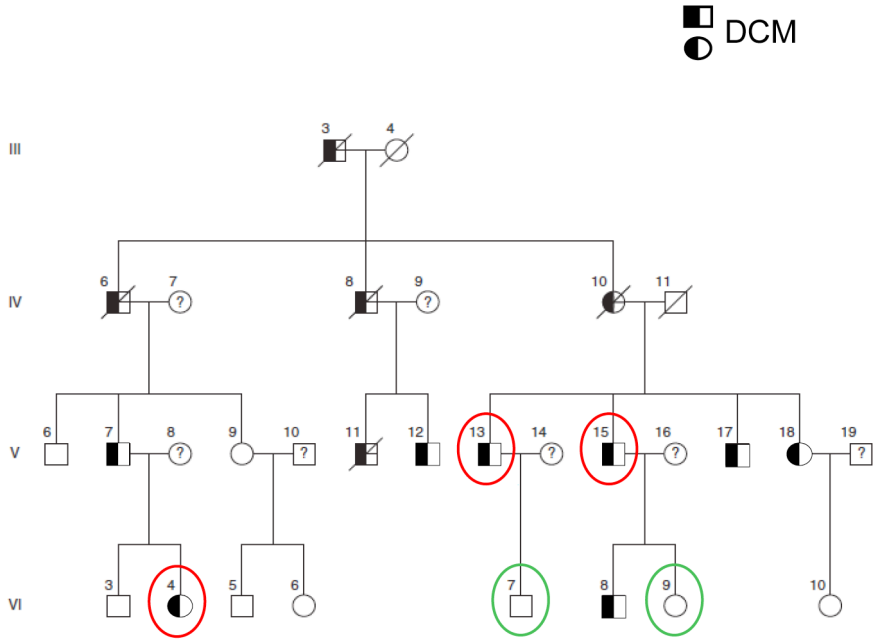

Figure 12. Family tree. iPSCs lines were generated from patients, carrying the K219T-LMNA mutation (red circles) and two healthy family members (green circles).

Patient code	Disorder	History of Arrhythmia	Gender	Age (years)	LMNA mutation
K219T#1	DCM	No	F	15	Yes
K219T#2	DCM	Yes	M	54	Yes
K219T#3	DCM	Yes	M	51	Yes
CNTR#1	healthy	No	M	29	No
CNTR#2	healthy	No	F	32	No
R190W	DCM	Yes	M	30	Yes

Table 8. **Summary of patients' information**. M: male; F: female.

iPSC lines were generated from fibroblasts isolated from patients' skin biopsies through the transduction of the four "Yamanaka" factors (*SOX2*, *OCT-4*, *KLF-4* and *c-MYC*) using STEMCCA lentiviral vectors, as previously described (Sommer, Stadtfeld et al. 2009). As controls, iPSC lines were also obtained from 2 wild type healthy family member.

An additional case carrying the *p.*R190W (**c.C568T**) *LMNA* heterozygous mutation was also enrolled in this study and iPSCs generated from peripheral blood mononuclear cells after their activation to T-lymphocytes.

The positions of the described *LMNA* mutations are graphically illustrated in the Fig.13-A.

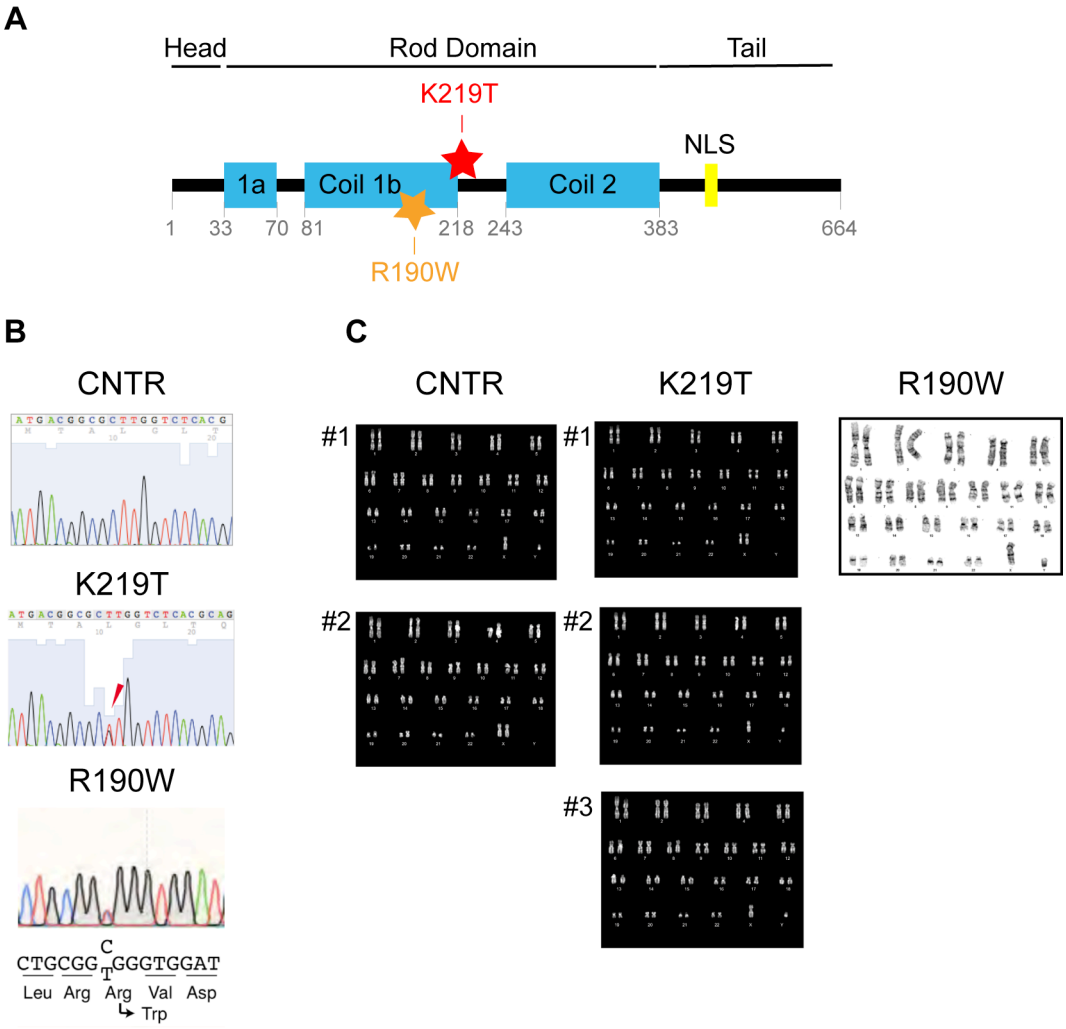

Figure 13. Genetic analyses of the *p*.K219T and *p*.R190W – LMNA mutations. (A) Schematic representation of the Lamin A protein structure, showing the localization of the *p*.K219T and *p*.R190W mutations. **(B)** Representative electropherograms from DNA sequencing of exons 3 and 4 of *LMNA* gene showing that the generated K219T LMNA-iPSC lines carried the alanine-to-cytosine transversion at position 656 (c.656A<C) in heterozygosity in exon 4 as in the patients (the reverse sequence is shown in the figure; the T<C mutation is indicated by the arrow) and that R190W LMNA-iPSC lines carried the cytosine to thymine transversion at position 568 (c.568C<T) in exon 3. CNTR iPSCs were wild-type. **(C)** Karyotype analyses confirming that the employed iPSC lines did not accumulate any major genetic abnormality during reprogramming.

As following step, a detailed characterization assessing the actual pluripotency of the generated lines and their genomic stability was performed (Fig. 14 and Fig. 15). iPSC colonies were stained with antibodies against the pluripotency markers OCT4 (green) SSEA4 (green) and TRA1-60 (red) (Fig.14-A and Fig.15-A) and tested for the alkaline phosphatase (AP) activity (Fig.14-C and Fig.15-C). Furthermore, we evaluated the expression of classic embryonic stem (ES) cell marker genes by real time qPCR (Fig.14-B and Fig.15-B) and the ability of iPSCs to differentiate into the three germ layers by teratoma formation assay.

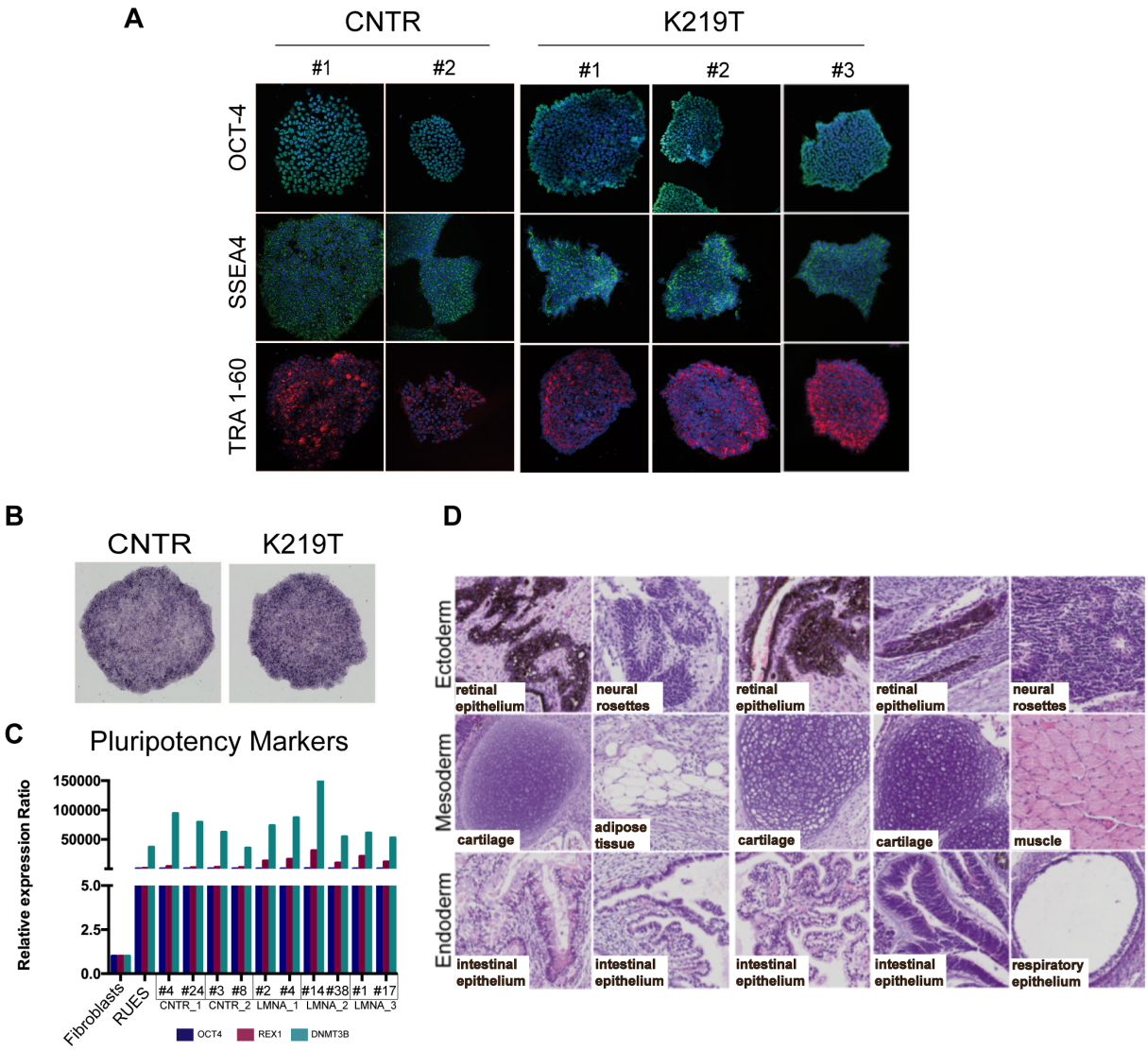

Figure 14. Characterization of the pluripotent state of iPSCs generated from patient-derived fibroblast with and without LaminA/C *p.*K219T mutation. **(A)** Immunofluorescence staining showing the expression of OCT4 and of the surface pluripotency markers SSEA4 and TRA1-60 in the generated CNTR- and K219T-iPSC lines. Nuclei were stained with DAPI. **(B)** Indicative images of AP activity in CNTR and K219T-LMNA iPSC lines. **(C)** qRT-PCR for *OCT4*, *REX1* and *DNMT3B* genes, showing the expression of the three markers of pluripotency in two lines per subject. Data are relative to parental fibroblasts and were normalized using HPRT as housekeeping gene. cDNA from the RUES2 ES cell line was used as a positive control. **(D)** Teratoma formation assay demonstrating the ability of the generated lines to differentiate *in vivo* into tissues originating from ectoderm (neural rosettes, retinal epithelium), mesoderm (cartilage, adipose tissue and muscle), and endoderm (intestinal or respiratory epithelium).

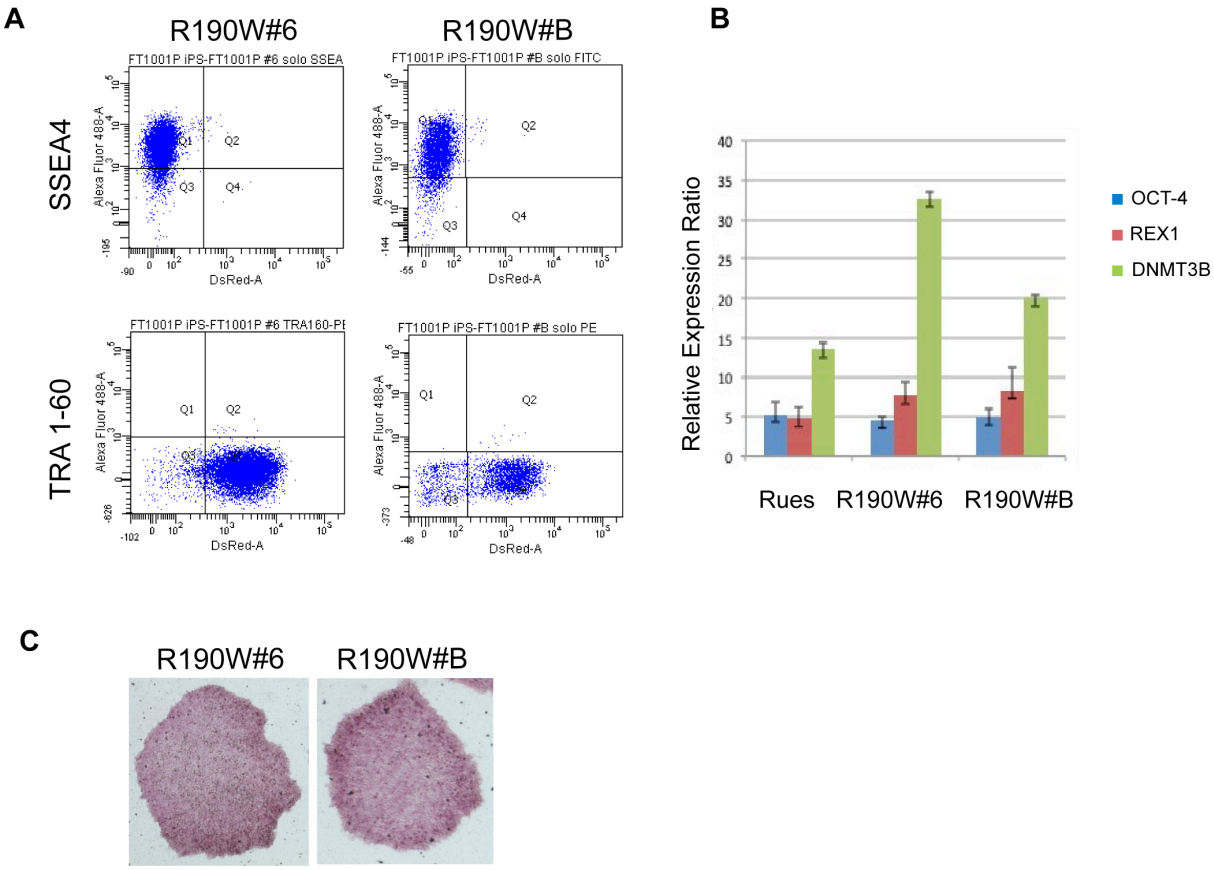

Figure 15. Characterization of R190W-iPSC lines. (A) Flow cytometry analysis of iPSCs to verify the expression of pluripotency markers SSEA4 and TRA1-60. **(B)** qRT-PCR for *OCT4*, *REX1* and *DNMT3B* genes, showing the expression of the three markers of pluripotency in two selected lines. **(C)** Indicative images of AP activity in two R190W-LMNA iPSC clones.

9.2. Cardiac differentiation and morphological analyses

Generated iPSCs were then differentiated into cardiomyocytes (CMs) for the functional and molecular studies. Cardiac differentiation has been achieved using a protocol optimized in the laboratory, which is based on the modulation of the WNT signalling pathway in a serum-free and chemically defined medium (Nakahama and Di Pasquale 2016) and allows the obtainment highly enriched iPSC-derived CMs (iPSC-CMs), reaching a differentiation efficiency of about 75-90%. The protocol is schematically described in the Fig.16. In brief, iPSCs were cultured until they reach 85-100% confluence (approximately 4 days from the seeding) and treated for 24 hours with 10-12μM (depending on the specific iPSC clone) CHIR99021, an activator of the WNT pathway, in RPMI+B27 supplement in absence of insulin. Then, on day 3 cells were treated with 5μM IWR-1 for 48 hours to inhibit the WNT signalling.

From day 10 cells were maintained in RPMI+B27 supplement with insulin and were cultured 20-30 days after spontaneous contractions start.

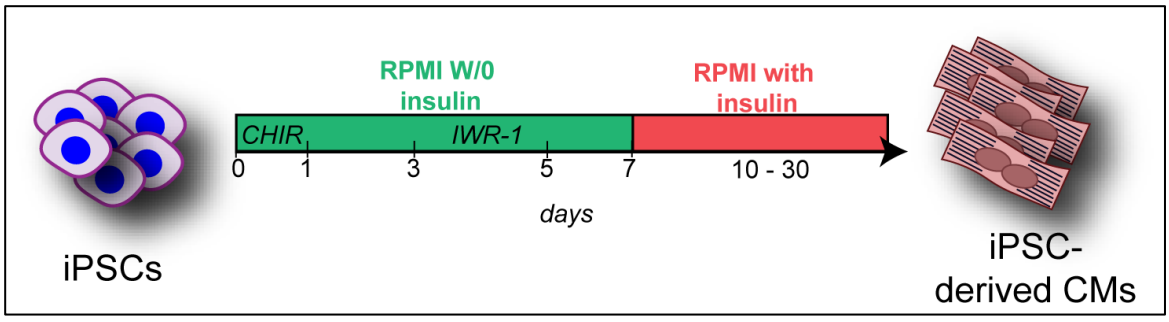

Figure 16. Cardiac differentiation protocol. The cartoon shows the steps of the differentiation protocol employed to obtain cardiomyocytes (CMs) starting from iPSCs.

The efficiency of differentiation into CMs was tested by FACS analysis through the evaluation of the expression of cardiac-specific marker α-sarcomeric actinin in all the generated cell lines (Fig. 17).

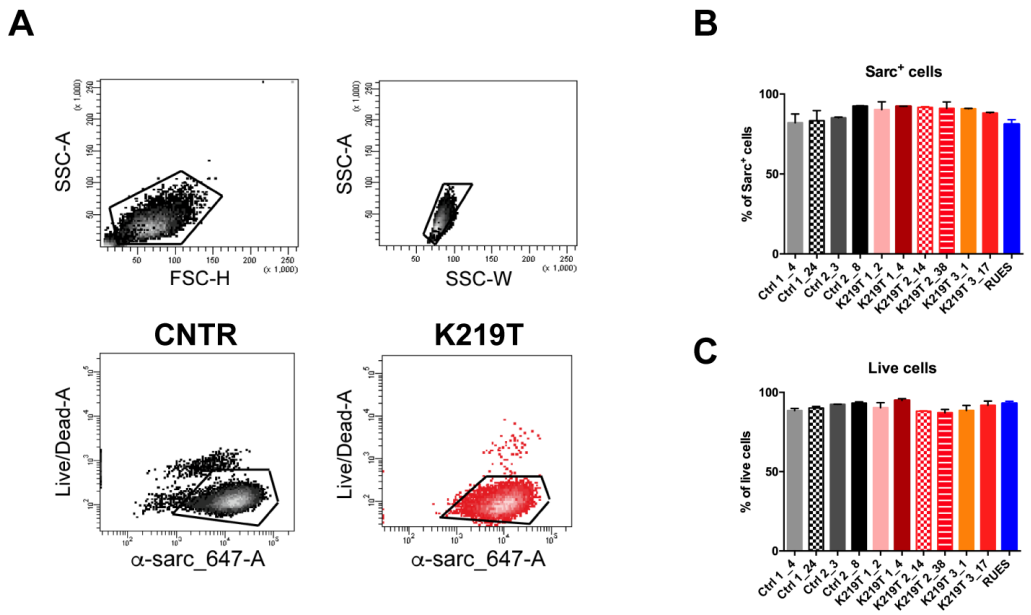

Figure 17. Flow cytometry analysis of iPSC-CMs. (**A**) Left: representative flow cytometry plots of human iPSC-CMs. Debris were excluded and cells were selected based on size (upper left panel). After exclusion of doublets (upper right panel) and dead cells, single live cells were analysed using a cardiac-specific antibody against sarcomeric α-actinin. Scatter plots and gates of a representative experiments in CNTR- and K219T-LMNA lines are shown in the bottom panels. (**B-C**) Percentage of sarcomeric α-actinin+ cells and of live cells. Histograms depict all clones analysed in duplicate.

Following differentiation, we first evaluated the morphological properties of the derived CMs. The morphological analyses revealed significant structural differences between CNTR and *LMNA* (mutated) CMs. The α-sarcomeric actinin immunofluorescence staining in Figure 21 (A and –B panels) shows a severe sarcomeric disorganization in CMs carrying K219T and R190W LaminA/C mutations. Furthermore, patch-clamp recordings in these cells revealed an augmented membrane capacity in *LMNA* mutant CMs, an indication of the increased size of the cells (Fig.18-C). From these experiments we can conclude that the generated models recapitulate the main morphological phenotypes of patients with DCM, α-sarcomeric disorganization and dilatation.

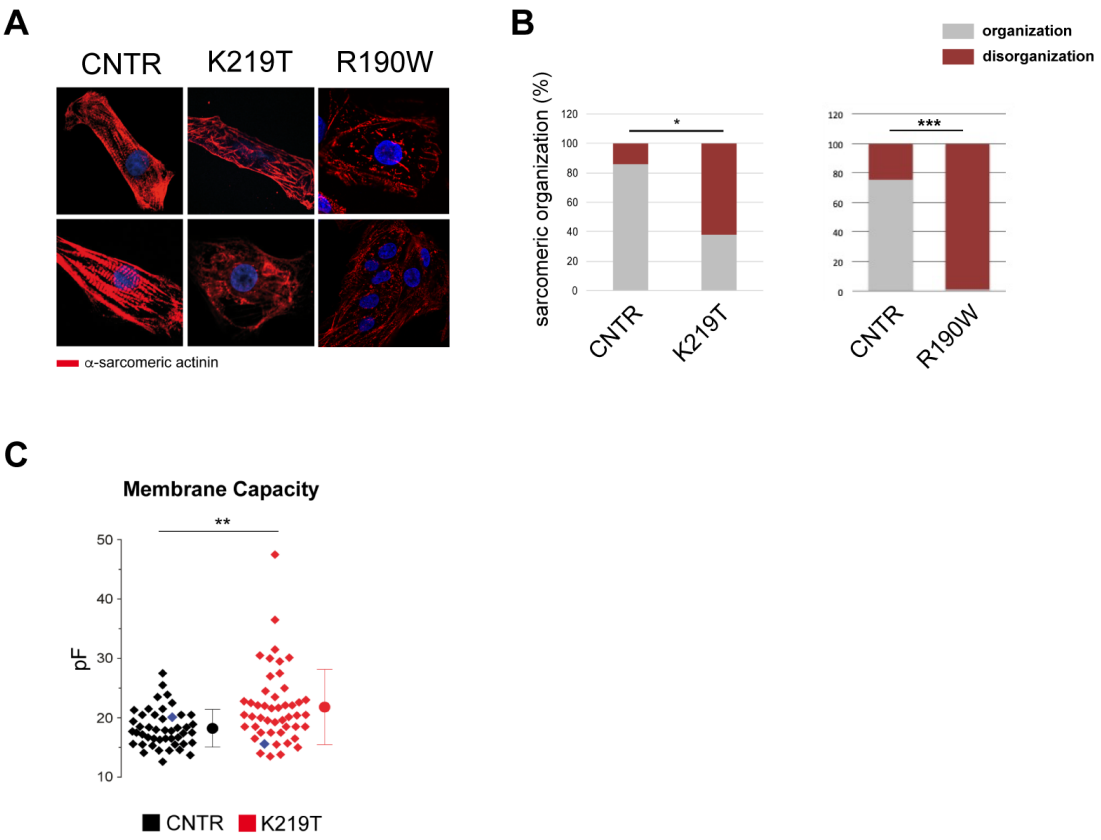

Figure 18. K219T LMNA-CMs recapitulate typical morphological traits of DCM. (A) Alpha sarcomeric actinin staining of CMs differentiated from CNTR, K219T and R190W LMNA-iPSCs revealed sarcomeric abnormalities (fragmented and punctuated staining) in those generated from the mutant lines. Nuclei were stained with DAPI. **(B)** Bar graph of the percentages of cells displaying sarcomeric disorganization in CNTR K219T and R190W cells. CNTR-CMs, n=83, K219T-CMs, n:126, R190W-CMs, n=97. All value are reported as mean ± SD. *p<0.05; ***p<0.0001 (unpaired t-test). **(C)** Patch-clamp recordings of the membrane capacity in CNTR-CMs and K219T-CMs showing a higher mean value in the latter population. CNTR-CMs, n=46, K219T-CMs, n=48. All values are reported as mean ± SD.**p<0.005 (unpaired t-test).

9.3. Transcriptional profiling of LMNA-CMs

In order to globally determine which pathways were altered by Lamin A/C mutations, we performed a global transcriptional profiling of CNTR and K219T LMNA-CMs by total RNA sequencing (Fig.19); the bioinformatics analysis revealed more than 1400 genes differentially modulated between the two experimental conditions. Analysis of the molecular functions and of the disease pathway by IPA (Ingenuity Pathway Analysis) indicated that those mis-regulated genes in *LMNA*-CMs encode proteins with key functions in cardiac conduction, metabolism, and muscle contraction.

Cardiac conduction abnormalities and contractility defects represent major clinical traits of *LMNA*-CMP. Therefore, based on the evidence from the transcriptome analyses, the following studies have been focused on the role of LaminA/C mutations in these two physio-pathological processes, to determine whether LaminA/C affect those functions through controlling the expression of critical genes.

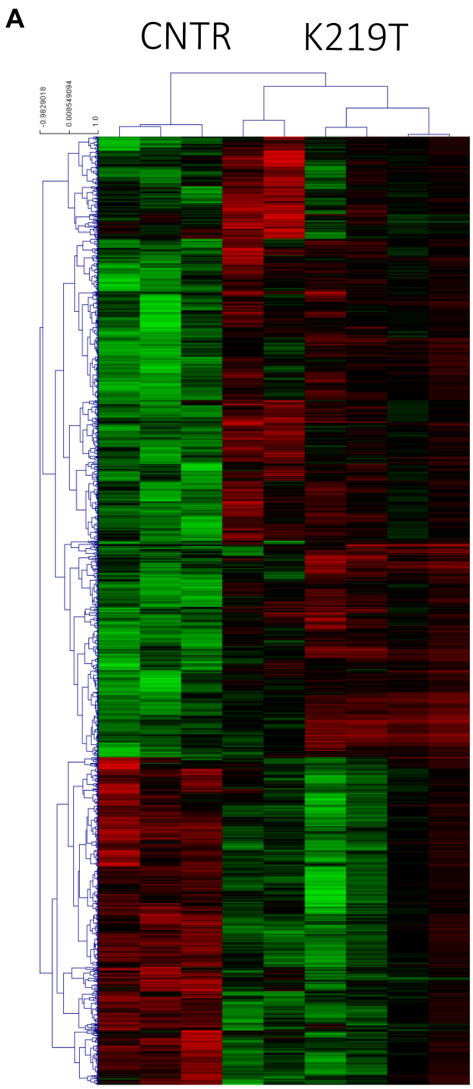

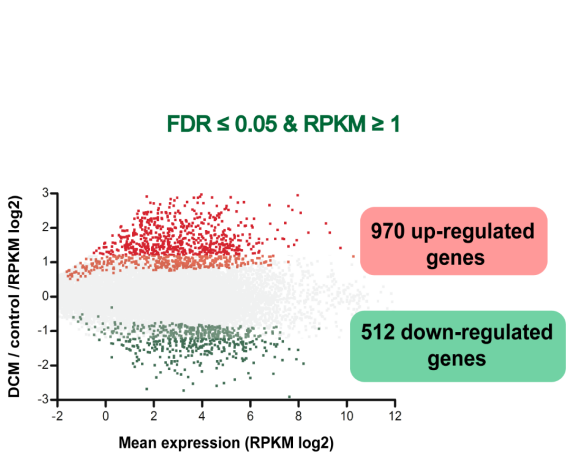

C

Reactome Pathway	FDR	# genes
Extracellular matrix organization	9,99E-14	65
Elastic fibre formation	1,09E-06	16
Retinoid metabolism and transport	1,09E-06	16
Degradation of the extracellular matrix	1,25E-06	23
Metabolism of fat-soluble vitamins	3,72E-06	16

Reactome Pathway	FDR	# genes
Muscle contraction	2,68E-10	31
Cardiac conduction	3,16E-08	19
The citric acid (TCA) cycle and respiratory electron transport	2,28E-06	20
Metabolism	1,54E-05	73
Glucose metabolism	3,79E-04	11

Figure 19. Transcriptional profile of LMNA-CMs. (A) Heatmap of the coding mRNA found differentially modulated in CNTR and K219T LMNA-CMs; (**B)** RPKM (Reads Per Kilobase Million) analysis showing genes differentially modulated: 970 up-regulated and 512 down-regulated in K219T LMNA-CMs samples compared to CNTR. (**C)** Table summarizing the functional pathways relative to the modulated genes, up-regulated in red and down-regulated in green.

9.4. Functional studies:

From action potential characteristics to determination of conduction properties of *LMNA*-CMs

In parallel to the definition of the transcriptome of *LMNA*-CMs, we also performed a comprehensive electrophysiological analysis assessing their main action potential (AP) properties by conventional whole-cell patch-clamp technique. Results from these experiments showed that the functionality of CMs was significantly affected by *LMNA* mutations. As shown in the Figure 23, maximal diastolic potential (MPD), maximal upstroke velocity (dV/dt_{max}) and the related AP properties, such as overshoot and AP amplitude (APA), were significant altered in K219T-CMs. In brief, we found MPD value increased in K219T-CMs (Fig.20-A), as indication of a more depolarized status compared to control samples. Moreover, we observed a significant decrease of dV/dt_{max} (Fig.20-B left panel), indicative of peak sodium current (I_{Na}) during the upstroke (Cohen, Bean et al. 1984; Berecki, Wilders et al. 2010), and the related AP properties, which in turn are representative of cardiomyocyte excitability and proper expression and functionality of $Na_v1.5$.

Based on both, results on altered cardiac conduction from transcriptional analysis and functional studies indicating defects on properties of cardiac excitability, the following studies were centred on deepening the mechanisms underlying those functions identified altered in *LMNA*-CMs and the specific role of LaminA/C defects in these processes.

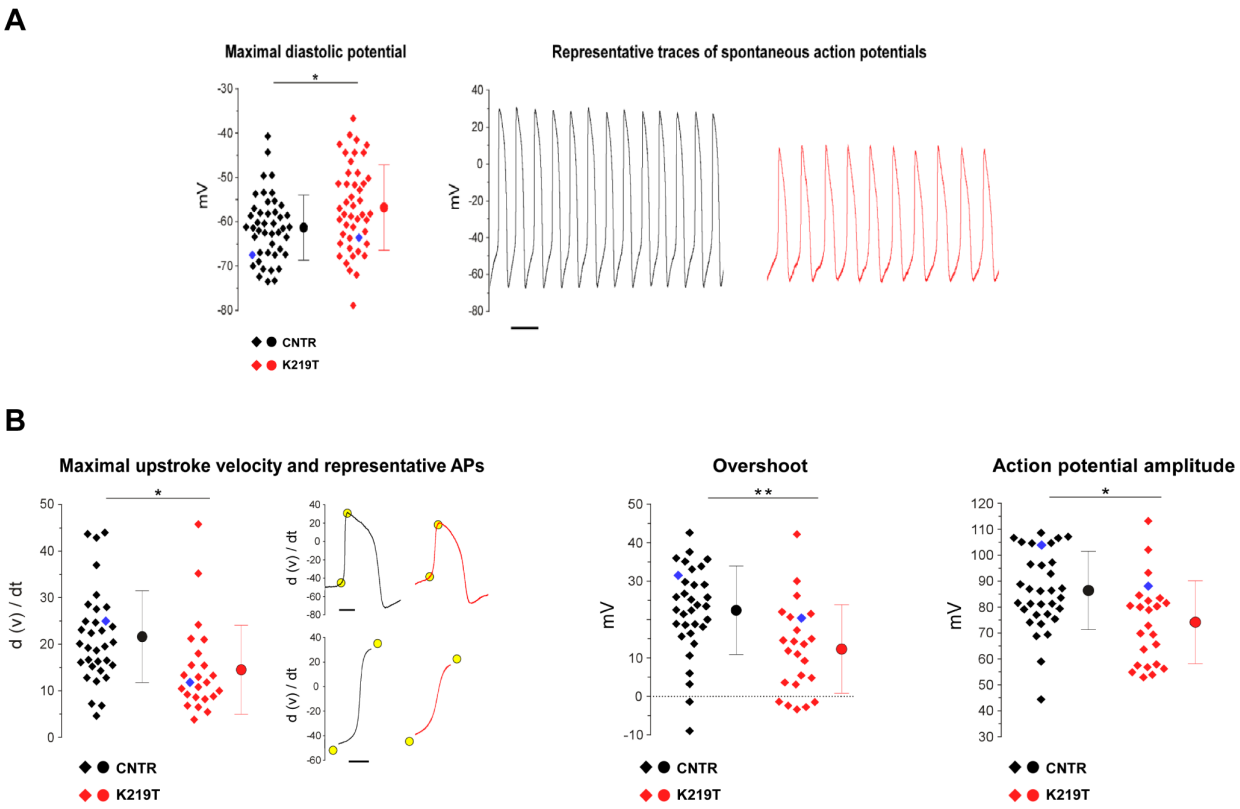

Figure 20. Action potential properties of LMNA-CMs. (**A**) Examples of spontaneous APs recorded in CNTR and LMNA-CMs (right panel; scale bar, 1 sec) and dot plot with maximal diastolic potential (MDP) data (left panel) recorded from CNTR and K219T-CMs, showing a depolarization of K219T cells. CNTR: n=45; K219T=46. (**B**) Dot plots for the main excitability features measured in spontaneously active iPSC-CMs: maximal upstroke velocity (dV/dt_{max}), overshoot and action potential amplitude (APA) are shown. All values are reported as mean ± SD. *p<0.05; **p<0.005 (unpaired t-test). Data are relative to CMs differentiated from 2 lines from each subjects (2 CNTR and 3 K219T-LMNA).

9.4.1. LMNA mutant CMs exhibit reduced sodium current density and defects in propagation of the electrical impulse

With the aim to further dissect the functional phenotype of CMs with *LMNA* mutations and to deepen the mechanisms at the basis of the AP abnormalities previously found in those cells by patch-clamp, we next investigated the effects of the *LMNA* mutations on I_{Na} density in iPSC-derived CMs. Therefore, we measured I_{Na} peak density of fast voltage-dependent sodium channels ($Na_v1.5$) by whole-cell patch clamp, using specific voltage protocols and external ionic solutions and found that the average peak I_{Na} density in K219T-and R190W-CMs was significantly lower than in CNTR cells (Fig. 21), with a

reduction of >40% at the membrane potential of -30 mV (Fig. 21). No significant differences in voltage dependence of activation and inactivation parameters (half-maximal voltage [$V_{1/2}$] and slope factor [k]) were instead detected between wild-type and mutated CMs (Fig. 21-C).

Therefore, an impairment of I_{Na} was observed in K219T- and R190W-CMs, which is in line with the reduction of the dV/dt_{max}, registered in these cells as described above.

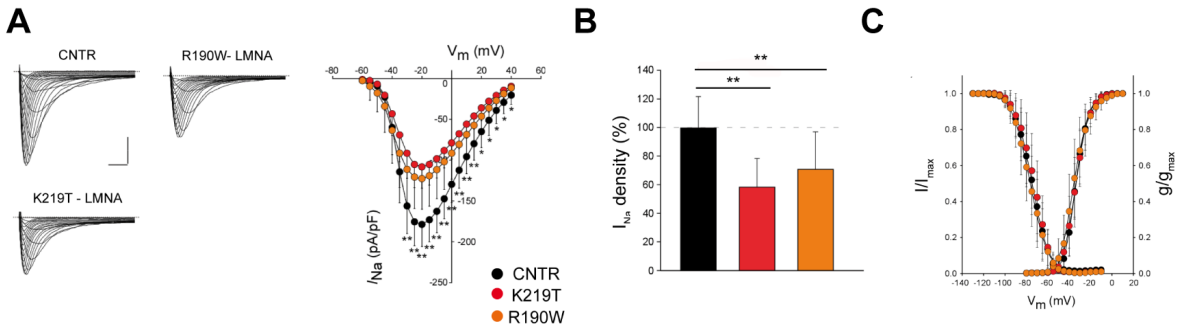

Figure 21. Voltage-gated sodium currents in K219T- and R190W-CMs. (**A**) On the left, representative Na^+ current (I_{Na}) traces recorded in control (top-left), R190W (top-right) and K219T (bottom) –LMNA-CMs (scale bar 2ms, 50pA/pF) The right panel shows I-V curves of average peak sodium current density. Results showed a significant reduction in R190W and K219T-CMs. (CNTR: n=23; R190W: n=18; K219T: n=22); (**B**) I_{Na} density, analysed at -30mV. Data are measured in R190W-CMs (110.93 ± 40.61 pA/pF) and K219T-CMs (91.58±30.69 pA/pF) relative to CNTR-CMs (156.12±33.73 pA/pF) and expressed as a percentage. (**C**) Steady state of activation (CNTR: n=23; R190W: n=18; K219T: n=22) and inactivation (CNTR: n=18; R190W: n=14; K219T: n=17) curves. Data are relative to iPSC-CMs differentiated from 2 independent lines from two CNTR, three K219T and one R190W-LMNA subjects. All values are reported as mean ± SD. *p<0.05;**p<0.005 (unpaired t-test).

I_{Na} and dV/dt_{max} are major players in driving the impulse propagation across the myocardium; we therefore hypothesized that defects at this level may exert an effect on cardiac impulse propagation and measured the propagation velocity of the APs in a confluent multi-cellular setting, which is electrically-coupled iPSC-CMs cultured on 80 µm wide strands (Fig. 22-A). For the analysis, cells were loaded with the voltage-sensitive dye DI-8-

ANEPPS and elicited with electrical stimulation at increasing frequencies. Results showed that CMs carrying K219T mutation failed to respond to increasing electrical stimulation at frequencies of 1Hz and 2Hz (Fig. 22-B). The resulting block (2:1, 3:1 or complete) of the impulse propagation is in agreement with the prolonged absolute refractory period secondary to the reduced sodium currents. Furthermore, K219T-CMs showed a significant decrease of the conduction velocity (CV) (Fig. 22-C), further supporting the notion of an impairment of impulse propagation in presence of the LaminA/C mutation.

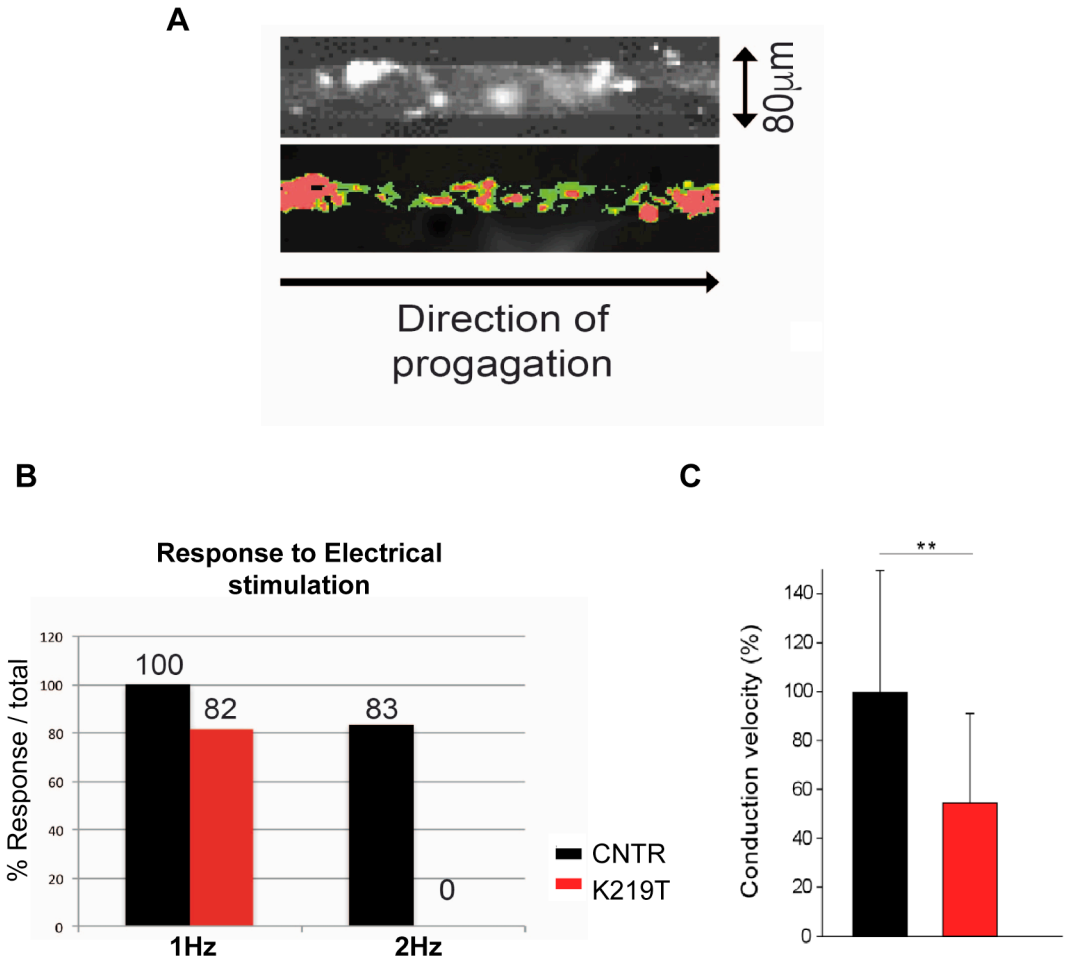

Figure 22. Generation and propagation of optical action potentials in K219T iPSC-CMs. (**A**) Representative images of a monolayer of iPSC-CMs in geometrically-defined strands (80 µm wide, 1-cm long). (**B**) Percentage of propagated APs at 1 and 2 Hz stimulation. (**C**) The bar graphs represent conduction velocity recorded in cell strands consisting of CNTR and K219T-CMs. CNTR: n=47; K219T: n=40. All values are

reported as mean ± SD. **p<0.005 (unpaired t-test). Data are relative to CMs differentiated from 2 independent lines from 2 CNTR and 3 K219T-LMNA subjects.

9.5. Molecular mechanisms of cardiac conduction defects in *LMNA*-CMs

9.5.1. Reduced sodium currents in K219T-CMs are determined by reduced expression of Nav1.5 and its encoding gene *SCN5A*

To deepen the molecular mechanism underlying the reduced sodium currents density in CMs carrying LaminA/C mutations, we first determined whether the cardiac sodium channel $Na_v1.5$ was correctly expressed and localized within the CMs by immunofluorescence. Surprisingly, we found that the expression of the protein was significantly reduced in CMs carrying the K219T-mutation in respect to the control cells (Fig. 23). Western blot analysis confirmed these results and showed a reduced expression of $Na_v1.5$ in the mutant cells.

Next, we investigated whether a diminished transcription of the $Na_v1.5$'s encoding gene, *SCN5A*, may be at the basis of our observations. In fact, among the diverse biological functions attributed to LaminA/C, a role in regulating gene expression has been described (Lund, Oldenburg et al. 2013; van Steensel and Belmont 2017). Moreover, relatively recent studies have indicated a link between LaminA/C defects and altered gene expression in different pathological contexts (Lee, Jiang et al. 2016; Lee, Lau et al. 2017).

Based on these premises, we analysed the relative expression of *SCN5A* in CNTR and *LMNA*-CMs by qRT-PCR. Results from these experiments are shown in the Figure 24 and indicate significantly reduced levels of *SCN5A* in both K219T-and R190W-CMs in respect to the control cells, supporting a role of LaminA/C in regulating its transcription.

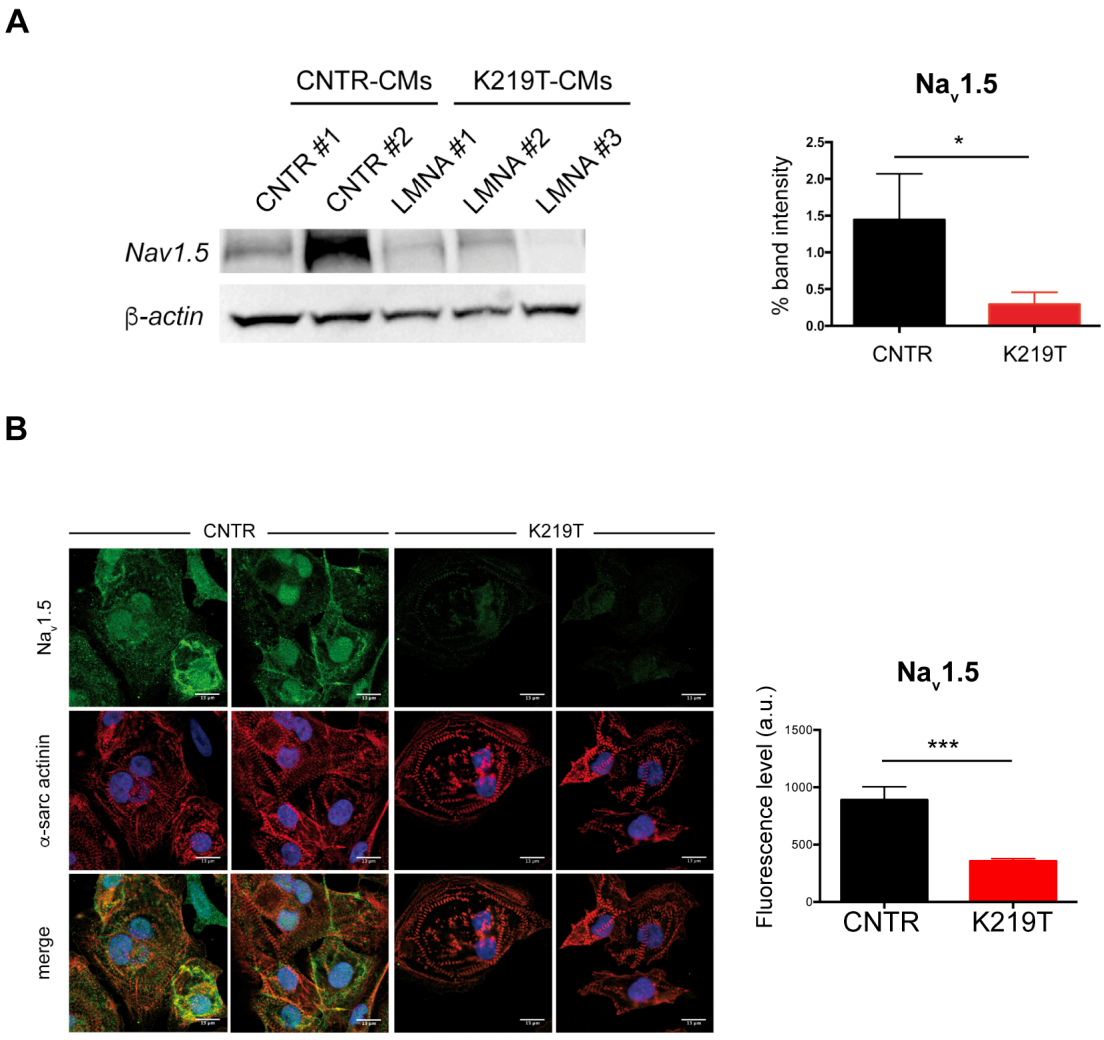

Figure 23. Reduction of Na$_v$1.5 protein in K219T-CMs. (A) Left: Western blot analysis showing reduced level of Na$_v$1.5 channel expression in K219T LMNA-CMs. Data are representative of one cell line per subject. Right: quantification of Na$_v$1.5 band intensity calculated as Na$_v$1.5/β-actin ratio (the diagram represents the mean of three independent experiments). **(B)** Left: Representative immunofluorescence images for Na$_v$1.5 (green) and α-sarcomeric actinin (red) in CNTR- and K219T LMNA-CMs; nuclei are stained with DAPI. (Scale bars: 13 μm). Right: quantification of Na$_v$1.5 fluorescence level calculated using ImageJ software (a.u. arbitrary unit). CNTR: n=10; K219T: n=10. All values are reported as mean ± SD. *p<0.05; ***p<0.01 (unpaired t-test).

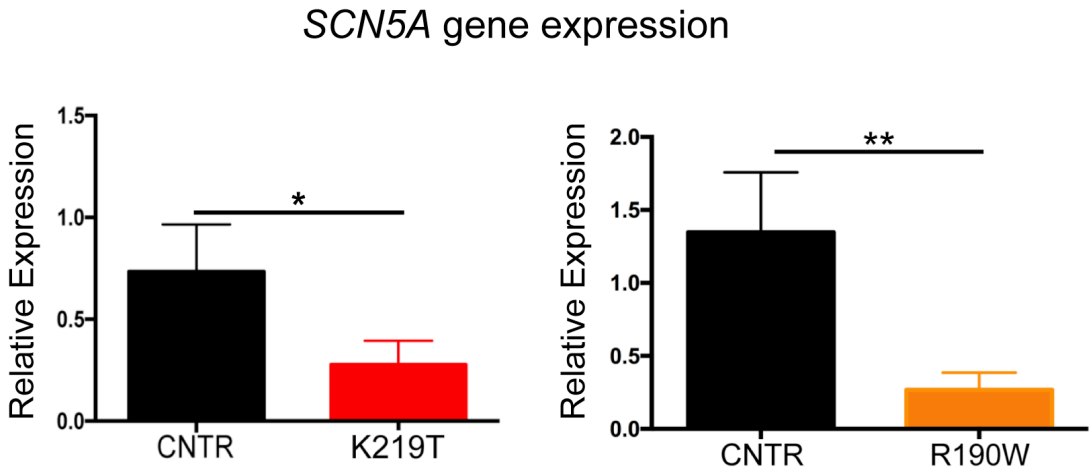

Figure 24. Reduction of SCN5A gene expression in CMs generated from both K219T and R190W LMNA-iPSC CMs. Real-time qPCR showing reduced expression of *SCN5A* gene in CMs generated from K219T LMNA-iPSCs (left) and R190W LMNA-iPSCs (right) compared to those differentiated from CNTR lines. Data are represented relative to CNTR-CMs and normalized to expression of the housekeeping genes *18S* and *HGPRT*. Data are relative to CMs differentiated from 2 independent lines from 2 CNTR, 3 K219T-LMNA and 1 R190W-LMNA. All values are reported as means ± SD. *p<0.05; **p<0.01 (unpaired t-test).

Altogether, the obtained results sustain the hypothesis that a reduction of the expression of *SCN5A* gene driven by LaminA/C mutations is at the basis of the diminished sodium currents density recorded in these cells and may, consequently, lead to an aberrant impulse propagation.

9.5.2. Reduction of *SCN5A* expression in *LMNA*-CMs is directly mediated by LaminA/C through an epigenetic mechanism

The above described results showed that the sodium channel gene, *SCN5A,* is differentially expressed at both mRNA and protein levels in CNTR-CMs and LMNA mutated-CMs (K219T and R190W mutations). To investigate how LaminA/C mutations can affect the expression of this gene, we next assessed the occupancy of its promoter by Chromatin Immunoprecipitation (ChIP) assay.

Figure 25-A shows the results of ChIP against LaminA/C and its binding to the Transcriptional Start Site (TSS) of *SCN5A* and indicates an enrichment of LaminA/C at this genomic locus in K219T-CMs compared to CNTR-CMs. On the contrary, LaminA/C resulted to be equally enriched in both experimental conditions (CNTR and K219T–CMs) at the TSS of *SCN10A, DEFA3* and *DEFA4* genes (Fig.25-A), which were evaluated as known genomic targets of LaminA/C. No enrichment of the protein is instead detectable at the TSS of the *JUN* gene, used as control of the specificity of the antibody, in both experimental samples. These findings confirmed the specificity of LaminA/C binding to *SCN5A* locus in K219T-CMs and strengthened our hypothesis that the mutated protein is directly involved in regulating the expression of the gene. To further characterize the mechanism behind *SCN5A* regulation, we performed ChIP analyses of two histone markers indicative of transcriptional repression – tri-methylated lysine 27 on histone 3 (H3K27me3) and tri-methylated lysine 9 on histone 3 (H3K9me3), and of one marker of transcriptional activation – tri-methylated lysine 4 on histone 3 (H3K4me3). Results in the Figure 25 (-B and –C) showed an enrichment of the two repressive marks at the TSS of the *SCN5A* gene in K219T-CMs; in contrast, H3K4me3 was enriched in CNTR-CMs (Fig. 25-D). Again, these findings support the hypothesis that diminished sodium current density in mutated CMs is due to reduction of *SCN5A* expression, which is epigenetically modulated.

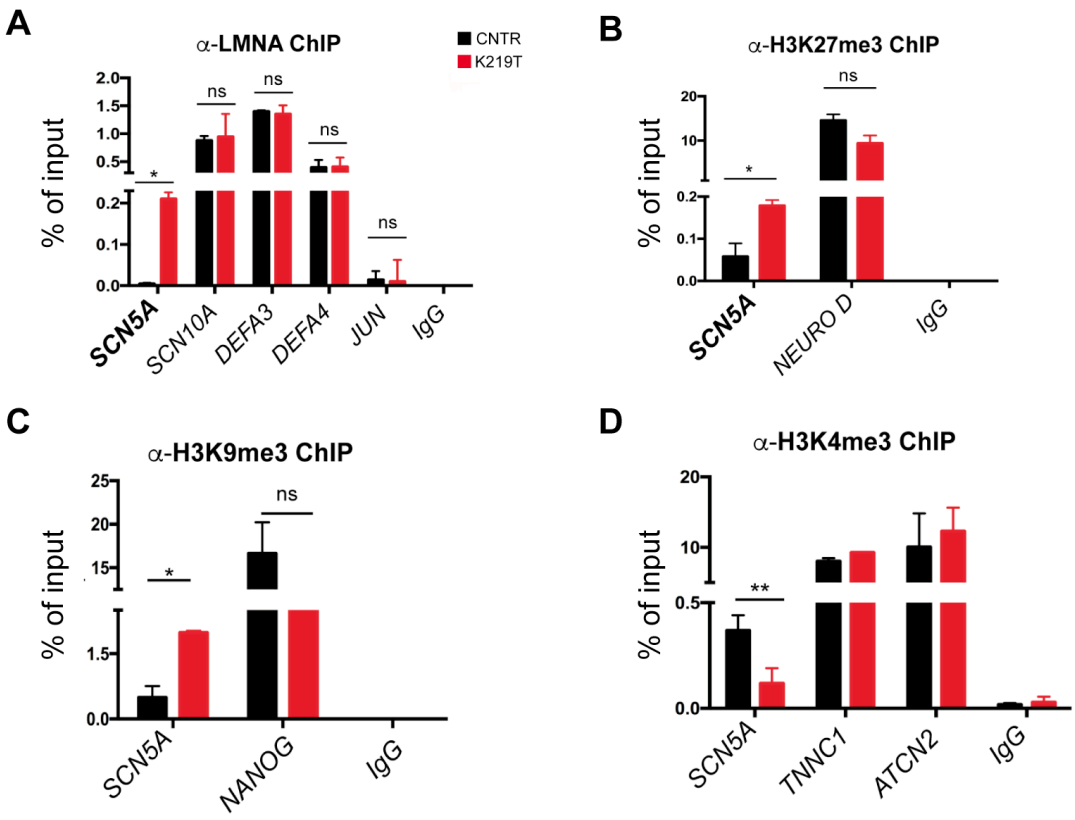

Figure 25. Lamin A/C mutation induces *SCN5A* repression through epigenetic regulation at its promoter. (A) ChIP for Lamin A/C, indicating increased binding of LaminA/C to the promoter region of the *SCN5A* gene in K219T-CMs. No enrichment was detectable for *JUN*, used as a negative control region for the ChIP experiment. *SCN10A*, *DEFA3* and *DEFA4* genes were used as positive control regions for the ChIP experiments. **(B)** ChIP for the histone modification H3K27me3, showing an enrichment of the repressive histone marker at the *SCN5A* gene promoter in K219T-CMs, supporting the reduced expression of the gene detected in these cells. *NEURO D* was used as positive control region for the antibody. **(C)** ChIP for H3K9me3, showing enrichment of this repressive marker at the promoter region of the *SCN5A* gene in K219T-CMs. The marker was equally enriched on the *NANOG* promoter region of CNTR and K219T-CMs, used as control. **(D)** ChIP for H3K4me3, showing enrichment of this active marker at the promoter region of the *SCN5A* gene in CNTR-CMs, and thus supporting active transcription of this gene in control cells. Analysis of deposition of H3K4me3 marker at *TNNC1* and *ACTN2* loci served as a control for the antibody. Data are presented as a percentage of input chromatin precipitated and relative to 2 independent iPSC-clones from each subject. All values are reported as means ± SD. ns: not significant; *p<0.05; **p<0.01 (unpaired t-test).

To further corroborate the specific action of Lamin A/C on the regulation of *SCN5A* among the other important genes of the cardiac conduction pathway, we also determined the expression levels of those encoding proteins that play key roles in cardiac conduction (i.e. *CX40*, *CX43*, *TBX3*, *TBX5*) and assessed Lamin A/C binding at their promoters. Results from

these experiments showed no significant changes in the expression of those genes between CNTR and K219T-CMs and no differences in Lamin A/C enrichment at their promoters (Fig. 26) further confirming *SCN5A* as main target of Lamin A/C in relation to the observed phenotype.

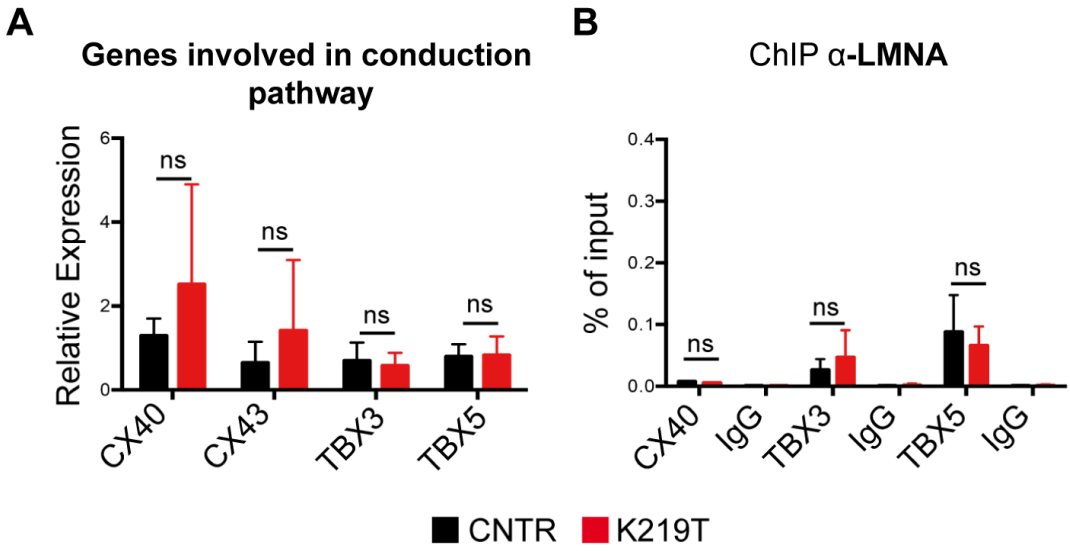

Figure 26. Epigenetic modulation of genes involved in cardiac conduction. (A) Realtime qPCR for genes encoding proteins with a key role in cardiac conduction, namely *CX40*, *CX43*, *TBX3* and *TBX5*, showing no significant differences in their expression levels between CNTR-CMs and K219T-CMs. **(B)** ChIP for LaminA/C followed by real-time qPCR of the immunoprecipitated DNA, assessing the binding of LaminA/C at the promoter region of the genes analysed in A. No significant enrichment was detectable at any of the analysed genes. *CX43* has not been included in the graph since values from real-time PCR were undetectable in both conditions. Data are presented as a percentage of input chromatin precipitated and relative to 2 independent iPSC-clones from each subject. All values are reported as means ± SD. ns: not significant.

Nuclear lamins are also implicated in tethering heterochromatin to the nuclear lamina (Deniaud and Bickmore 2009; Solovei, Wang et al. 2013); these interactions occur through large Lamin-Associated Domains (LADs) in chromatin and are predominantly associated with transcriptional silencing (Guelen, Pagie et al. 2008; Luperchio, Wong et al. 2014). LADs are mostly cell-specific and may be distinguished into constitutive (cLADs) and

variable (vLADs). The latter correspond to LAD borders and have been shown to be marked by H3K27me3 and to dynamically shift to and from the nuclear periphery during development, determining distinct gene expression outcomes (Yanez-Cuna and van Steensel 2017).

Since *SCN5A* has been reported to locate in close proximity to *SCN10A* and *SCN11A*, both mapping in a LAD (Lund, Oldenburg et al. 2013), we next determine whether chromatin remodelling (re-localization of the LADs) is occurring in presence of *LMNA* mutations and analyse the LaminA/C binding at this genomic locus during the differentiation of iPSC into CMs. We found that, in CNTR-CMs, LaminA/C interact with the *SCN5A* promoter at early stages of cardiac differentiation, but that binding was lost from day 12. In contrast, in K219T-CMs such binding was maintained throughout differentiation (Fig.27-A) and, later, in terminally differentiated CMs. This finding supports the hypothesis that *SCN5A* is included in a differentiation-regulated LAD, and is consistent with ChIP-seq data previously reported in other cell types (Lund, Oldenburg et al. 2013) and with the cardiac-specific expression of the *SCN5A* gene.

In addition, to visualize the nuclear localization of *SCN5A* gene, we performed 3D-DNA immuno-FISH (Fluorescence In Situ Hybridization) as previously described (Reddy, Zullo et al. 2008). Figure 27-B is illustrates the methodology employed to build the 3D distance map with ImageJ software and to assign a position to the gene of interest in the analysed iPSC-CMs nuclei. Results from this analysis showed a preferential positioning of *SCN5A* gene at the nuclear periphery in K219T-CMs when compared to CNTR cells (Fig. 27-C), further supporting the notion that LaminA/C regulates *SCN5A* gene expression and that chromatin remodelling (re-localization of the LADs) may occur in the presence of the *LMNA* mutations.

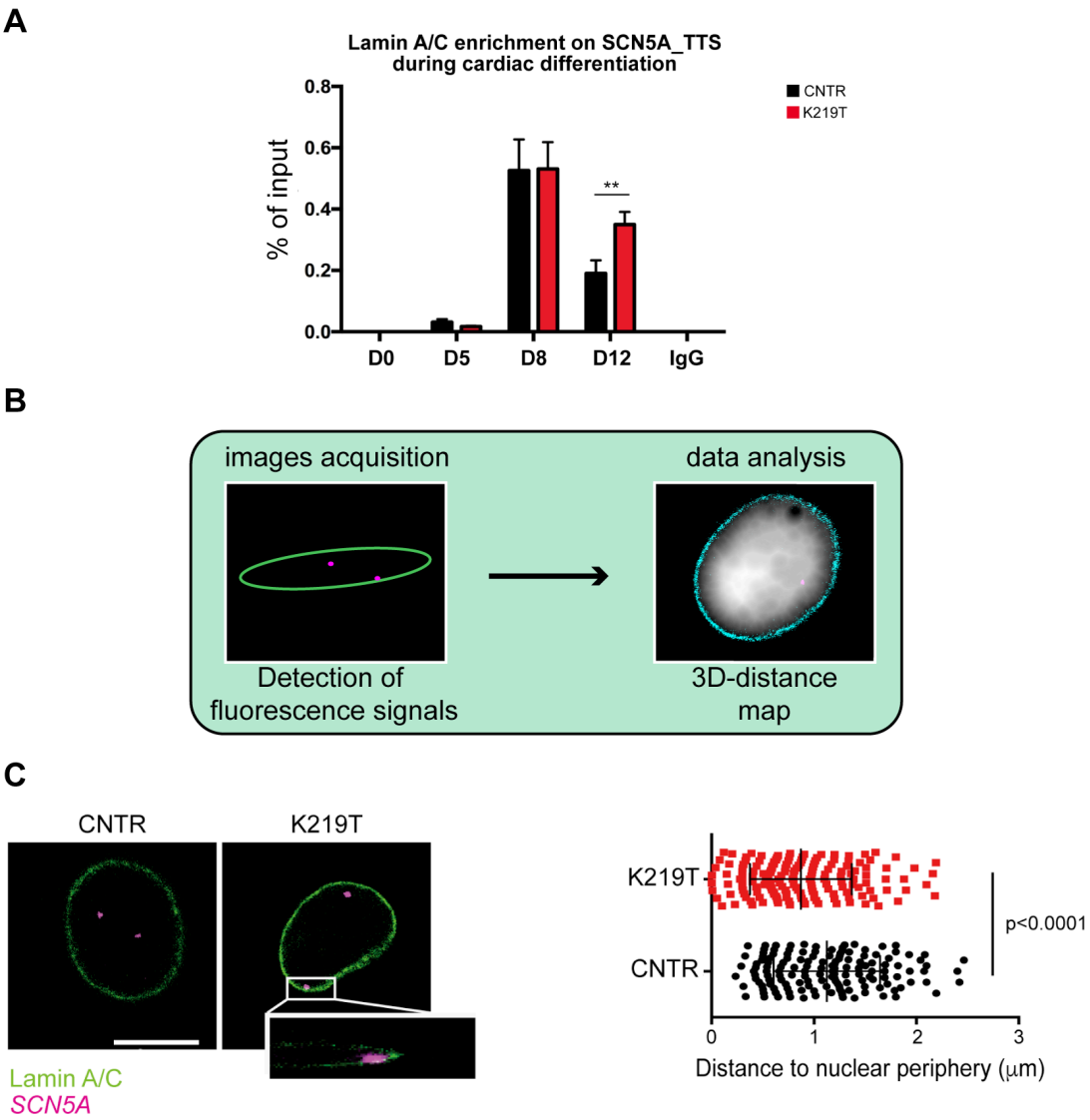

Figure 27. Epigenetic modulation of SCN5A promoter during cardiac differentiation and analysis of the nuclear positioning of SCN5A locus. (A) ChIP against Lamin A/C, showing the dynamics of Lamin A/C enrichment at the TSS of the *SCN5A* gene during cardiac differentiation (from days 0 to 12). For this analysis, two-way Anova was used as the statistics test. Data are presented as a percentage of input chromatin precipitated and relative to 2 independent iPSC clones from each subject. All values are reported as means ± SD, if not differently specified. **p<0.01, ns: not significant. **(B)** Strategy used for 3D-FISH data analysis. Left: images were acquired using confocal microscope. The green circle indicates the Lamin A/C, while the magenta spots the genomic region relative to the *SCN5A* gene. The acquired z-stacks images were analysed using ImageJ software. Right: Using 3D-distance map function, on DAPI channel, we calculated the distance of *SCN5A* spots from nuclear periphery (cyan), in each CM nucleus; **(C)** 3D-FISH experiment detecting Lamin A/C (green) and the *SCN5A* gene (magenta) with an antibody and a DNA probe respectively. Left: representative images of nuclei from CNTR and K219T-CM preparations (Scale bar: 9 µm). Magnified box shows the colocalization of the *SCN5A* probe at the nuclear lamina. Right: Analysis of the distance from the nuclear lamina, showing preferential localization of the *SCN5A* probe (magenta) at the nuclear periphery in

K219T-CMs vs CNTR. Quantification was carried out using a specific plug-in of the ImageJ software (CNTR: n=72 cells; K219T: n=82 cells; $p<0.0001$ unpaired t-test).

To corroborate the obtained results, we also investigated the role of LaminA/C *in vivo* on heart tissue sections from the same patients carrying the K219T mutation (Fig. 28-A). Through molecular studies targeting both, the $Na_v1.5$ protein and its encoding gene *SCN5A*, we confirmed a reduced expression of $Na_v1.5$ sodium channel in heart tissue sections from patients carrying the K219T mutation in respect to control hearts (Fig. 28-B-C); furthermore pathology tissue chromatin immunoprecipitation (PAT-ChIP) experiments showed an increased binding of LaminA/C at the TSS of *SCN5A* in heart sections from K219T patients compared to controls (Fig. 28-D). Overall these results further strengthen the hypothesis that the reduction of sodium currents is dependent upon diminished expression of the *SCN5A* gene, also in adult human cardiomyocytes.

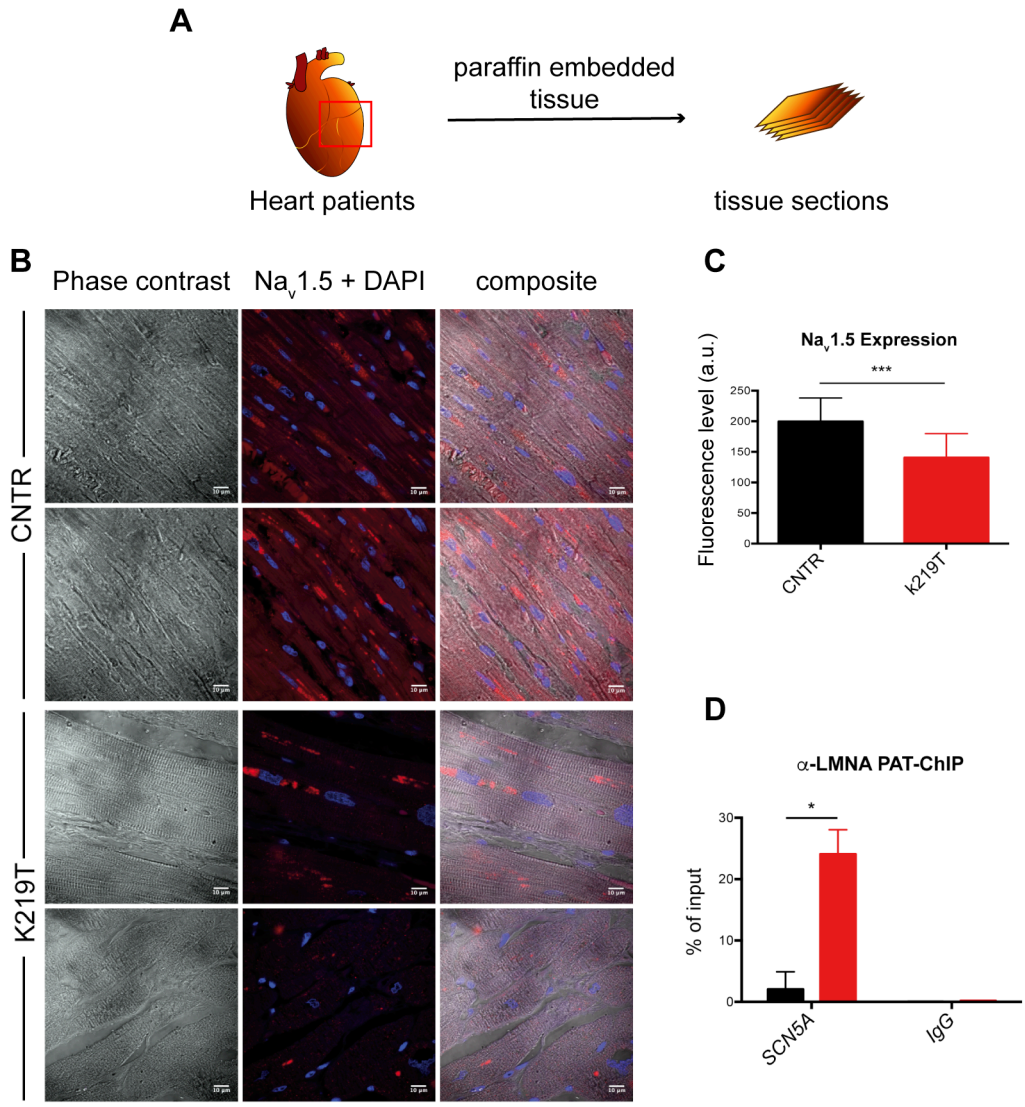

Figure 28. Analysis of heart tissue sections. A) Graphic representation of the starting samples used to perform cardiac tissue investigations. **(B)** Immunostaining of paraffin-embedded heart sections from patients carrying the K219T mutation on LaminA/C (bottom panels) and from control subjects (top panels) targeting the $Na_v1.5$ sodium channel (red); nuclei were stained with DAPI. **(C)** Histogram showing the quantification of the red fluorescent signal, corresponding to the $Na_v1.5$ protein, confirming its reduced expression also in K219T-LMNA patient hearts (a.u. arbitrary unit). **(D)** PAT-ChIP analysis of heart sections from patients carrying the K219T mutation on *LMNA* (red bar) and from control subjects (black bar), showing increased binding of LaminA/C at the *SCN5A* gene promoter region in K219T-CMs. Chromatin was immunoprecipitated with an antibody against LaminA/C and the resulting DNA was analysed by real-time qPCR and presented as a percentage of input chromatin precipitated for the indicated region. All values are reported as means ± SD.*$p<0.05$; ***$p<0.0001$ (unpaired t-test). Data are relative to 2 independent iPSC-clones from each subject.

9.5.3. LaminA/C cooperates with PRC2 complex in regulating *SCN5A* gene transcription

Interaction between the LaminA/C and chromatin is widely recognized and may occur directly or through chromatin binding factors (Wilson and Foisner 2010). The DNA Adenine Methylation-based Identification (Dam-ID) first, and ChIP-sequencing experiments (ChIP-seq) afterwards, have allowed the discovery and the investigation of the LADs regions (Guelen, Pagie et al. 2008). However, how LAD regions are regulated in disease and mechanisms by which they influence gene expression remains poorly understood. According with published studies, LaminA/C epigenetic signature is associated with H3K27me3 profile (Harr, Luperchio et al. 2015; van Steensel and Belmont 2017), in particular at the vLADs. This epigenetic modification is specifically catalysed by Polycomb Repressive Complex 2 (PRC2). Cesarini E. and colleagues recently described a tissue-specific cross-talk between LaminA/C and PRC2 in regulating gene transcription (Cesarini, Mozzetta et al. 2015), and showed that this is involved in controlling the expression of a large number of genes during differentiation of muscle cells. Based on these premises and on our results showing an enrichment of H3K27me3 at the *SCN5A* promoter, we next determined whether the *SCN5A* expression could be modulated by a cooperation between PRC2 and LaminA/C. We thus evaluated the binding of Suz12, a subunit of PRC2, to the *SCN5A* promoter by ChIP and found an increased binding of this protein in K219T-CMs (Fig. 29-A). This is indicative of a potential interaction between LaminA/C and PRC2 in modulating transcription in CMs. To test this, we performed immunoprecipitation (IP) experiments against LaminA/C in CNTR and K219T iPSC-CMs to assess the direct interaction with PRC2. Results showed a higher amount of EZH2 (Enhancer of zeste homolog 2, the catalytic subunit of PRC2) bound to LaminA/C in mutant CMs compared to the controls, indicating a higher binding affinity of mutant LaminA/C to PRC2 (Fig 29-B). This finding was confirmed also on undifferentiated iPSCs following lentiviral-mediated overexpression of either WT- or K219T-Lamin A/C, in which IP experiments showed an increased amount of Ezh2 bound to

mutant LaminA/C with respect to the wild-type protein (Fig. 29-C). These findings support the hypothesis that LaminA/C and PRC2 interact with higher affinity in the presence of the mutation.

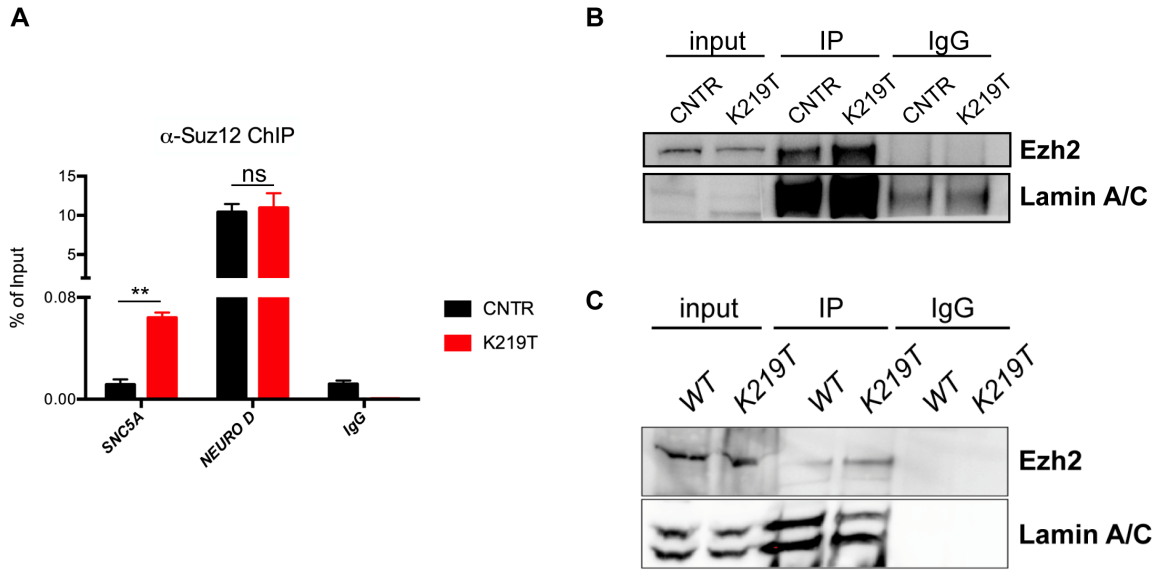

Figure 29. LaminA/C-PRC2 interplay in the regulation of *SCN5A* transcription. (A) ChIP against Suz12 (a PcG protein of the PRC2 complex), showing an enrichment of the protein at the *SCN5A* gene promoter region in K219T-CMs. No significant differences were detectable at the *NEURO D* promoter, used as positive control for the antibody. Data are presented as a percentage of input chromatin precipitated and are relative to 2 independent iPSC lines from each subject. **(B-C)** Western blot analysis of co-immunoprecipitation (co-IP) targeting LaminA/C and the PRC2 subunit Ezh2 conducted on CNTR and K219T-CMs **(B)** and on control iPSCs transduced with lentiviral vectors carrying either GFP-tagged WT- or K219T-Lamin A/C **(C)**. In both experiments, there is a higher binding affinity of mutant K219T-LaminA/C for Ezh2. Nuclear extracts were immunoprecipitated with LaminA/C antibody, and inputs immunoblotted and hybridized with Ezh2 antibody. An unrelated IgG antibody was used as negative control. All values are reported as means ± SD.**p<0.01; ns: not significant (unpaired t-test).

Next, we also evaluated the expression of the two proteins by Super Resolution Microscopy; results from these experiments confirmed the previous Co-IP studies and showed an increased co-localization of the two proteins in K219T-CMs (Fig. 30).

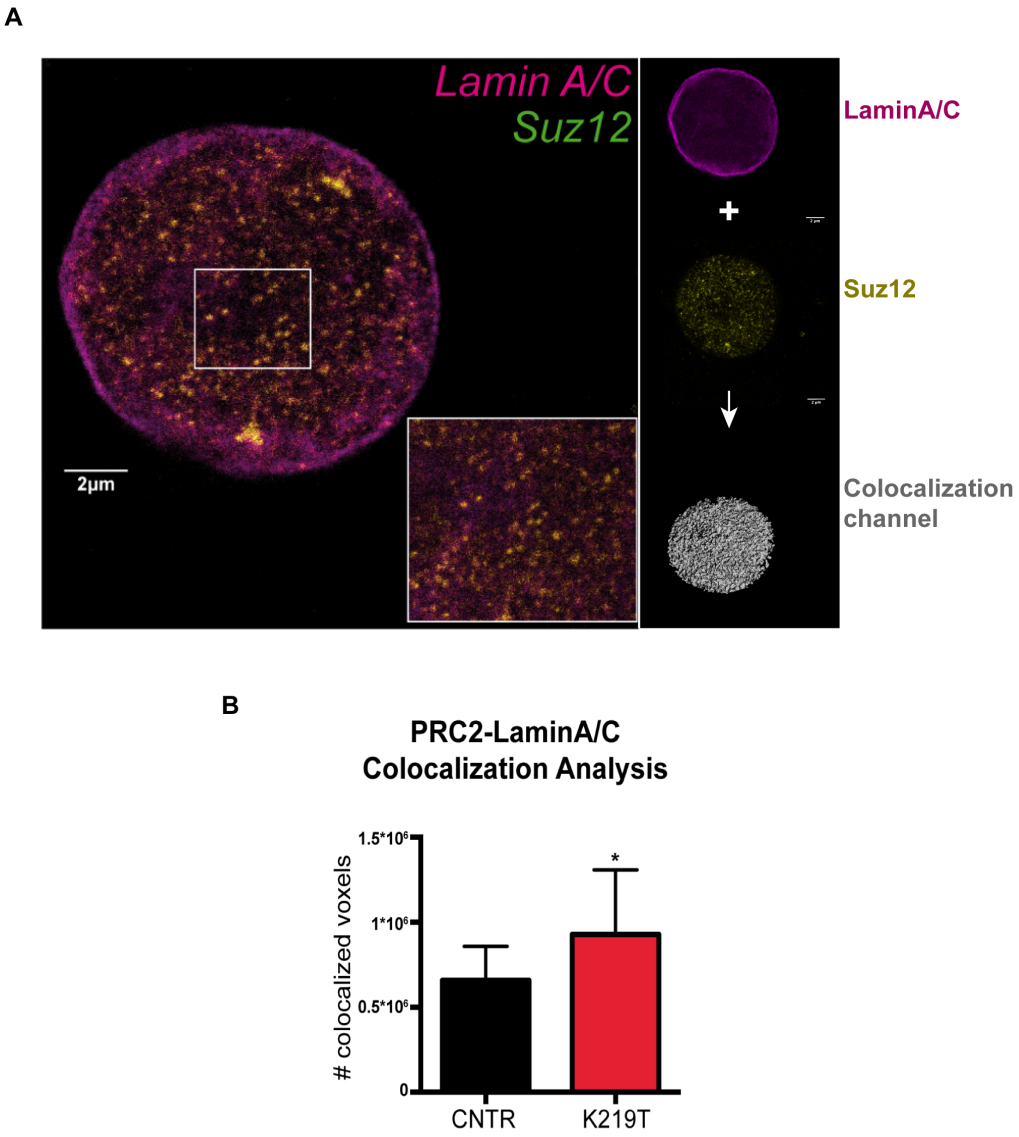

Figure 30. 3D-STED super-resolution microscopy for LaminA/C and Suz12. (A) 3D-STED super-resolution microscopy for LaminA/C and Suz12. On the left, a representative image of a nucleus stained for the two proteins. The magnified box shows the co-localization of the two proteins (visible as yellow spots). Panel on the right show the strategy used to analyse the number of protein colocalization voxels, using the "colocalization channel building" function of Imaris software. **(B)** The graph shows the quantification of the voxels of colocalization of the two proteins: interaction was higher in K219T-CMs vs CNTR-CMs (n=16 cells per condition). All values are reported as means ± SD.*$p<0.05$ (unpaired t-test).

In addition, analysis of the distribution of PRC2 (alone or bound to LaminA/C) showed substantial differences in the global localization-profiles in CNTR and K219T-CMs, suggesting a different dynamics of the proteins in the two conditions (Fig.31). In detail, we found a proportion of the PRC2-LaminA/C complex in closer proximity to the nuclear periphery in K219T-CMs compared to CNTR cells (Fig 31-A-B). This finding fits well with results from 3D-FISH experiments, which locate the *SCN5A* locus preferentially at the nuclear periphery in mutant CMs, and sustains the notion that PRC2 and LaminA/C cooperate to regulate *SCN5A* transcription by simultaneously binding to its promoter at the nuclear periphery. Of note, we also found that a subpopulation of the complex was significantly relocated towards the nuclear interior in K219T-CMs (Fig. 31-B and C), further supporting the emerging view that global rearrangement of the two proteins occurs in the presence of *LMNA* mutations and that this altered dynamics is likely to affect global transcription.

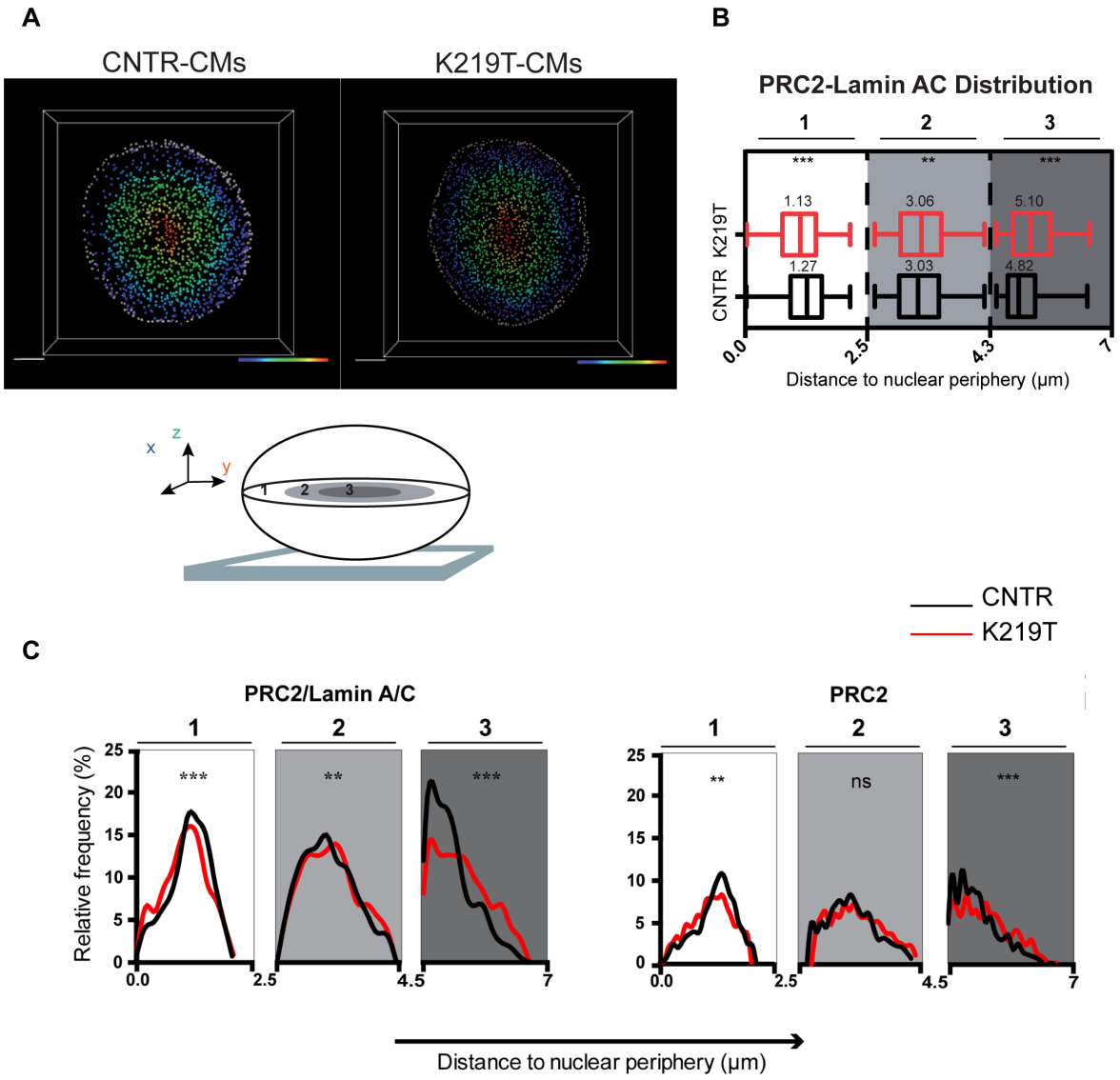

Figure 31. Assessment of PRC2-LaminA/C complex distribution into iPSC-CMs nucleus. (A) Strategy to determine the distance of PRC2-LaminA/C complex from the nuclear periphery. For this analysis, 3D-STED microscopy colocalization channel acquisitions (data from Fig. 3.1.3.6) were used and the "distance transformation" function of Imaris software was applied to z-stack images. Top: representative images of CNTR and K219T-CMs nuclei (scale bar: 2µm). Grey spots indicate LaminA/C fluorescence, selected as the outside ring and serving as the "nuclear edge"; the distance transformation function was run on the LaminA/C channel, and the distances of the PRC2/LaminA/C colocalization calculated. The coloured bar indicates the relative position of the spots to the nuclear edge: the farthest positions are in red and the closest ones in violet. Bottom: strategy used for data representation. Distances were scored in three zones, designated as 1, periphery (from 0 to 2.15 µm, indicated in white); 2, middle (from 2.15µm to 4.3µm, indicated in light grey); and 3, central zone (from 4.3 µm to 6.45 µm, indicated in dark grey). As above, the distance of every single colocalization spot was calculated from the "nuclear edge", identified as a ring of spots of LaminA/C. **(B)** Distribution profile of PRC2-Lamin A/C colocalization in nuclei of CNTR and K219T-CMs. The box plot shows the distribution of PRC2/Lamin A/C complex within the nucleus in the three selected zones. Values are median ± SD of 5 cells per conditions (***p<0.0001; **p<0.01, two-way ANOVA). **(C)** Distribution profiles of PRC2-LaminA/C complex (left) and PRC2 (right). Data show significantly different dynamics of the two proteins in CNTR (black line) and K219T-CMs (red line), with a subpopulation of the PRC2/LaminA/C

complex in K219T-CMs (top) localized closer to the nuclear periphery (zone 1) than in CNTR-CMs, and another subpopulation relocated towards the nuclear interior (zone 3). Distribution relative to PRC2 itself shows profiles similar to those obtained from the colocalization signals above. The distances to the nuclear periphery were calculated relative to the "nuclear edge", identified as a ring of spots of LaminA/C, and represented as frequency distribution profiles using cubic spline of histogram with 0.2 μm Bin. Relative distributions were evaluated in three selected zones: 1, periphery (white); 2, middle (light grey); and 3, central (dark grey). Values are median ± SD of 5 cells per condition (***$p<0.0001$; **$p<0.01$, two-way ANOVA).

9.5.4. K219T LaminA/C overexpression in CMs from control ES cells recapitulates functional and molecular characteristics of parental K219T-CMs

To further prove that the reduction of Na^+ current density and the respective downregulation of the *SCN5A* gene are caused by the K219T LaminA/C mutation, we performed a series of gain of function studies in CMs derived from the RUES2 human ES cell line by overexpressing the mutant K219T-LaminA/C.

We first generated a C-terminal tagged EGFP (enhanced green fluorescent protein)-fusion lentiviral construct expressing LaminA/C carrying the K219T mutation (LaminA/C-EGFP); the same construct expressing the wild type LaminA/C and a lentiviral vector carrying the empty GFP cassette were used as controls (Fig. 32-A). Then, to mimic the heterozygous disease condition, RUES-CMs were transduced at day 6 of differentiation, stage at which LaminA/C begins to be expressed. Analyses by patch clamp showed a reduction of the peak Na^+ current density in cells expressing the mutation, positive for GFP expression (at -30mV holding potential, 29.8% decrease vs CNTR-CMs indicated as GFP^{neg}; Fig. 32-B-D). No changes of the voltage dependence of activation and inactivation parameters (half-maximal voltage [V1/2] and slope factor [k]) between the conditions (Fig. 32-C). Instead, overexpression of either the empty GFP vector or the vector encoding wild-type LaminA/C (WT LaminA/C-GFP) did not produce any effect on Na^+ current density in

RUES2-CMs (Fig. 32-B-C-D), providing an additional demonstration that the observed phenotype is causally linked to the K219T LaminA/C mutation.

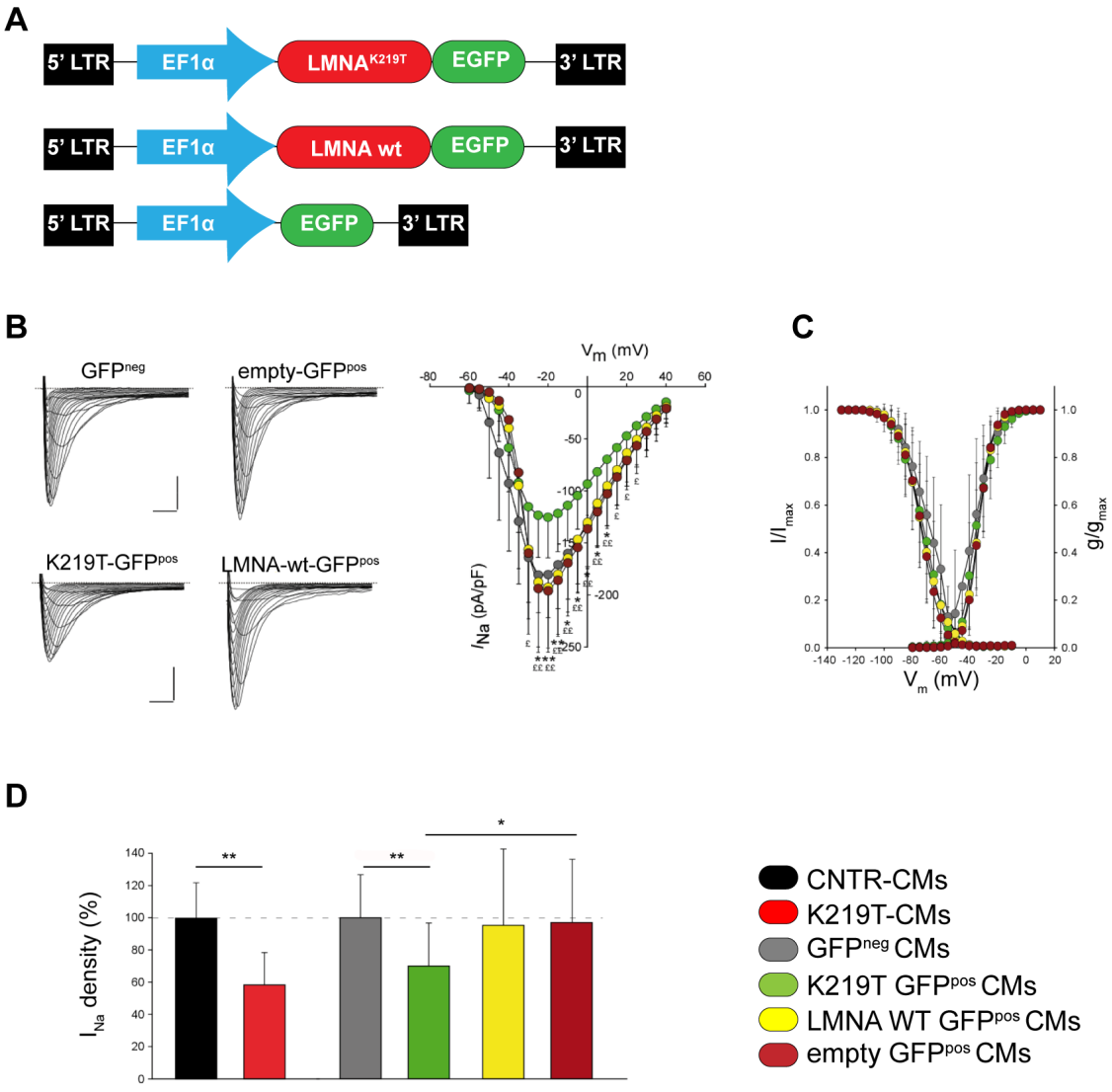

Figure 32. Overexpression of K219T-LMNA in the RUES ESC lines recapitulates the phenotype of parental K219T-CMs. (A) Lentiviral vectors expressing the C-terminal GFP-tagged K219T-LaminA/C, wild type LaminA/C and empty vector, used for the overexpression experiments. **(B)** Left panel: examples of Na^+ current traces recorded in GFP^{neg} and empty-GFP^{pos} CMs (top); K219T-GFP^{pos} and *LMNA*-WT-GFP^{pos} CMs (bottom), (Scale bar, 2ms, 50pA/pF). Right panel: I-V curves constructed from average peak sodium current density as a function of voltage command measured in the four conditions described above (GFP^{neg}: n=14; K219T-GFP^{pos}: n=21; empty -GFP^{pos}: n=15; *LMNA*-WT-GFP^{pos}: n=14) showing significant sodium current reductions in K219T-GFP^{pos} cells, while there were no changes compared to control cells (GFP^{neg}) induced by overexpression of either the empty-GFP vector or the one expressing wild-type LaminA/C. All values are reported as means ± SD. *p <0.05; **p <0.005 and $^{£}$p <0.05; $^{££}$p <0.005 (unpaired t-test). **(C)** Voltage dependences: steady state activation (GFP^{neg}: n=14; K219T-GFP^{pos}: n=21; empty-GFP^{pos}: n=15; LMNA-WT-GFP^{pos}: n=14)/inactivation (GFP^{neg}: n=11; K219T-GFP^{pos}: n=17; empty-GFP^{pos}: n=12; *LMNA*-WT-GFP^{pos}: n=12) curves. (**D**) Na^+ current density, measured at -30 mV, in K219T-CMs (91.58 ± 30.69 pA/pF) relative to CNTR-CMs (156.12 ± 33.73 pA/pF) and K219T-GFP^{pos} (115.20 ± 43.35 pA/pF), *LMNA*-WT-GFP^{pos} CMs

(156.22 ± 81.41 pA/pF) and empty-GFP^{pos} CMs (159.76 ± 63.31 pA/pF) relative to GFP^{neg} CMs (164.02 ± 43.18 pA/pF) all expressed as a percentage. Values for K219T- (red bar) and CNTR- (black bar) CMs are reported from Figure 21 as references for evaluating the relative effect in the analysed overexpression conditions. All values are reported as means ± SD. *p <0.05; **p <0.005 (unpaired t-test).

Functional data were also confirmed at the molecular level, by assessment of the expression of *SCN5A* gene by RT-PCR after cell sorting: the results showed levels of expression significantly lower in RUES-CMs overexpressing the mutation (GFP^{pos}) in respect to the control GFP^{neg} cells (Fig. 33-A-B).

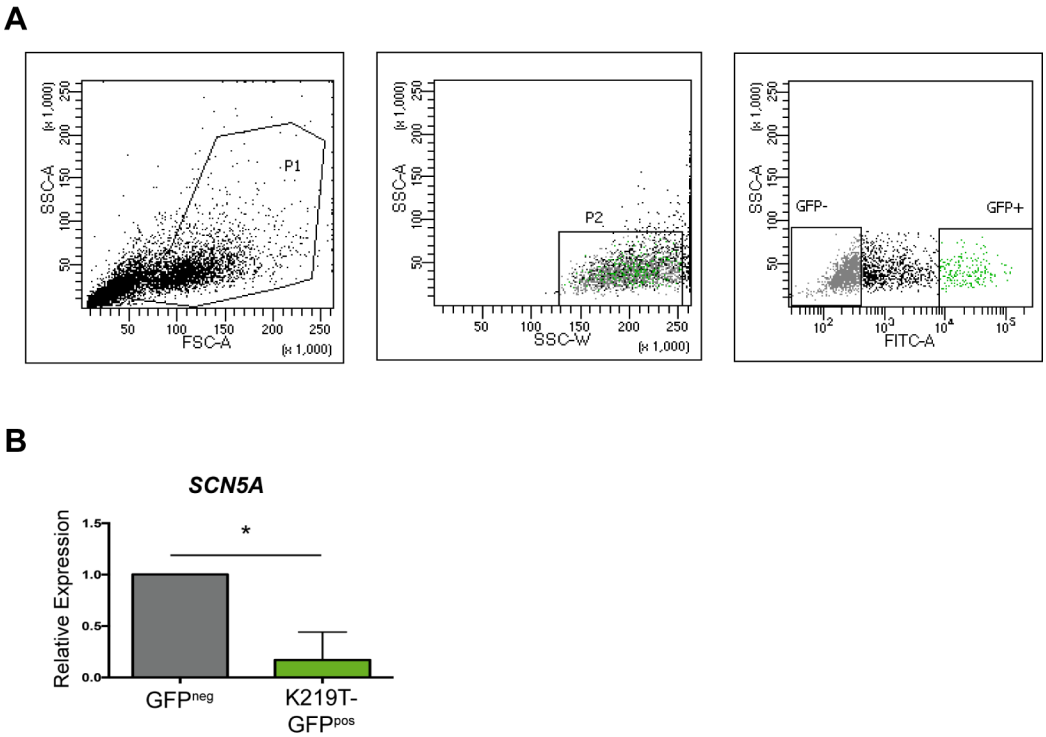

Figure 33. Molecular investigation of RUES ESC lines infected with K219T-LMNA lentivirus. (A) Gating strategy and cell populations (GFP^{pos}- and GFP^{neg}) selected for the sorting are shown. **(B)** RT-PCR comparing *SCN5A* gene expression in GFP^{neg} and K219T-GFP^{pos} CMs isolated through FACS. Data are represented relative to GFP^{neg} samples and normalized to expression of *HPRT* and *18S* housekeeping genes. All values are reported as means ± SD. *p< 0.05, unpaired t-test.

9.5.5. Isogenic control lines

In order to unequivocally establish genotype-phenotype correlations and determine the mechanisms behind the pathology, we combined iPSC technology with a CRISPR/Cas9 genome editing approach and generated iPSC lines, in which the *LMNA* mutations have been corrected (isogenic lines). This part of the study (strategy design) has been conducted in collaboration with the laboratory of Prof. Charles E. Murry, University of Washington (Seattle, WA, USA).

As first step we identified closest "TTAA" sites to both mutations (about 130bp from mutations sites), in order to minimize the editing "scar". Then, we designed single guides RNA (sgRNAs) spanning the TTAA site for each targeting sequence, and cloned them into the enhanced specificity SpCas9 (eSpCas9) plasmid (Fig.35). Targeting vectors was constructed from the MV-PGK-Puro-TK plasmid, containing a piggyBac transposon and specific selection cassettes containing both positive and negative selectable markers (puromycin resistance and thymidine kinase conferring fialuridine sensitivity). Details of lines generation are provided in materials and methods chapter.

The protocol is adapted from Yusa K et al (Yusa 2013) and the workflow is illustrated in Fig.34 A-B. In brief, a vector containing a piggyBac (pb*LMNA*) selection-cassette was used to target *LMNA* locus, between exon 3 and exon 4. Using CRISPR/Cas9 strategy, the pb*LMNA* vector together with eSpCas9 guide plasmid were transfected into K219T and R190W-LMNA iPSCs.

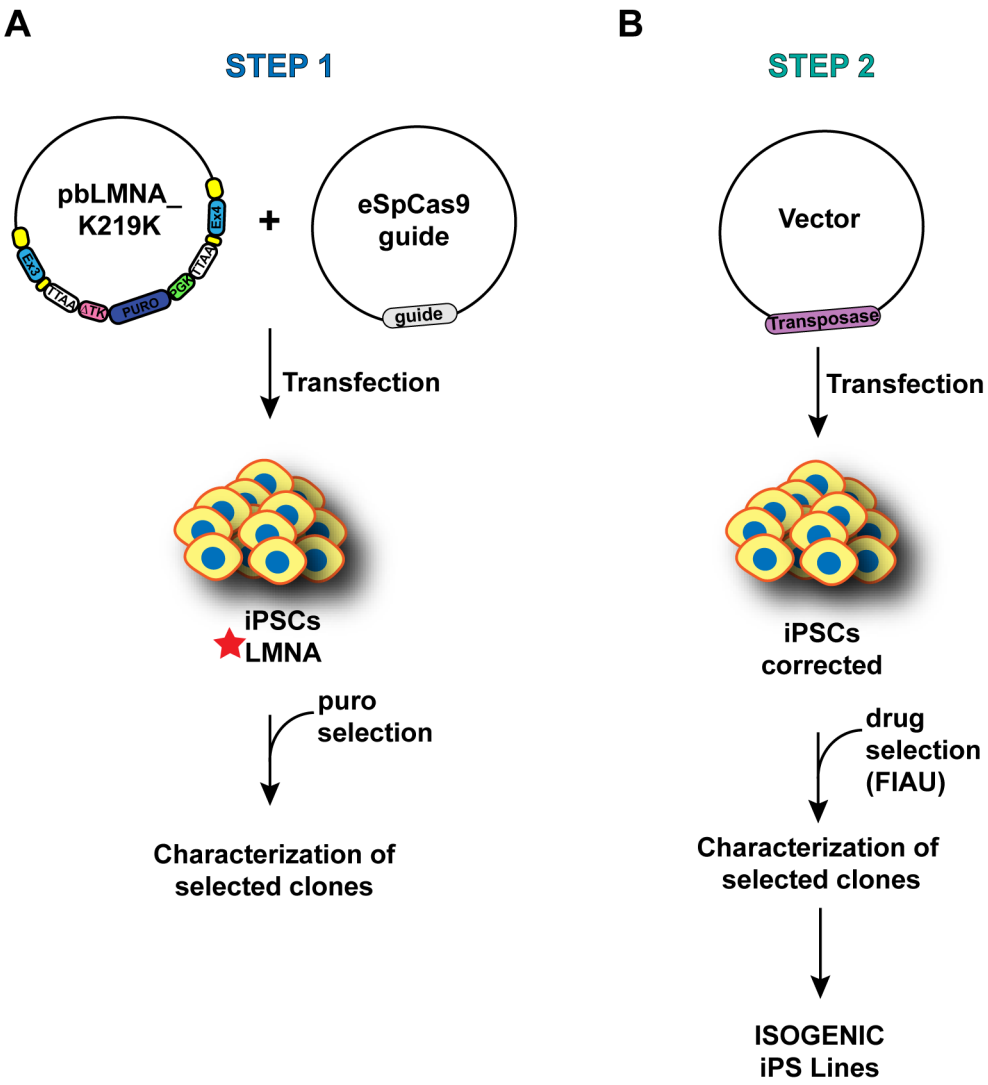

Figure 34. Schematic representation of the workflow for the generation of the isogenic control lines, using the piggyBac transposon system. *LMNA* mutations are indicated by the red star.

For the first step, 75,000 iPSCs were seeded in each well of 6-well plate and transfected with 1 µg of DNA, equally divided between eSpCas9-*LMNA* and pb*LMNA*_K219K. Targeted cells were drug-selected by adding puromycin at a concentration of 1 µg/ml for the first 4 days, and then reduced to 0.5 µg/ml. After 10 days, isolated clones were manually picked and genotyped (Fig. 36-A). Positive clones were further characterized by Sanger sequencing, karyotyped and expanded. To remove piggyBac, K219K_PB_iPSCs were transfected using a transposase expression vector (Fig. 34-B). After 1 week cells were negatively selected by adding 400 nM of fialuridine to the culture media. Individual clones were isolated after 7

days of selection and screened by PCRs (Fig.36-A). Positive clones were sequenced to confirm the correction of the *LMNA* mutation and then analysed for karyotype verification (Fig.36-B and -C). In addition, we already generated corrected lines also from LMNA#3 and R190W#B clones, which will be included in future investigations and analyses.

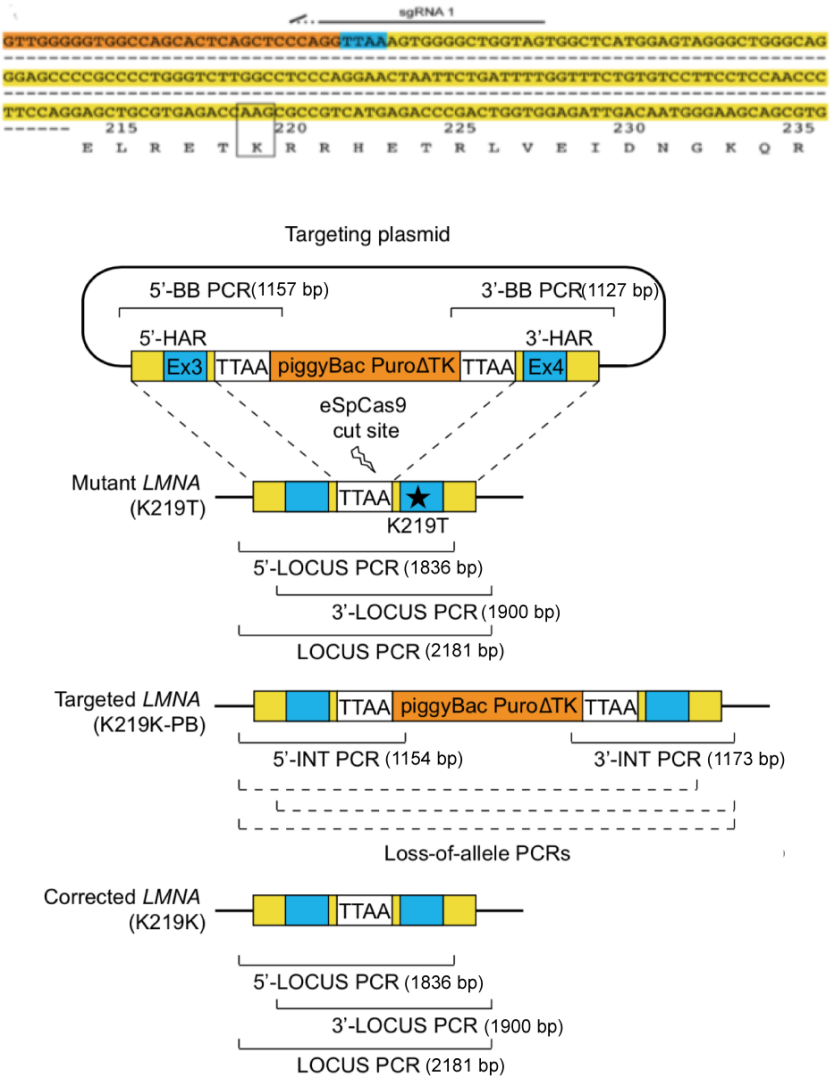

Figure 35. Schematic view of the gene correction strategy. Upper panel: representation of the endogenous "TTAA" site in the third intron of *LMNA* and located 135 bp upstream to the AAC mutation in exon 4 leading to the K219T change, and of the single guide RNA (sgRNA) sequence. The bottom panel gives a schematic view of the gene correction strategy, including the specific PCRs used for the genotyping.

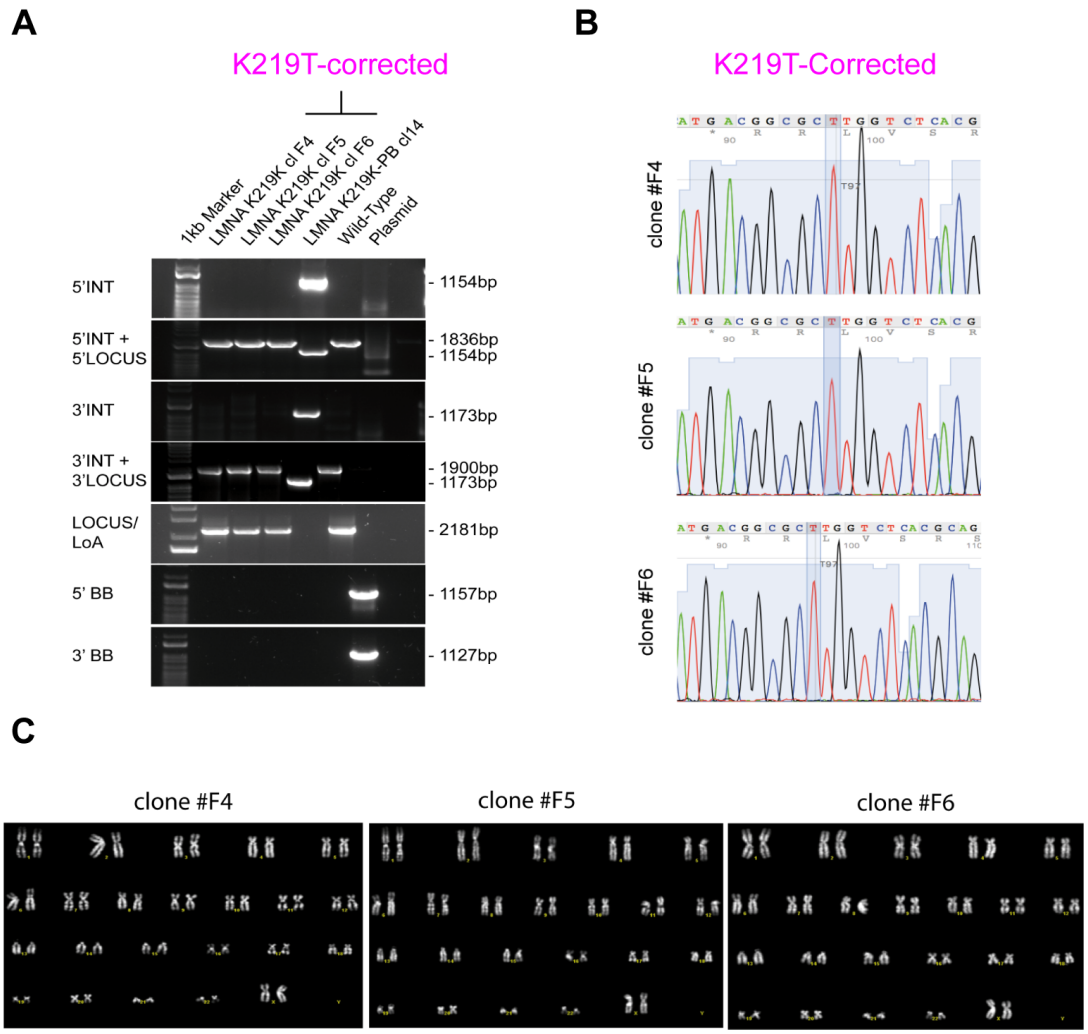

Figure 36. Characterization of corrected-lines. (A) Genotyping PCRs for the three lines generated from the K219T LMNA #1_2 iPSC line. DNA from a control line and the targeting plasmid, have been included as controls. **(B)** Electropherograms of the three isogenic K219T-corrected iPSC lines generated in this study (clone #F4, #F5, #F6), showing the specific correction of the mutation. **(C)** Karyotype analyses of the three isogenic K219T-corrected clones, confirming that no major genetic abnormalities were induced by the gene editing.

9.5.6. Correction of the mutation by gene-editing rescues both functional and molecular phenotypes of K219T-CMs

Functional analyses by patch-clamp revealed a complete restore of Na^+ currents in K219T-corrected CMs. Indeed, I_{Na} density recorded in corrected lines are totally comparable with those from CNTR-CMs (Fig. 37).

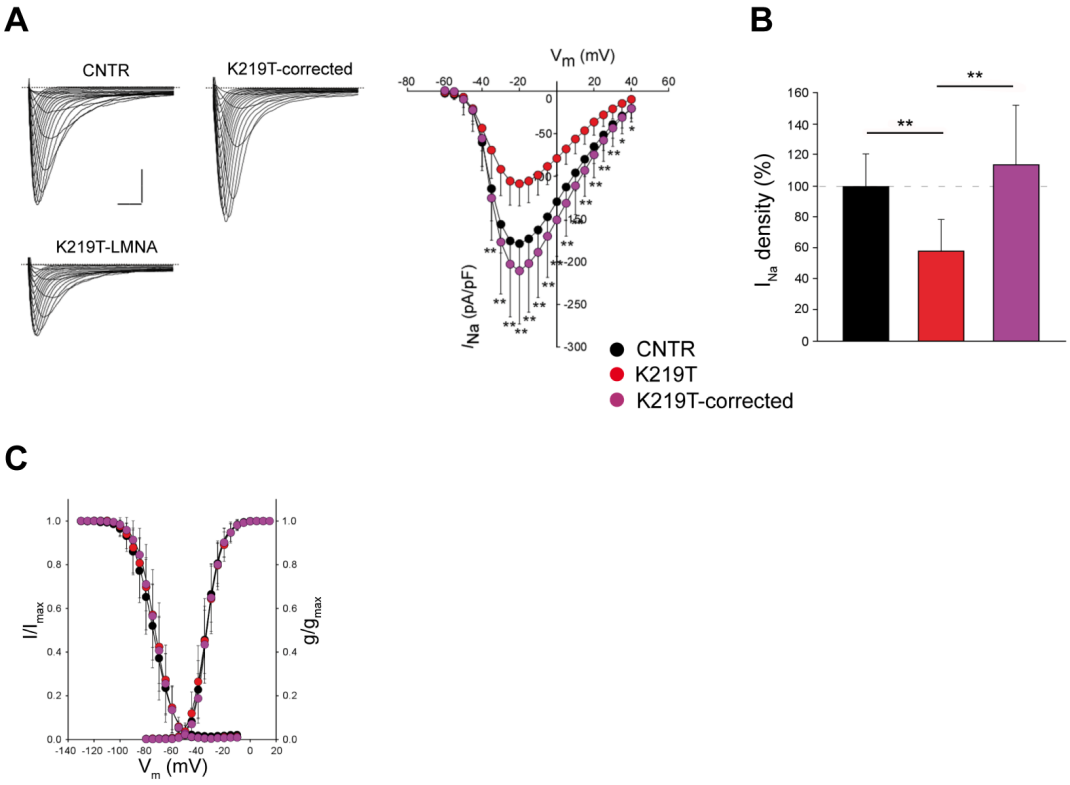

Figure 37. Functional analyses of K219T-corrected isogenic CMs. (A) Left panel: examples of I_{Na} traces recorded in CNTR- (top), K219T-corrected (top) and K219T (bottom) -CMs (Scale bar, 2ms, 50pA/pF). Right panel: I-V curves constructed from average peak sodium current density as a function of voltage command measured in the three conditions described above (CNTR: n=23; K219T-corrected: n=14; K219T: n=22), showing a significant increase in K219T-corrected cells with respect to the parental mutant CMs. **(B)** I_{Na} density, measured at -30 mV, in K219T-corrected CMs (176.94 ± 61.05 pA/pF) relative to K219T-CMs (91.58 ± 30.69 pA/pF) and CNTR-CMs (156.12 ± 33.73 pA/pF) expressed as a percentage. **(C)** Voltage dependences: steady state activation (CNTR: n=23; K219T-corrected: n=14; K219T: n=22); inactivation (CNTR: n=18; K219T-corrected: n=12; K219T: n=17) curves. All values are reported as means ± SD. *adj. p <0.05; **adj.p<0.005 (two-way ANOVA).

Remarkably, reestablishment of sodium current density corresponded to a significant enhancement of *SCN5A* transcription in the K219T-corrected cells (Fig. 38-A); restoration of the functional and molecular phenotype was also coupled with decreased binding of LaminA/C to the *SCN5A* promoter in K219T-corrected CMs (Fig. 38-B), further supporting the hypothesis that impairment of *SCN5A* expression and the consequential effect on the Na^+ current is due to the *LMNA* mutation.

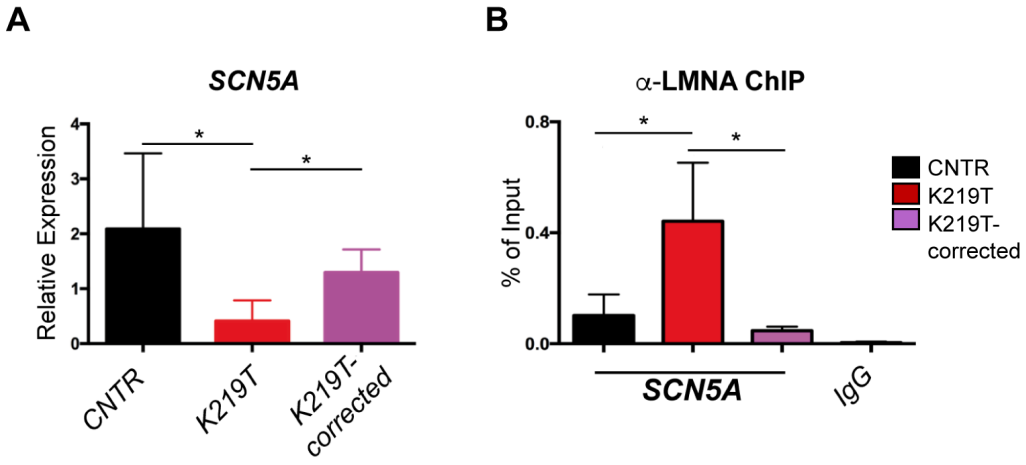

Figure 38. Molecular phenotype of K219T-corrected isogenic CMs. (A) RT-PCR showing that *SCN5A* gene expression in CMs generated from K219T-corrected-iPSCs is restored to levels as in CNTR-CMs. Data are represented relative to CNTR-CMs and normalized to the expression of the housekeeping genes *18S* and *HGPRT*. **(B)** ChIP against LaminA/C, showing loss of LaminA/C binding at the *SCN5A* promoter region in K219T-corrected CMs *vs* mutant K219T-CMs. Levels of LaminA/C binding are instead indistinguishable from those detected in CMs differentiated from control iPSCs. All values are reported as means ± SD. *adj. $p < 0.05$; (two-way ANOVA).

On the whole, our findings support a model in which mutated LaminA/C disturbs the correct transcription of *SCN5A* by favouring the binding of PRC2 to its promoter, leading to decreased peak Na^+ current and slower conduction velocity (Fig. 39).

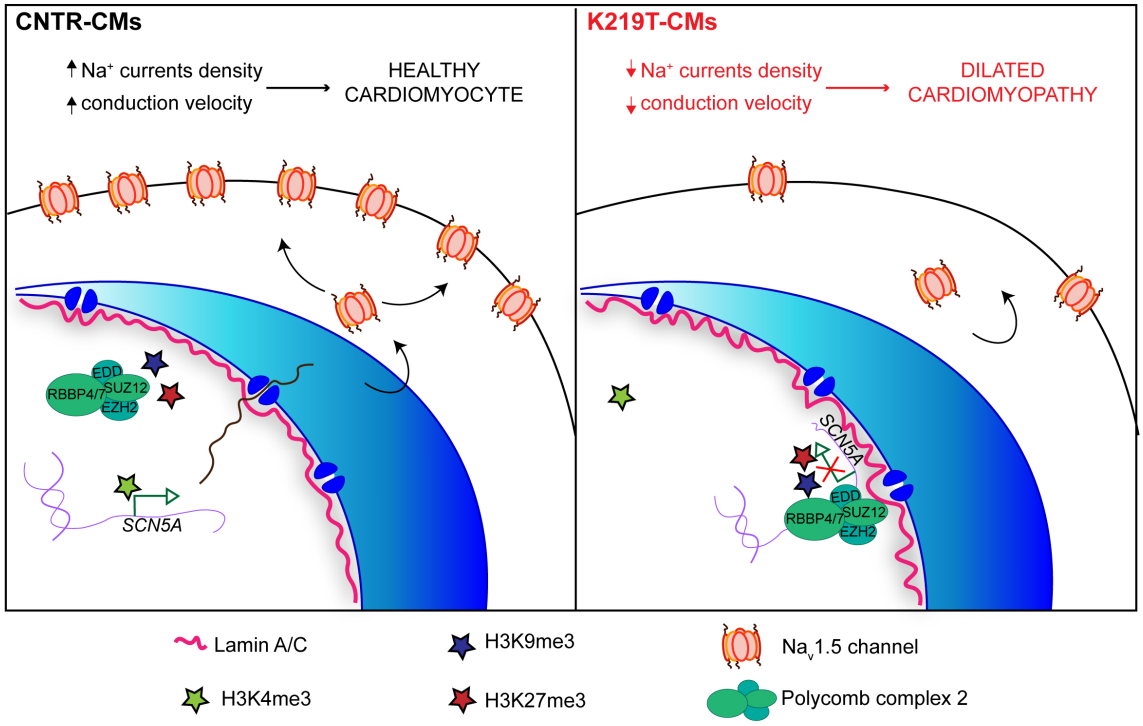

Figure 39. Proposed pathogenic mechanism of action of K219T_LaminA/C in human iPSC-derived CMs. Left: Healthy CMs. The *SCN5A* genomic region is localized in the nuclear interior and is actively transcribed; in this cellular state, the $Na_v1.5$ sodium channel density at the plasma membrane is sufficient to assure proper impulse propagation. Right: Laminopathic CMs. K219T_LaminA/C and PRC2 bind each other with high affinity and are enriched at the *SCN5A* promoter region, where the H3K27me3 (catalysed by PRC2) and H3K9me3 repressive histone marks are also present. In this repressive environment, this genomic region is preferentially sequestered at the nuclear periphery. As a result, *SCN5A* gene transcription is repressed, leading to reduced expression of the $Na_v1.5$ sodium channel at the plasma membrane, which, in turn, affects conduction velocity which results reduced in this condition. This regulatory mechanism may be at the basis of the onset of the conduction defects in patients with *LMNA*-CMP.

9.6. Use of *LMNA*-CMs as a platform for drug testing: a proof-of-concept experiment

Beyond their utility for studying mechanisms of disease, iPSCs have been extensively proven to be a reliable tool also for pharmacological testing (Takahashi and Yamanaka 2016), as long as a good readout may be identified.

In order to validate the translational power of the generated models and the reliability of the main functional outcome emerged from our studies, namely reduction of sodium currents, as pharmacological readout, we perform a series of *proof-of-concept* experiments and tested the effect of a small molecule, called Remodelin, on this functional parameter.

Remodelin is an inhibitor of the N-acetyltransferase 10 enzyme (NAT10), that has been shown to efficiently improve nuclear abnormalities of laminopathic cells, either depleted for LaminA/C or from patients affected by progeria (HGPS -Hutchinson-Gilford Progeria Syndrome) (Larrieu, Britton et al. 2014). Remodelin has been also shown to enhance lifespan of HGPS mice and to ameliorate the associated cardiac pathologies *in vivo* (Balmus, Larrieu et al. 2018).

Nuclear morphology and chromatin disorganization are also typical signs of cells carrying *LMNA* mutations (Toth, Yang et al. 2005; Galiova, Bartova et al. 2008; Chen, Chi et al. 2012) including the one described by us (Roncarati, Viviani Anselmi et al. 2013). Exposure of K219T-CMs to Remodelin rescued average peak Na^+ currents density, increasing it to a level similar to that recorded in CNTR-CMs (Fig. 40-A); indeed, at a membrane potential of -30 mV, there was a 60.7% increase in density (Fig. 40-B). While the molecular mechanism by which Remodelin is acting in this context is still unknown, this finding confirms the importance of nuclear structure on gene expression control, providing indirect evidence of the pathogenic mechanism of the K219T *LMNA* mutation, and suggests that our model may be used as a screening platform for drugs restoring the investigated LaminA/C function.

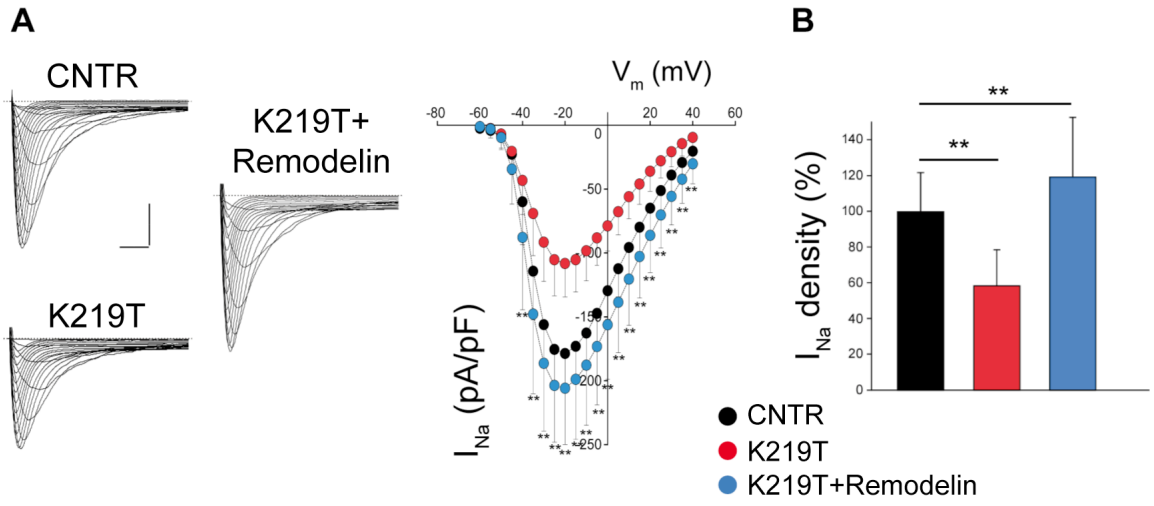

Figure 40. Treatment with Remodelin restores sodium currents density in K219T-CMs. (A) Left column: examples of I_{Na} traces recorded in CNTR- (top, left), K219T LMNA- (bottom, left) and K219T LMNA-CMs exposed to Remodelin (K219T+Remodelin - middle, right) (Scale bar, 2ms, 50pA/pF). Right panel: I-V curves constructed from average peak sodium current density as a function of voltage command measured in the three conditions described above. CNTR-CMs: n=23; K219T *LMNA*-CMs: n=22; K219T *LMNA*-CMs + Remodelin: n= 20. **(B)** I_{Na} density, measured at -30 mV, in K219T *LMNA*-CMs exposed to Remodelin (186.39 ± 52.96 pA/pF) relative to K219T-LMNA (91.58 ± 30.69 pA/pF) and CNTR-CMs (156.12 ± 33.73 pA/pF) expressed as a percentage. All values are reported as means ± SD. **p < 0.005, unpaired t-test.

9.7. Effect of LaminA/C mutations on contractile pathways: molecular and functional studies

9.7.1. K219T LaminA/C mutation modulates genes involved in contraction of the cardiac muscle

Based on the results from RNA-sequencing experiments, we next focused on the muscle contraction pathway and assess whether the functionality of iPSC-CMs was affected by Lamin A/C mutations. From the analysis of transcriptomic data, *MYH6*, *MYBPC3*, *DES*, *TCAP*, *TRIM63*, *TNNT2* emerged as the main mis-regulated genes which encode proteins with key functions in muscle contraction.

In a first instance, we validated the genes selected from the bioinformatics analysis by real time RT-PCR and confirmed they were all down-regulated in K219T-CMs compared to the CNTR (Fig.41-A). Next, we focused on two of these, *TRIM63* and *TNNT2* genes, and tested whether the down regulation of their expression in K219T-CMs was due to Lamin A/C mutation. ChIP experiments against LaminA/C confirmed an enrichment of the protein on the promoter region of both *TRIM63* and *TNNT2* genes in K219T-CMs (Fig. 41-B), supporting the hypothesis that LaminA/C is directly involved in the epigenetic control of the expression of both genes and that the K219T mutation can interfere with this regulatory mechanism resulting in an impairment of their transcription.

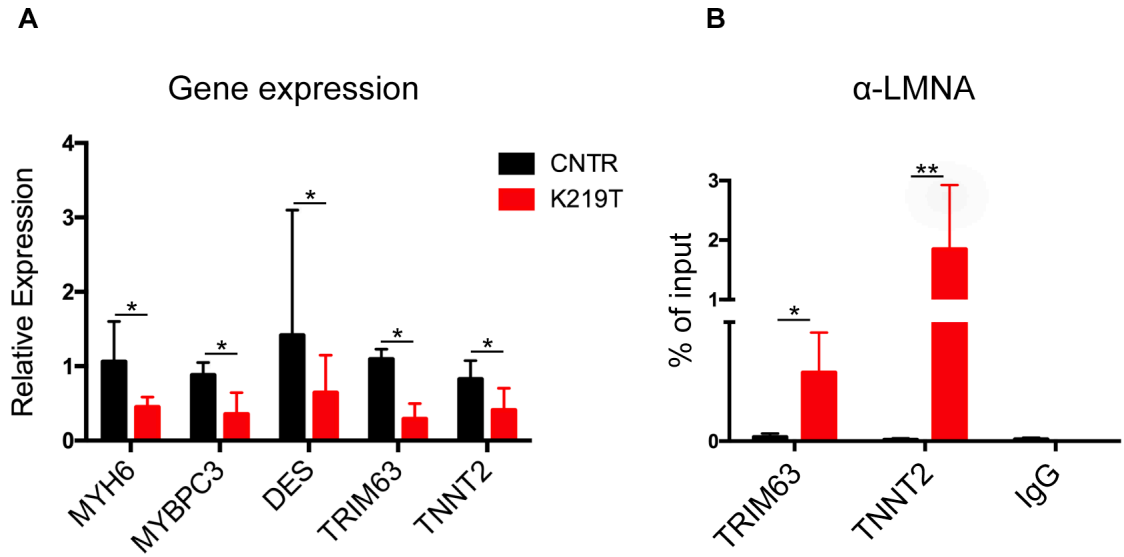

Figure 41. Effect of LaminA/C mutations on contractility genes. (A) Real-time PCR showing reduced expression of genes involved in cardiac contraction in CMs generated from K219T-iPSCs in respect to those differentiated from CNTR cells; **(B)** ChIP analysis in CNTR and K219T-CMs using antibody against LaminA/C. The graph shows an increased binding of LaminA/C at the promoter region of *TRIM63* and *TNNT2* genes in K219T-CMs. Data are presented as percentage of input chromatin precipitated and relative to 2 independent iPSC clones from each subject. All values are reported as means ± SD. *p<0.05; **p<0.01 (unpaired t-test).

9.7.2. Assessment of contractile properties of *LMNA*-CMs

In order to establish the impact of LaminA/C mutations on CMs contractility parameters, we performed functional analyses using the IonOptix microscope technique (Feaster, Cadar et al. 2015; Pointon, Harmer et al. 2015). In the same experimental setting, we evaluated both contraction force and intracellular calcium dynamics. To assess the amount of Ca^{2+}, iPSC-CMs were loaded with Fura-2 acetoxymethyl ester, Fura-2 AM (Molecular Probes Inc, Eugene, OR) (Fig. 41-A). Then, spontaneous contractions following electrical (Fig. 42-B) or chemical stimulations (Fig. 42-C), were recorded.

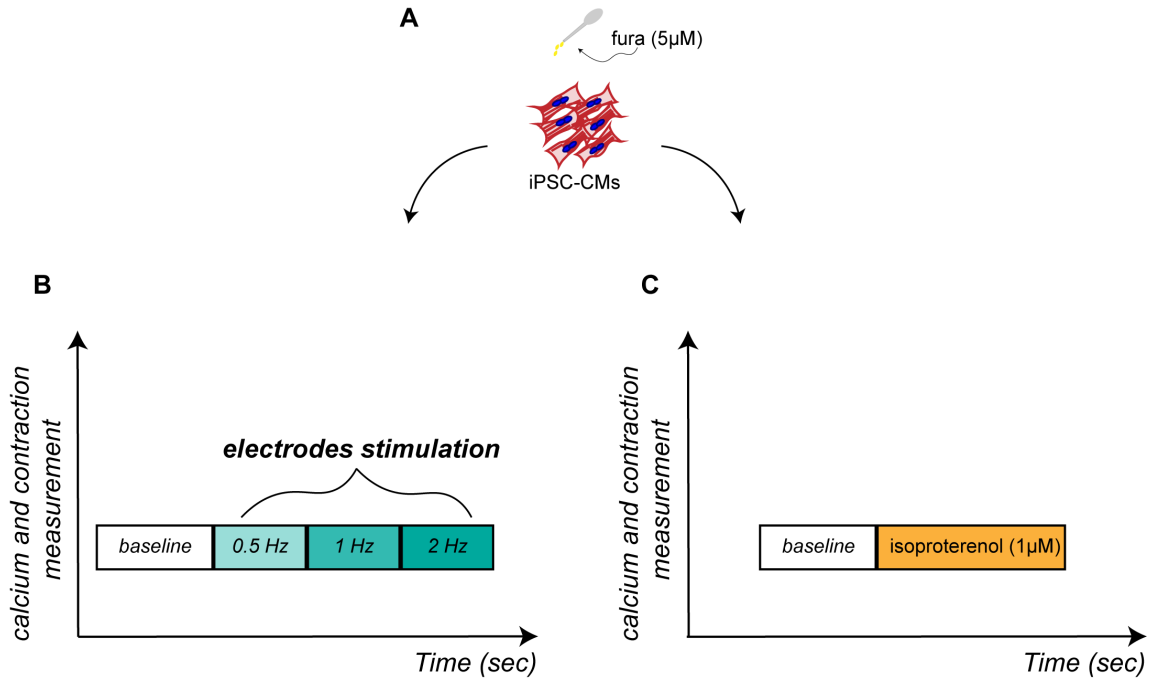

Figure 42. Schematic representation of the approach used for functional measurements using IonOptix system. (A) iPSC-CMs were loaded with FURA-2 (5μM) to measure calcium transients and then, in order to perform contraction measurements, CMs from both control and LMNA mutated lines, were recorded with the following protocols: the baseline - spontaneous beating - followed by either electrodes stimulation (0.5, 1 and 2 Hz) **(B)** or with β-adrenergic agonist isoproterenol **(C)**.

To analyse contractility, we employed a cell length IonOptix protocol, instead of the commonly used one which is based on evaluation of sarcomere length; this is because of the smaller and thinner morphology of iPSC-CMs sarcomeres compared to mouse adult CMs. Example of traces from calcium transients and contraction recordings are shown in the Figure 43 and have been recorded for each analysed cell.

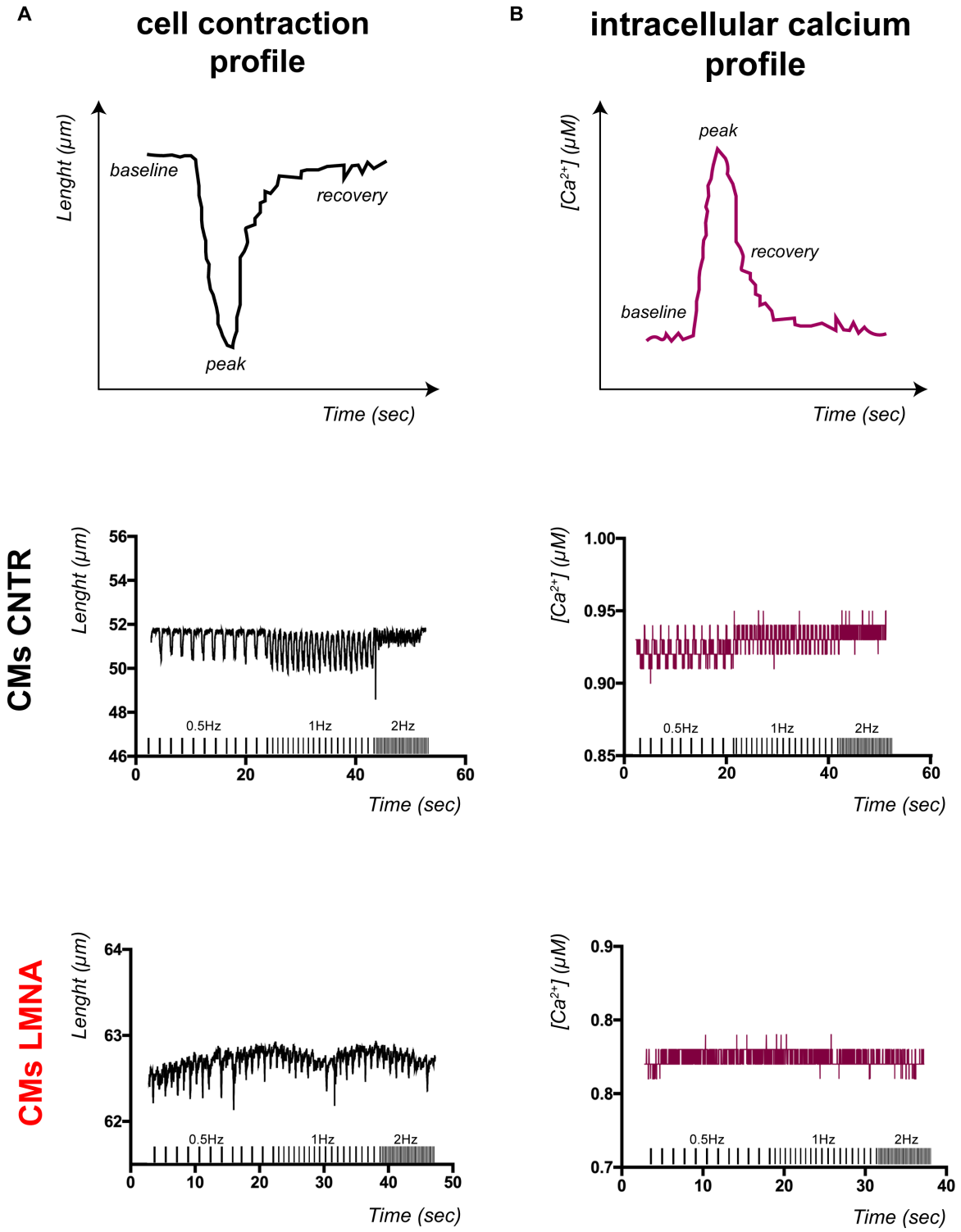

Figure 43. (A) Top: Schematic representation of cell contraction recordings using IonOptix system. Bottom: representative trace of iPSC-CMs contraction (CNTR labelled in black and LMNA labelled in red). **(B)** Top: schematic representation of Ca^{2+} measurements in cells loaded with FURA-2 (an intracellular calcium indicator). Bottom: representative trace of intracellular calcium measurements in iPSC-CMs (CNTR labelled in black and LMNA labelled in red).

Results from these experiments are shown in the Figure 44 and indicates a decrease in cluster shortening in CMs carrying the *LMNA* mutations when compared with those generated from control iPSCs. Furthermore, mutant CMs fail to respond to electrodes stimulation (0.5Hz, 1Hz, 2Hz). This data is in agreement with those previously obtained during assessment of conduction velocity of K219T-CMs (see **Figure 22**), reinforcing the concept of a defective response to ionotropic stimulation in presence of LaminA/C mutations. Mechanisms behind this phenotypic trait are still under investigation.

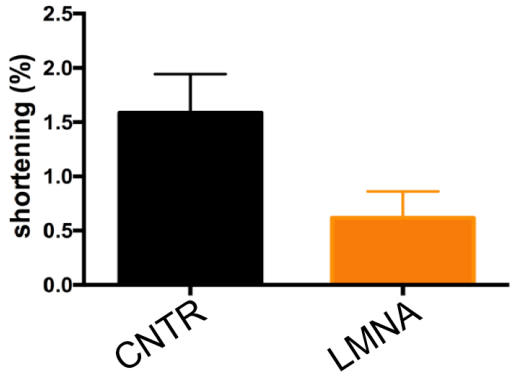

Figure 44. Shortening parameter measured in LMNA- and CNTR-CMs. The graph shows a decrease of cluster shortening parameter (an index of contractility) in LMNA-CMs compared to CNTR-CMs. *LMNA* samples are indicative of data from K219T- and R190W-CMs.

10. CHAPTER DISCUSSION AND FINAL REMARKS

The heterogeneous clinical phenotypes of laminopathies represent the main limitation for the identification of the molecular mechanisms underlying the disease and for the development of effective therapies. Genetically-modified animal models, immortalized cell lines and primary human cells have been extensively used to study the effect of LaminA/C mutations in different contexts; however, dissection of the mechanisms responsible for the disease is still incomplete, especially for those tissues/organs that are of difficult accessibility or for which human and animal physiology highly differs, as the heart (Arimura, Helbling-Leclerc et al. 2005; Mounkes, Kozlov et al. 2005).

Our study aimed at overcoming such limitations and developed a model system to dissect functional and molecular mechanisms of cardiac defects associated to laminopathies. At the heart level, mutation in the *LMNA* gene cause DCM, usually anticipated by various CSDs (Arbustini, Pilotto et al. 2002; Brodt, Siegfried et al. 2013; Zhang, Kieckhaefer et al. 2013). Defects of the contractile apparatus represent, together with the conduction abnormalities, major clinical phenotypes of laminopathies and have been detected in laminopathic cells derived from patients exhibiting skeletal or cardiac disorders. Cellular abnormalities, including irregular nuclear shape and susceptibility to electrical stress, were already described on laminopathic fibroblasts (Goldman, Shumaker et al. 2004; Scaffidi and Misteli 2006; Shumaker, Dechat et al. 2006) or iPSC-CMs derived from patients with LMNA-CMP (Siu, Lee et al. 2012; Lee, Lau et al. 2017; Chatzifrangkeskou, Yadin et al. 2018). However, described mechanisms are still incomplete.

Here we generated a human model of LMNA-CMP to investigate the role of LaminA/C mutations in the proper cellular context: the human cardiomyocytes. To this goal, we employed iPSC technology combined with a wide range of different techniques and dissected cellular and molecular mechanisms responsible for the disease phenotype.

First of all, our analyses confirmed an increased size of CMs obtained from K219T- and R190W-iPSCs, demonstrating that the generated models are able to recapitulate a typical trait of DCM. Furthermore, those cells also display disorganization of the sarcomeric

structure by immunofluorescence, which is another key feature of *LMNA*-CMPs. This is in agreement to what already described in iPSC-CMs by other groups, and further support the reliability of the employed model for investigating the mechanisms underlying the disease (Chatzifrangkeskou, Yadin et al. 2018).

Electrophysiological characterization by patch clamp highlighted, as major functional phenotypes, significant alterations of AP properties of cardiac excitability. In particular, maximal upstroke velocity (dV/dt_{max}) was the major electrical phenotype that emerged altered in mutant CMs. This defect was linked to a profound impairment of Na^+ current density, that leads to cardiac impulse propagation defects.

Even though a link between LaminA/C mutations and $Na_v1.5$ regulation has been previously reported, results emerged from previous studies are contradictory and conducted on other cellular systems. Liu et al reported an inhibitory effect of R644C and R190W *LMNA* mutations on $Na_v1.5$ currents in HEK293T cells (Liu, Shan et al. 2016). Conversely, Markandeya Y.S. and colleagues described an increased peak of I_{Na} and the prolongation of action potential duration in ventricular CMs isolated from N195K/N195K homozygous mice (Markandeya, Tsubouchi et al. 2016). Our findings get across these discrepancies and described this phenotype in a relevant pathophysiological context in humans that is a patient-specific model of *LMNA*-CMP generated through differentiation of iPSCs into CMs.

Density of voltage-gated Na^+ current is at the basis of the excitability of the cardiomyocyte and is a major determinant of impulse propagation across the myocardium (Grant 2009; Rook, Evers et al. 2012). *SCN5A* gene encodes the main cardiac voltage-gated sodium channel α-subunit, $Na_v1.5$; mutations of this gene have been linked to impaired expression or function of the $Na_v1.5$ protein and have been associated to various forms of hereditary arrhythmias, such as Long QT syndrome type 3 (LQTS3), Lenègre-Lev disease and Brugada syndrome (Li, Yin et al. 2018). Alterations of *SCN5A* gene, and its encoded protein $Na_v1.5$, have been also frequently reported in common cardiac disorders, including heart failure, further indicating their fundamental role in the regulation of cardiomyocyte excitability

(McNally and Mestroni 2017). Moreover, conduction disorders and sudden death also represent typical hallmarks of CMP due to *LMNA* mutation (McNally and Mestroni 2017; Nomura 2018). Altogether, these evidences strongly support a pathogenic role of diminished Na^+ channel expression in the occurrence of the conduction disorders detected in *LMNA*-CMs.

In line with these observations, conduction velocities were also found considerably decreased in confluent multicellular strands of K219T-CMs. Cardiac excitation depends on both AP generation from individual cells and cell-to-cell conduction of the generated AP. This latter event occurs through gap junctions (Kleber and Rudy 2004; Mounkes, Kozlov et al. 2005; Veeraraghavan, Gourdie et al. 2014). On this regard, mislocalization or misexpression of Connexin-43 (CX-43) have been previously associated to conduction defects in LMNA-CMP (Sun, Yazawa et al. 2012; Veeraraghavan, Gourdie et al. 2014; Macquart, Juttner et al. 2018). CX-43 is a gap junction protein, which, in the heart, localizes at the intercalated disks (end-to-end coupling) of CMs, where it contributes to establish intercellular conductance and impulse propagation (Molica, Meens et al. 2014; Kelly, Simek et al. 2015; Leybaert, Lampe et al. 2017). In our model, we did not found abnormal expression of *CX-43* gene; however, we could not exclude the possibility that an anomalous localization of the protein may occur, leading to a reduced gap junctional coupling and contributing to the conduction defects detected in mutant *LMNA*-CMs. In support of this, we observed that the reduction of CVs in K219T-CMs was more accentuated than the decrease in dV/dt_{max} and Na^+ current density registered in single-cell preparations. The stronger difference detected on CV than on the excitability parameters may be due to an additive effect of the intercellular conductance pathway to the sodium-based excitability disturbances.

Given the major role of A-type lamins in transcriptional regulation and chromatin organization, we hypothesize that an alteration of the transcriptional program caused by mutations in LaminA/C may underlie the functional defects found in *LMNA*-CMs.

Molecular studies targeting sodium channel protein $Na_v1.5$ and its encoding gene, *SCN5A*, revealed a significant reduction of both protein and transcript in mutant CMs accompanied by an increased binding of LaminA/C and deposition of the H3K9me3 and H3K27me3 markers at the promoter of the gene. These evidences strongly support the hypothesis of an epigenetically-mediated modulation on *SCN5A* gene driven by LaminA/C and defective in case of occurrence of *LMNA* mutations. Along this line, it is now widely recognized that, besides its structural role in the nucleus, LaminA/C take also part in the control of gene transcription either by its direct interaction with chromatin and DNA or through the binding to specific chromatin associated proteins and transcription factors (Johnson, Nitta et al. 2004; Reddy, Zullo et al. 2008; Zuleger, Robson et al. 2011; Harr, Luperchio et al. 2015). When LaminA/C gene is defective, these interactions may result altered (Worman and Courvalin 2002; Wilson and Foisner 2010), and changes in specific gene transcription patterns are likely to occur as major consequences.

The interaction between lamins and chromatin mainly occurs through the LADs, namely Lamin Associated Domains, which are regions of the genome of about 0.1-10Mb that include mostly, but not exclusively, repressed genes. Specific LADs distribution profiles have been found in many different cell types and proposed to contribute to define cell identity; in addition to this, recent studies have shown rearrangements of LADs occurs in disease and may define a specific disease state (Guelen, Pagie et al. 2008; Kind, Pagie et al. 2013; Lund, Oldenburg et al. 2013; Cesarini, Mozzetta et al. 2015; Perovanovic, Dell'Orso et al. 2016). It is therefore highly probable that changes in gene expression occurring in cells from patients carrying different types of LaminA/C mutations (i.e. progeroid disorder, lipodystrophies and muscle dystrophy) were due to gain/loss of LADs, affecting genome architecture (Perovanovic, Dell'Orso et al. 2016; Paulsen, Sekelja et al. 2017). Interestingly, *SCN5A* was also found located in a LAD in other cell types (Lund, Oldenburg et al. 2013); as such it represents a potential target gene which expression may be altered in case of LAD remodelling. The analysis of LaminA/C binding at the *SCN5A* promoter locus during

differentiation of iPSC into CMs, confirmed this hypothesis, supporting the notion that LAD rearrangement may occur in presence of the *LMNA* mutation also in CMs. Therefore, our findings strongly sustain a view by which the epigenetic regulation of *SCN5A* mediated by LaminA/C may be a cause of the disease.

More in detail, in the model we propose here, mutant LaminA/C form a repressive complex with PRC2, which acts inhibiting *SCN5A* gene transcription through the repressive action of LaminA/C itself and the deposition of the H3K27me3 repressive marker at the promoter of the gene. In addition to this, *SCN5A* gene also resulted preferentially located at the nuclear periphery, in a repressive environment.

Therefore, the proposed model sees two additional "actors" involved in the modulation of the expression of *SCN5A* gene: PRC2 and the nuclear periphery. Results from 3D-FISH experiments indicated a significantly different nuclear localization occurring in K219T-CMs, with the *SCN5A* gene probe preferentially detected at the nuclear periphery. This further contributes to determine a repressive environment, leading to a down-regulation of sodium channel gene and resulting in diminished sodium current, and may be indicative of changes in LADs conformation.

Additionally, together with LaminA/C, we also found an enrichment of PRC2 at the same *SCN5A* promoter locus. Results from Super Resolution Microscopy (STED) experiments revealed a higher colocalization of LaminA/C and PRC2 in mutant CMs and a different distribution of the PRC2/LaminA/C complex in presence of the mutation, suggesting that a single point mutation in *LMNA* could differentially mediate the specific affinity of LaminA/C protein for other binding factors, as the Polycomb complex. STED experiments have also shown a portion of PRC2/LaminA/C complex constrained to the nuclear periphery in K219T-CMs, further supporting the view that a regulatory circuit involving LaminA/C and PRC2 is acting on *SCN5A* gene at that cellular compartment. However, it is worth to point out that a significant portion of the complex has also been identified in the nuclear interior. This is line with previous studies indicating a link between LaminA/C and the intra-

nuclear localization of PcG proteins and with their preferential nuclear compartmentalization in cells lacking LaminA/C (Marullo, Cesarini et al. 2016).

Based on the functional interaction of nucleoplasmic LaminA/C with PRC2, previously described by Marullo et al, and on the discrepancies in proteins' distribution profiles found between K219T–and CNTR-CMs, we hypothesized that differences in proteins' interaction affinity may exist in the context of the pathology. Co-IP experiments confirmed this hypothesis and showed a higher binding of LaminA/C to PRC2 in K219T-CMs, indicative of the higher affinity of K219T mutated form of LaminA/C for PRC2. This is also in line with the similar distribution profiles of the two proteins in the 3D nuclear space and with the different proteins' dynamics we observed.

The concept that a correlation between LaminA/C mutations and protein dynamics may exist is not new and it has been recently described (Serebryannyy, Ball et al. 2018). In this study, the authors illustrated a new method, called single molecule tracking (SMT) technology, to distinguish the behaviour of LaminA/C protein carrying different mutations within the nuclear space at the single-cell level and showed substantial differences in the distribution of the LaminA/C mutants, identifying peripheral and nuclear interior subpopulations. These results are in line with our 3D-STED findings and reinforce the notion that changes of protein's dynamics may occur in presence of different *LMNA* mutations in CMs nuclei. This proteins' relocation within the nucleus is expected to act in the control of gene transcription in a cell- specific and time-dependent manner.

In view of these global rearrangements throughout the nucleus, we cannot exclude an effect on other disease-relevant genes, besides the main identified target *SCN5A,* in our cellular model; on the contrary, transcriptional reprogramming is likely to occur at the global level in cardiac cells, leading to dis-regulation of genes involved in different pathways and disease.

In agreement with this assumption, results from RNA-seq analysis in mutant and control CMs showed a differential expression of genes involved in cardiac contraction and cell

metabolism, other two relevant pathways for *LMNA*-CMP. Preliminary data from gene expression and ChIP performed on two of the downregulated genes of the contraction pathway indicated a mechanisms of regulation similar to the one described for *SCN5A*, showing an enrichment of LaminA/C protein on their promoter in K219T-CMs in respect to the controls. These additional findings further support the solidity of the mechanisms proposed for *SCN5A* regulation and, more generally, strengthen the hypothesis that LaminA/C can function as a docking platform and selectively modulate the expression of specific target genes.

Improving the knowledge of the molecular basis underlying the *LMNA*-CMP clinical phenotype constitutes a mandatory requisite to enhance the patients' lifespan and to improve currently available therapeutic approaches, still inadequate to specifically treat *LMNA* patients. Available medical treatments are, in fact, more directed to control symptoms and to prevent disease progression other than to cure the origin of the disease.

Besides the important mechanistic advancement, results obtained in this Thesis work also allowed to identify *SCN5A* gene and Na^+ current density as new pharmacological targets for conduction defects in *LMNA*-CMPs.

It is indeed conceivable that pharmacological modulation of sodium channel activity or expression, for example by sodium channel agonists, epigenetic drugs or gene replacement, will lead to an improvement of the functional phenotype in these cells. This concept is further sustained by results from K219T-corrected lines that demonstrated the casual link between K219T-LMNA mutation, *SCN5A* gene transcriptional regulation and Na^+ currents, showing the rescue of the electrophysiological phenotype (normalization of Na^+ currents density) in isogenic K219T-corrected LMNA –CMs and the reestablishment of *SCN5A* expression level as in the controls through the restore of its epigenetic regulation as in the healthy condition. A further confirmation of *SCN5A* as potential therapeutic target comes from preliminary data by us that show a beneficial effect of lentiviral-mediated overexpression of *SCN5A* gene

in mutant K219T-CMs on both, sodium currents density and maximal upstroke velocity (not shown).

Finally, we also provided evidence that iPCS-derived CMs represent a reliable platform for drug testing and that sodium current density may be successfully employed as functional outcome, as indicated by the experiments on Remodelin (Larrieu, Britton et al. 2014), in which the functional defects of *LMNA*-CMs were blunted by restoring sodium current density to a normal level. While the molecular mechanism by which Remodelin is acting in this context is still unknown, we assume that it can act either on gene expression by rescuing the morphology of the nucleus, and consequently by reorganization of chromatin, or by shuttling the Na^+ channels that are left at the plasma membrane through a microtubule-mediated mechanism (Shen, Zheng et al. 2009).

NAT10 activity was indeed linked to microtubules stabilization, so that the mechanism of action of Remodelin in CMs may rely on modulation of the nucleo-cytoplasmic transport through midbody and microtubules machinery. In line with this hypothesis, it has been recently proposed that NAT10 inhibition could restore the Transportin-1/NPC protein complex (TNPO1-NUP153) translocation into the nucleus in HGPS, resulting in the proper assembling of nuclear pore complexes (NPCs) and in the restore of the other NPC-dependent activities (Larrieu, Vire et al. 2018). Therefore, it is reasonable that also *LMNA* mutations could lead to defects in the nuclear-cytosol exchanges through microtubules machinery and that the transcriptional changes as well as the different protein dynamics and the altered interaction affinity showed in mutant CMs, could be the downstream effects of *LMNA* mutations.

Interestingly, Remodelin has been also shown effective *in vivo* in ameliorating the HGPS phenotype by enhancing the healthspan in $Lmna^{G609G}$ HGPS mouse model (Balmus, Larrieu et al. 2018); this further sustains the potential validity of this molecule in treatment of *LMNA* patients. On this regard, we have accumulated preliminary evidence in CNTR-CMs (data not shown), showing a boost effect of Remodelin on sodium channel and AP parameters,

suggesting that inhibition of NAT10 can be beneficial for CMs fitness. These data also support the potential of Remodelin as specific enhancer of $Na_v1.5$ currents, rather than as a specific drug for *LMNA*-CMP. Further investigations on the molecular mechanisms behind the observed functional effects will shed light on the specific pathways targeted by Remodelin in the CMs and help establishing its actual therapeutic value for cardiac diseases.

In conclusion, this thesis describes a new pathogenic mechanism for LMNA-CMP, dependent upon transcriptional changes driven by mutant LaminA/C. In particular, for the conduction defects, one of the most severe *LMNA*-CMP associated phenotype, *SCN5A* was identified as the major target gene. Whether the described effect on this gene is selective for certain mutations affecting specific protein domains or is more broadly linked to altered LaminA/C conformation is still unclear and needs further investigation. The identification of a conserved LaminA/C-dependent epigenetic mechanism that regulates transcription of genes belonging to other two disease-relevant pathways, cardiac metabolism and muscle contraction, further supports the validity of the proposed model and provides us with novel biological targets. This last achievement represents an important step forward for the development of more specific drugs to treat *LMNA*-CMP.

In this Thesis we demonstrated the robust association between the *LMNA* mutations and the observed patient phenotype. However, some limitations are yet to be overcome.

Among them, the immature state of iPSCs-derived CMs represent a critical issue and their management in late-onset diseases is still debated.

In addition to the consideration of the iPSC-CMs maturation stage, there is another limitation of this study. It would be very interesting to investigate the transcriptional effect of the LaminA/C mutations through whole-genome approach. Indeed, a global transcriptional reprogramming is likely to occur in CMs in presence of mutated LaminA/C, altering regulation of key genes in disease-progress (i.e. genes involved in contractile machinery and cell metabolism). However, genome-wide investigations and genome conformation analysis

are necessary to specifically address how LaminA/C moves into cell nuclei and can control transcription.

11. Bibliography

An, M. C., N. Zhang, et al. (2012). "Genetic correction of Huntington's disease phenotypes in induced pluripotent stem cells." Cell Stem Cell **11**(2): 253-263.

Arbustini, E., P. Morbini, et al. (2000). "Familial dilated cardiomyopathy: from clinical presentation to molecular genetics." Eur Heart J **21**(22): 1825-1832.

Arbustini, E., A. Pilotto, et al. (2002). "Autosomal dominant dilated cardiomyopathy with atrioventricular block: a lamin A/C defect-related disease." J Am Coll Cardiol **39**(6): 981-990.

Arimura, T., A. Helbling-Leclerc, et al. (2005). "Mouse model carrying H222P-Lmna mutation develops muscular dystrophy and dilated cardiomyopathy similar to human striated muscle laminopathies." Hum Mol Genet **14**(1): 155-169.

Balmus, G., D. Larrieu, et al. (2018). "Targeting of NAT10 enhances healthspan in a mouse model of human accelerated aging syndrome." Nat Commun **9**(1): 1700.

Benedetti, S., I. Menditto, et al. (2007). "Phenotypic clustering of lamin A/C mutations in neuromuscular patients." Neurology **69**(12): 1285-1292.

Berecki, G., R. Wilders, et al. (2010). "Re-evaluation of the action potential upstroke velocity as a measure of the Na+ current in cardiac myocytes at physiological conditions." PLoS One **5**(12): e15772.

Bian, Q., N. Khanna, et al. (2013). "beta-Globin cis-elements determine differential nuclear targeting through epigenetic modifications." J Cell Biol **203**(5): 767-783.

Bione, S., E. Maestrini, et al. (1994). "Identification of a novel X-linked gene responsible for Emery-Dreifuss muscular dystrophy." Nat Genet **8**(4): 323-327.

Blelloch, R., M. Venere, et al. (2007). "Generation of induced pluripotent stem cells in the absence of drug selection." Cell Stem Cell **1**(3): 245-247.

Bonne, G., M. R. Di Barletta, et al. (1999). "Mutations in the gene encoding lamin A/C cause autosomal dominant Emery-Dreifuss muscular dystrophy." Nat Genet **21**(3): 285-288.

Briggs, R. and T. J. King (1952). "Transplantation of Living Nuclei From Blastula Cells into Enucleated Frogs' Eggs." Proc Natl Acad Sci U S A **38**(5): 455-463.

Brodt, C., J. D. Siegfried, et al. (2013). "Temporal relationship of conduction system disease and ventricular dysfunction in LMNA cardiomyopathy." J Card Fail **19**(4): 233-239.

Brown, W. T. (1992). "Progeria: a human-disease model of accelerated aging." Am J Clin Nutr **55**(6 Suppl): 1222S-1224S.

Butin-Israeli, V., S. A. Adam, et al. (2012). "Nuclear lamin functions and disease." Trends Genet **28**(9): 464-471.

Cao, N., H. Liang, et al. (2013). "Highly efficient induction and long-term maintenance of multipotent cardiovascular progenitors from human pluripotent stem cells under defined conditions." Cell Res **23**(9): 1119-1132.

Carmeliet, E. and J. Vereecke (2002). "Cardiac Cellular Electrophysiology."

Cesarini, E., C. Mozzetta, et al. (2015). "Lamin A/C sustains PcG protein architecture, maintaining transcriptional repression at target genes." J Cell Biol **211**(3): 533-551.

Chatzifrangkeskou, M., C. Le Dour, et al. (2016). "ERK1/2 directly acts on CTGF/CCN2 expression to mediate myocardial fibrosis in cardiomyopathy caused by mutations in the lamin A/C gene." Hum Mol Genet **25**(11): 2220-2233.

Chatzifrangkeskou, M., D. Yadin, et al. (2018). "Cofilin-1 phosphorylation catalyzed by ERK1/2 alters cardiac actin dynamics in dilated cardiomyopathy caused by lamin A/C gene mutation." Hum Mol Genet **27**(17): 3060-3078.

Chen, C. Y., Y. H. Chi, et al. (2012). "Accumulation of the inner nuclear envelope protein Sun1 is pathogenic in progeric and dystrophic laminopathies." Cell **149**(3): 565-577.

Chen, X., S. Yammine, et al. (2014). "The visualization of large organized chromatin domains enriched in the H3K9me2 mark within a single chromosome in a single cell." Epigenetics **9**(11): 1439-1445.

Cohen, C. J., B. P. Bean, et al. (1984). "Maximal upstroke velocity as an index of available sodium conductance. Comparison of maximal upstroke velocity and voltage clamp measurements of sodium current in rabbit Purkinje fibers." Circ Res **54**(6): 636-651.

Crasto, S. and E. Di Pasquale (2018). "Induced Pluripotent Stem Cells to Study Mechanisms of Laminopathies: Focus on Epigenetics." Front Cell Dev Biol **6**: 172.

Cyganek, L., M. Tiburcy, et al. (2018). "Deep phenotyping of human induced pluripotent stem cell-derived atrial and ventricular cardiomyocytes." JCI Insight **3**(12).

Davis, R. P., C. W. van den Berg, et al. (2011). "Pluripotent stem cell models of cardiac disease and their implication for drug discovery and development." Trends Mol Med **17**(9): 475-484.

De Sandre-Giovannoli, A., R. Bernard, et al. (2003). "Lamin a truncation in Hutchinson-Gilford progeria." Science **300**(5628): 2055.

De Santis, R., L. Santini, et al. (2017). "FUS Mutant Human Motoneurons Display Altered Transcriptome and microRNA Pathways with Implications for ALS Pathogenesis." Stem Cell Reports **9**(5): 1450-1462.

Dechat, T., A. Gajewski, et al. (2004). "LAP2alpha and BAF transiently localize to telomeres and specific regions on chromatin during nuclear assembly." J Cell Sci **117**(Pt 25): 6117-6128.

Dechat, T., B. Korbei, et al. (2000). "Lamina-associated polypeptide 2alpha binds intranuclear A-type lamins." J Cell Sci **113 Pt 19**: 3473-3484.

Dechat, T., K. Pfleghaar, et al. (2008). "Nuclear lamins: major factors in the structural organization and function of the nucleus and chromatin." Genes Dev **22**(7): 832-853.

Deniaud, E. and W. A. Bickmore (2009). "Transcription and the nuclear periphery: edge of darkness?" Curr Opin Genet Dev **19**(2): 187-191.

Di Pasquale, E., F. Lodola, et al. (2013). "CaMKII inhibition rectifies arrhythmic phenotype in a patient-specific model of catecholaminergic polymorphic ventricular tachycardia." Cell Death Dis **4**: e843.

Dittmer, T. A. and T. Misteli (2011). "The lamin protein family." Genome Biol **12**(5): 222.

Dittmer, T. A., N. Sahni, et al. (2014). "Systematic identification of pathological lamin A interactors." Mol Biol Cell **25**(9): 1493-1510.

Drawnel, F. M., S. Boccardo, et al. (2014). "Disease modeling and phenotypic drug screening for diabetic cardiomyopathy using human induced pluripotent stem cells." Cell Rep **9**(3): 810-821.

Eggan, K., K. Baldwin, et al. (2004). "Mice cloned from olfactory sensory neurons." Nature **428**(6978): 44-49.

Eriksson, M., W. T. Brown, et al. (2003). "Recurrent de novo point mutations in lamin A cause Hutchinson-Gilford progeria syndrome." Nature **423**(6937): 293-298.

Evans, M. J. and M. H. Kaufman (1981). "Establishment in culture of pluripotential cells from mouse embryos." Nature **292**(5819): 154-156.

Fanelli, M., S. Amatori, et al. (2010). "Pathology tissue-chromatin immunoprecipitation, coupled with high-throughput sequencing, allows the epigenetic profiling of patient samples." Proc Natl Acad Sci U S A **107**(50): 21535-21540.

Fatkin, D., C. MacRae, et al. (1999). "Missense mutations in the rod domain of the lamin A/C gene as causes of dilated cardiomyopathy and conduction-system disease." N Engl J Med **341**(23): 1715-1724.

Feaster, T. K., A. G. Cadar, et al. (2015). "Matrigel Mattress: A Method for the Generation of Single Contracting Human-Induced Pluripotent Stem Cell-Derived Cardiomyocytes." Circ Res **117**(12): 995-1000.
Feher, J. (2012). "The Cardiac Action Potential." 458-466.
Foisner, R. and L. Gerace (1993). "Integral membrane proteins of the nuclear envelope interact with lamins and chromosomes, and binding is modulated by mitotic phosphorylation." Cell **73**(7): 1267-1279.
Fujiwara, M., P. Yan, et al. (2011). "Induction and enhancement of cardiac cell differentiation from mouse and human induced pluripotent stem cells with cyclosporin-A." PLoS One **6**(2): e16734.
Fusaki, N., H. Ban, et al. (2009). "Efficient induction of transgene-free human pluripotent stem cells using a vector based on Sendai virus, an RNA virus that does not integrate into the host genome." Proc Jpn Acad Ser B Phys Biol Sci **85**(8): 348-362.
Galiova, G., E. Bartova, et al. (2008). "Chromatin changes induced by lamin A/C deficiency and the histone deacetylase inhibitor trichostatin A." Eur J Cell Biol **87**(5): 291-303.
Gaustad, K. G., A. C. Boquest, et al. (2004). "Differentiation of human adipose tissue stem cells using extracts of rat cardiomyocytes." Biochem Biophys Res Commun **314**(2): 420-427.
Gerace, L. and G. Blobel (1980). "The nuclear envelope lamina is reversibly depolymerized during mitosis." Cell **19**(1): 277-287.
Goldman, R. D., D. K. Shumaker, et al. (2004). "Accumulation of mutant lamin A causes progressive changes in nuclear architecture in Hutchinson-Gilford progeria syndrome." Proc Natl Acad Sci U S A **101**(24): 8963-8968.
Goldring, C. E., P. A. Duffy, et al. (2011). "Assessing the safety of stem cell therapeutics." Cell Stem Cell **8**(6): 618-628.
Grant, A. O. (2009). "Cardiac ion channels." Circ Arrhythm Electrophysiol **2**(2): 185-194.
Gruenbaum, Y., A. Margalit, et al. (2005). "The nuclear lamina comes of age." Nat Rev Mol Cell Biol **6**(1): 21-31.
Guelen, L., L. Pagie, et al. (2008). "Domain organization of human chromosomes revealed by mapping of nuclear lamina interactions." Nature **453**(7197): 948-951.
Gurdon, J. B. (1962). "The developmental capacity of nuclei taken from intestinal epithelium cells of feeding tadpoles." J Embryol Exp Morphol **10**: 622-640.
Harborth, J., S. M. Elbashir, et al. (2001). "Identification of essential genes in cultured mammalian cells using small interfering RNAs." J Cell Sci **114**(Pt 24): 4557-4565.
Harikumar, A. and E. Meshorer (2015). "Chromatin remodeling and bivalent histone modifications in embryonic stem cells." EMBO Rep **16**(12): 1609-1619.
Harr, J. C., T. R. Luperchio, et al. (2015). "Directed targeting of chromatin to the nuclear lamina is mediated by chromatin state and A-type lamins." J Cell Biol **208**(1): 33-52.
He, J. Q., Y. Ma, et al. (2003). "Human embryonic stem cells develop into multiple types of cardiac myocytes: action potential characterization." Circ Res **93**(1): 32-39.
Herrmann, H. and U. Aebi (2016). "Intermediate Filaments: Structure and Assembly." Cold Spring Harb Perspect Biol **8**(11).
Hershberger, R. E. and J. D. Siegfried (2011). "Update 2011: clinical and genetic issues in familial dilated cardiomyopathy." J Am Coll Cardiol **57**(16): 1641-1649.
Ho, J. C., T. Zhou, et al. (2011). "Generation of induced pluripotent stem cell lines from 3 distinct laminopathies bearing heterogeneous mutations in lamin A/C." Aging (Albany NY) **3**(4): 380-390.
Hochedlinger, K. and R. Jaenisch (2002). "Nuclear transplantation: lessons from frogs and mice." Curr Opin Cell Biol **14**(6): 741-748.
Hockemeyer, D. and R. Jaenisch (2016). "Induced Pluripotent Stem Cells Meet Genome Editing." Cell Stem Cell **18**(5): 573-586.

Ikegami, K., T. A. Egelhofer, et al. (2010). "Caenorhabditis elegans chromosome arms are anchored to the nuclear membrane via discontinuous association with LEM-2." Genome Biol **11**(12): R120.

International Stem Cell, I., O. Adewumi, et al. (2007). "Characterization of human embryonic stem cell lines by the International Stem Cell Initiative." Nat Biotechnol **25**(7): 803-816.

Johnson, B. R., R. T. Nitta, et al. (2004). "A-type lamins regulate retinoblastoma protein function by promoting subnuclear localization and preventing proteasomal degradation." Proc Natl Acad Sci U S A **101**(26): 9677-9682.

Kaji, K., K. Norrby, et al. (2009). "Virus-free induction of pluripotency and subsequent excision of reprogramming factors." Nature **458**(7239): 771-775.

Kelly, J. J., J. Simek, et al. (2015). "Mechanisms linking connexin mutations to human diseases." Cell Tissue Res **360**(3): 701-721.

Kim, K., A. Doi, et al. (2010). "Epigenetic memory in induced pluripotent stem cells." Nature **467**(7313): 285-290.

Kind, J., L. Pagie, et al. (2013). "Single-cell dynamics of genome-nuclear lamina interactions." Cell **153**(1): 178-192.

Kind, J. and B. van Steensel (2010). "Genome-nuclear lamina interactions and gene regulation." Curr Opin Cell Biol **22**(3): 320-325.

Kleber, A. G. and Y. Rudy (2004). "Basic mechanisms of cardiac impulse propagation and associated arrhythmias." Physiol Rev **84**(2): 431-488.

Kolb, T., K. Maass, et al. (2011). "Lamin A and lamin C form homodimers and coexist in higher complex forms both in the nucleoplasmic fraction and in the lamina of cultured human cells." Nucleus **2**(5): 425-433.

Krohne, G. and R. Benavente (1986). "The nuclear lamins. A multigene family of proteins in evolution and differentiation." Exp Cell Res **162**(1): 1-10.

Kubben, N., J. W. Voncken, et al. (2010). "Mapping of protein- and chromatin-interactions at the nuclear lamina." Nucleus **1**(6): 460-471.

Laflamme, M. A., K. Y. Chen, et al. (2007). "Cardiomyocytes derived from human embryonic stem cells in pro-survival factors enhance function of infarcted rat hearts." Nat Biotechnol **25**(9): 1015-1024.

Larrieu, D., S. Britton, et al. (2014). "Chemical inhibition of NAT10 corrects defects of laminopathic cells." Science **344**(6183): 527-532.

Larrieu, D., E. Vire, et al. (2018). "Inhibition of the acetyltransferase NAT10 normalizes progeric and aging cells by rebalancing the Transportin-1 nuclear import pathway." Sci Signal **11**(537).

Lee, J. H., S. I. Protze, et al. (2017). "Human Pluripotent Stem Cell-Derived Atrial and Ventricular Cardiomyocytes Develop from Distinct Mesoderm Populations." Cell Stem Cell **21**(2): 179-194 e174.

Lee, T. I., R. G. Jenner, et al. (2006). "Control of developmental regulators by Polycomb in human embryonic stem cells." Cell **125**(2): 301-313.

Lee, Y. K., Y. Jiang, et al. (2016). "Recent advances in animal and human pluripotent stem cell modeling of cardiac laminopathy." Stem Cell Res Ther **7**(1): 139.

Lee, Y. K., Y. M. Lau, et al. (2017). "Modeling Treatment Response for Lamin A/C Related Dilated Cardiomyopathy in Human Induced Pluripotent Stem Cells." J Am Heart Assoc **6**(8).

Leybaert, L., P. D. Lampe, et al. (2017). "Connexins in Cardiovascular and Neurovascular Health and Disease: Pharmacological Implications." Pharmacol Rev **69**(4): 396-478.

Li, H. L., N. Fujimoto, et al. (2015). "Precise correction of the dystrophin gene in duchenne muscular dystrophy patient induced pluripotent stem cells by TALEN and CRISPR-Cas9." Stem Cell Reports **4**(1): 143-154.

Li, W., L. Yin, et al. (2018). "SCN5A Variants: Association With Cardiac Disorders." Front Physiol **9**: 1372.

Lian, X., J. Zhang, et al. (2013). "Directed cardiomyocyte differentiation from human pluripotent stem cells by modulating Wnt/beta-catenin signaling under fully defined conditions." Nat Protoc **8**(1): 162-175.
Lieu, D. K., J. D. Fu, et al. (2013). "Mechanism-based facilitated maturation of human pluripotent stem cell-derived cardiomyocytes." Circ Arrhythm Electrophysiol **6**(1): 191-201.
Liu, Z., H. Shan, et al. (2016). "A novel lamin A/C gene missense mutation (445 V > E) in immunoglobulin-like fold associated with left ventricular non-compaction." Europace **18**(4): 617-622.
Lodola, F., D. Morone, et al. (2016). "Adeno-associated virus-mediated CASQ2 delivery rescues phenotypic alterations in a patient-specific model of recessive catecholaminergic polymorphic ventricular tachycardia." Cell Death Dis **7**(10): e2393.
Loh, Y. H., W. Zhang, et al. (2007). "Jmjd1a and Jmjd2c histone H3 Lys 9 demethylases regulate self-renewal in embryonic stem cells." Genes Dev **21**(20): 2545-2557.
Long, C., H. Li, et al. (2018). "Correction of diverse muscular dystrophy mutations in human engineered heart muscle by single-site genome editing." Sci Adv **4**(1): eaap9004.
Lund, E., A. R. Oldenburg, et al. (2013). "Lamin A/C-promoter interactions specify chromatin state-dependent transcription outcomes." Genome Res **23**(10): 1580-1589.
Luperchio, T. R., X. Wong, et al. (2014). "Genome regulation at the peripheral zone: lamina associated domains in development and disease." Curr Opin Genet Dev **25**: 50-61.
Macquart, C., R. Juttner, et al. (2018). "Microtubule cytoskeleton regulates connexin 43 localization and cardiac conduction in cardiomyopathy caused by mutation in A-type lamins gene." Hum Mol Genet.
Malik, N. and M. S. Rao (2013). "A review of the methods for human iPSC derivation." Methods Mol Biol **997**: 23-33.
Mandai, M., A. Watanabe, et al. (2017). "Autologous Induced Stem-Cell-Derived Retinal Cells for Macular Degeneration." N Engl J Med **376**(11): 1038-1046.
Margalit, A., E. Neufeld, et al. (2007). "Barrier to autointegration factor blocks premature cell fusion and maintains adult muscle integrity in C. elegans." J Cell Biol **178**(4): 661-673.
Markandeya, Y. S., T. Tsubouchi, et al. (2016). "Inhibition of late sodium current attenuates ionic arrhythmia mechanism in ventricular myocytes expressing LaminA-N195K mutation." Heart Rhythm **13**(11): 2228-2236.
Marti, M., L. Mulero, et al. (2013). "Characterization of pluripotent stem cells." Nat Protoc **8**(2): 223-253.
Marullo, F., E. Cesarini, et al. (2016). "Nucleoplasmic Lamin A/C and Polycomb group of proteins: An evolutionarily conserved interplay." Nucleus **7**(2): 103-111.
McCulloch, E. A. and J. E. Till (1960). "The radiation sensitivity of normal mouse bone marrow cells, determined by quantitative marrow transplantation into irradiated mice." Radiat Res **13**: 115-125.
McNally, E. M. and L. Mestroni (2017). "Dilated Cardiomyopathy: Genetic Determinants and Mechanisms." Circ Res **121**(7): 731-748.
Meuleman, W., D. Peric-Hupkes, et al. (2013). "Constitutive nuclear lamina-genome interactions are highly conserved and associated with A/T-rich sequence." Genome Res **23**(2): 270-280.
Mihic, A., J. Li, et al. (2014). "The effect of cyclic stretch on maturation and 3D tissue formation of human embryonic stem cell-derived cardiomyocytes." Biomaterials **35**(9): 2798-2808.
Miragoli, M., G. Gaudesius, et al. (2006). "Electrotonic modulation of cardiac impulse conduction by myofibroblasts." Circ Res **98**(6): 801-810.

Molica, F., M. J. Meens, et al. (2014). "Mutations in cardiovascular connexin genes." Biol Cell **106**(9): 269-293.
Moretti, A., M. Bellin, et al. (2010). "Patient-specific induced pluripotent stem-cell models for long-QT syndrome." N Engl J Med **363**(15): 1397-1409.
Mounkes, L. C., S. V. Kozlov, et al. (2005). "Expression of an LMNA-N195K variant of A-type lamins results in cardiac conduction defects and death in mice." Hum Mol Genet **14**(15): 2167-2180.
Muchir, A., P. Pavlidis, et al. (2007). "Activation of MAPK in hearts of EMD null mice: similarities between mouse models of X-linked and autosomal dominant Emery Dreifuss muscular dystrophy." Hum Mol Genet **16**(15): 1884-1895.
Mummery, C., D. Ward-van Oostwaard, et al. (2003). "Differentiation of human embryonic stem cells to cardiomyocytes: role of coculture with visceral endoderm-like cells." Circulation **107**(21): 2733-2740.
Naetar, N., B. Korbei, et al. (2008). "Loss of nucleoplasmic LAP2alpha-lamin A complexes causes erythroid and epidermal progenitor hyperproliferation." Nat Cell Biol **10**(11): 1341-1348.
Nakahama, H. and E. Di Pasquale (2016). "Generation of Cardiomyocytes from Pluripotent Stem Cells." Methods Mol Biol **1353**: 181-190.
Ng, E. S., R. P. Davis, et al. (2005). "Forced aggregation of defined numbers of human embryonic stem cells into embryoid bodies fosters robust, reproducible hematopoietic differentiation." Blood **106**(5): 1601-1603.
Nikolova, V., C. Leimena, et al. (2004). "Defects in nuclear structure and function promote dilated cardiomyopathy in lamin A/C-deficient mice." J Clin Invest **113**(3): 357-369.
Nomura, S. (2018). "Genetic and non-genetic determinants of clinical phenotypes in cardiomyopathy." J Cardiol.
Nunes, S. S., J. W. Miklas, et al. (2013). "Biowire: a platform for maturation of human pluripotent stem cell-derived cardiomyocytes." Nat Methods **10**(8): 781-787.
Otsuji, T. G., I. Minami, et al. (2010). "Progressive maturation in contracting cardiomyocytes derived from human embryonic stem cells: Qualitative effects on electrophysiological responses to drugs." Stem Cell Res **4**(3): 201-213.
Paige, S. L., T. Osugi, et al. (2010). "Endogenous Wnt/beta-catenin signaling is required for cardiac differentiation in human embryonic stem cells." PLoS One **5**(6): e11134.
Papp, B. and K. Plath (2013). "Epigenetics of reprogramming to induced pluripotency." Cell **152**(6): 1324-1343.
Park, I. H., R. Zhao, et al. (2008). "Reprogramming of human somatic cells to pluripotency with defined factors." Nature **451**(7175): 141-146.
Passier, R., D. W. Oostwaard, et al. (2005). "Increased cardiomyocyte differentiation from human embryonic stem cells in serum-free cultures." Stem Cells **23**(6): 772-780.
Paulis, M., A. Castelli, et al. (2015). "A pre-screening FISH-based method to detect CRISPR/Cas9 off-targets in mouse embryonic stem cells." Sci Rep **5**: 12327.
Paulis, M., A. Castelli, et al. (2015). "Chromosome transplantation as a novel approach for correcting complex genomic disorders." Oncotarget **6**(34): 35218-35230.
Paulsen, J., M. Sekelja, et al. (2017). "Chrom3D: three-dimensional genome modeling from Hi-C and nuclear lamin-genome contacts." Genome Biol **18**(1): 21.
Peric-Hupkes, D., W. Meuleman, et al. (2010). "Molecular maps of the reorganization of genome-nuclear lamina interactions during differentiation." Mol Cell **38**(4): 603-613.
Perovanovic, J., S. Dell'Orso, et al. (2016). "Laminopathies disrupt epigenomic developmental programs and cell fate." Sci Transl Med **8**(335): 335ra358.
Pickersgill, H., B. Kalverda, et al. (2006). "Characterization of the Drosophila melanogaster genome at the nuclear lamina." Nat Genet **38**(9): 1005-1014.

Pointon, A., A. R. Harmer, et al. (2015). "Assessment of cardiomyocyte contraction in human-induced pluripotent stem cell-derived cardiomyocytes." Toxicol Sci **144**(2): 227-237.
Priori, S. G., C. Napolitano, et al. (2013). "Induced pluripotent stem cell-derived cardiomyocytes in studies of inherited arrhythmias." J Clin Invest **123**(1): 84-91.
Raffaele Di Barletta, M., E. Ricci, et al. (2000). "Different mutations in the LMNA gene cause autosomal dominant and autosomal recessive Emery-Dreifuss muscular dystrophy." Am J Hum Genet **66**(4): 1407-1412.
Ran, F. A., P. D. Hsu, et al. (2013). "Genome engineering using the CRISPR-Cas9 system." Nat Protoc **8**(11): 2281-2308.
Reddy, K. L., J. M. Zullo, et al. (2008). "Transcriptional repression mediated by repositioning of genes to the nuclear lamina." Nature **452**(7184): 243-247.
Robertson, C., D. D. Tran, et al. (2013). "Concise review: maturation phases of human pluripotent stem cell-derived cardiomyocytes." Stem Cells **31**(5): 829-837.
Robson, M. I., J. I. de Las Heras, et al. (2016). "Tissue-Specific Gene Repositioning by Muscle Nuclear Membrane Proteins Enhances Repression of Critical Developmental Genes during Myogenesis." Mol Cell **62**(6): 834-847.
Roncarati, R., C. Viviani Anselmi, et al. (2013). "Doubly heterozygous LMNA and TTN mutations revealed by exome sequencing in a severe form of dilated cardiomyopathy." Eur J Hum Genet **21**(10): 1105-1111.
Rook, M. B., M. M. Evers, et al. (2012). "Biology of cardiac sodium channel Nav1.5 expression." Cardiovasc Res **93**(1): 12-23.
Rusinol, A. E. and M. S. Sinensky (2006). "Farnesylated lamins, progeroid syndromes and farnesyl transferase inhibitors." J Cell Sci **119**(Pt 16): 3265-3272.
Scaffidi, P. and T. Misteli (2006). "Lamin A-dependent nuclear defects in human aging." Science **312**(5776): 1059-1063.
Scheiner, Z. S., S. Talib, et al. (2014). "The potential for immunogenicity of autologous induced pluripotent stem cell-derived therapies." J Biol Chem **289**(8): 4571-4577.
Seki, T., S. Yuasa, et al. (2012). "Generation of induced pluripotent stem cells from a small amount of human peripheral blood using a combination of activated T cells and Sendai virus." Nat Protoc **7**(4): 718-728.
Senior, A. and L. Gerace (1988). "Integral membrane proteins specific to the inner nuclear membrane and associated with the nuclear lamina." J Cell Biol **107**(6 Pt 1): 2029-2036.
Serebryannyy, L. A., D. A. Ball, et al. (2018). "Single molecule analysis of lamin dynamics." Methods.
Shen, Q., X. Zheng, et al. (2009). "NAT10, a nucleolar protein, localizes to the midbody and regulates cytokinesis and acetylation of microtubules." Exp Cell Res **315**(10): 1653-1667.
Shumaker, D. K., T. Dechat, et al. (2006). "Mutant nuclear lamin A leads to progressive alterations of epigenetic control in premature aging." Proc Natl Acad Sci U S A **103**(23): 8703-8708.
Singh, V. K., M. Kalsan, et al. (2015). "Induced pluripotent stem cells: applications in regenerative medicine, disease modeling, and drug discovery." Front Cell Dev Biol **3**: 2.
Siu, C. W., Y. K. Lee, et al. (2012). "Modeling of lamin A/C mutation premature cardiac aging using patient-specific induced pluripotent stem cells." Aging (Albany NY) **4**(11): 803-822.
Slaymaker, I. M., L. Gao, et al. (2016). "Rationally engineered Cas9 nucleases with improved specificity." Science **351**(6268): 84-88.
Smith, A. G. (2001). "Embryo-derived stem cells: of mice and men." Annu Rev Cell Dev Biol **17**: 435-462.

Solovei, I., A. S. Wang, et al. (2013). "LBR and lamin A/C sequentially tether peripheral heterochromatin and inversely regulate differentiation." Cell **152**(3): 584-598.
Sommer, C. A., M. Stadtfeld, et al. (2009). "Induced pluripotent stem cell generation using a single lentiviral stem cell cassette." Stem Cells **27**(3): 543-549.
Speckman, R. A., A. Garg, et al. (2000). "Mutational and haplotype analyses of families with familial partial lipodystrophy (Dunnigan variety) reveal recurrent missense mutations in the globular C-terminal domain of lamin A/C." Am J Hum Genet **66**(4): 1192-1198.
Sullivan, T., D. Escalante-Alcalde, et al. (1999). "Loss of A-type lamin expression compromises nuclear envelope integrity leading to muscular dystrophy." J Cell Biol **147**(5): 913-920.
Sun, N., M. Yazawa, et al. (2012). "Patient-specific induced pluripotent stem cells as a model for familial dilated cardiomyopathy." Sci Transl Med **4**(130): 130ra147.
Swift, J., I. L. Ivanovska, et al. (2013). "Nuclear lamin-A scales with tissue stiffness and enhances matrix-directed differentiation." Science **341**(6149): 1240104.
Takahashi, K., K. Tanabe, et al. (2007). "Induction of pluripotent stem cells from adult human fibroblasts by defined factors." Cell **131**(5): 861-872.
Takahashi, K. and S. Yamanaka (2006). "Induction of pluripotent stem cells from mouse embryonic and adult fibroblast cultures by defined factors." Cell **126**(4): 663-676.
Takahashi, K. and S. Yamanaka (2016). "A decade of transcription factor-mediated reprogramming to pluripotency." Nat Rev Mol Cell Biol **17**(3): 183-193.
Takeda, M., Y. Kanki, et al. (2018). "Identification of Cardiomyocyte-Fated Progenitors from Human-Induced Pluripotent Stem Cells Marked with CD82." Cell Rep **22**(2): 546-556.
Tesson, F., M. Saj, et al. (2014). "Lamin A/C mutations in dilated cardiomyopathy." Cardiol J **21**(4): 331-342.
Thomson, J. A., J. Itskovitz-Eldor, et al. (1998). "Embryonic stem cell lines derived from human blastocysts." Science **282**(5391): 1145-1147.
Tohyama, S., F. Hattori, et al. (2013). "Distinct metabolic flow enables large-scale purification of mouse and human pluripotent stem cell-derived cardiomyocytes." Cell Stem Cell **12**(1): 127-137.
Tong, J., W. Li, et al. (2011). "Lamin A/C deficiency is associated with fat infiltration of muscle and bone." Mech Ageing Dev **132**(11-12): 552-559.
Toth, J. I., S. H. Yang, et al. (2005). "Blocking protein farnesyltransferase improves nuclear shape in fibroblasts from humans with progeroid syndromes." Proc Natl Acad Sci U S A **102**(36): 12873-12878.
van Rijsingen, I. A., E. Arbustini, et al. (2012). "Risk factors for malignant ventricular arrhythmias in lamin a/c mutation carriers a European cohort study." J Am Coll Cardiol **59**(5): 493-500.
van Steensel, B. and A. S. Belmont (2017). "Lamina-Associated Domains: Links with Chromosome Architecture, Heterochromatin, and Gene Repression." Cell **169**(5): 780-791.
Veeraraghavan, R., R. G. Gourdie, et al. (2014). "Mechanisms of cardiac conduction: a history of revisions." Am J Physiol Heart Circ Physiol **306**(5): H619-627.
Waddington, C. H. (1957). "The Strategy of the genes." London:Allen and Unwin.
Warren, L., P. D. Manos, et al. (2010). "Highly efficient reprogramming to pluripotency and directed differentiation of human cells with synthetic modified mRNA." Cell Stem Cell **7**(5): 618-630.
Watanabe, A., Y. Yamada, et al. (2013). "Epigenetic regulation in pluripotent stem cells: a key to breaking the epigenetic barrier." Philos Trans R Soc Lond B Biol Sci **368**(1609): 20120292.
Wilmut, I., A. E. Schnieke, et al. (1997). "Viable offspring derived from fetal and adult mammalian cells." Nature **385**(6619): 810-813.

Wilson, K. L. and R. Foisner (2010). "Lamin-binding Proteins." Cold Spring Harb Perspect Biol **2**(4): a000554.
Woltjen, K., I. P. Michael, et al. (2009). "piggyBac transposition reprograms fibroblasts to induced pluripotent stem cells." Nature **458**(7239): 766-770.
Worman, H. J. (2012). "Nuclear lamins and laminopathies." J Pathol **226**(2): 316-325.
Worman, H. J. and G. Bonne (2007). ""Laminopathies": a wide spectrum of human diseases." Exp Cell Res **313**(10): 2121-2133.
Worman, H. J. and J. C. Courvalin (2002). "The nuclear lamina and inherited disease." Trends Cell Biol **12**(12): 591-598.
Xu, C., S. Police, et al. (2002). "Characterization and enrichment of cardiomyocytes derived from human embryonic stem cells." Circ Res **91**(6): 501-508.
Yanez-Cuna, J. O. and B. van Steensel (2017). "Genome-nuclear lamina interactions: from cell populations to single cells." Curr Opin Genet Dev **43**: 67-72.
Yang, D., Z. J. Zhang, et al. (2008). "Human embryonic stem cell-derived dopaminergic neurons reverse functional deficit in parkinsonian rats." Stem Cells **26**(1): 55-63.
Yoon, B. S., S. J. Yoo, et al. (2006). "Enhanced differentiation of human embryonic stem cells into cardiomyocytes by combining hanging drop culture and 5-azacytidine treatment." Differentiation **74**(4): 149-159.
Yoshida, Y., K. Takahashi, et al. (2009). "Hypoxia enhances the generation of induced pluripotent stem cells." Cell Stem Cell **5**(3): 237-241.
Young, S. G., L. G. Fong, et al. (2005). "Prelamin A, Zmpste24, misshapen cell nuclei, and progeria--new evidence suggesting that protein farnesylation could be important for disease pathogenesis." J Lipid Res **46**(12): 2531-2558.
Yu, J., M. A. Vodyanik, et al. (2007). "Induced pluripotent stem cell lines derived from human somatic cells." Science **318**(5858): 1917-1920.
Yusa, K. (2013). "Seamless genome editing in human pluripotent stem cells using custom endonuclease-based gene targeting and the piggyBac transposon." Nat Protoc **8**(10): 2061-2078.
Zahr, H. C. and D. E. Jaalouk (2018). "Exploring the Crosstalk Between LMNA and Splicing Machinery Gene Mutations in Dilated Cardiomyopathy." Front Genet **9**: 231.
Zhang, H., J. E. Kieckhaefer, et al. (2013). "Mouse models of laminopathies." Aging Cell **12**(1): 2-10.
Zhang, J., M. Klos, et al. (2012). "Extracellular matrix promotes highly efficient cardiac differentiation of human pluripotent stem cells: the matrix sandwich method." Circ Res **111**(9): 1125-1136.
Zuleger, N., M. I. Robson, et al. (2011). "The nuclear envelope as a chromatin organizer." Nucleus **2**(5): 339-349.